POLYPUBLIE
Polytechnique Montréal

POLYTECHNIQUE MONTRÉAL
UNIVERSITÉ D'INGÉNIERIE

Titre: Title:	Towards Ultra-Low Specific Contact Resistance On High Sn-Content GeSn For Mid-Infrared Optoelectronics
Auteur: Author:	Salim Abdi
Date:	2020
Type:	Mémoire ou thèse / Dissertation or Thesis
Référence: Citation:	Abdi, S. (2020). Towards Ultra-Low Specific Contact Resistance On High Sn-Content GeSn For Mid-Infrared Optoelectronics [Master's thesis, Polytechnique Montréal]. PolyPublie. https://publications.polymtl.ca/5471/

Document en libre accès dans PolyPublie
Open Access document in PolyPublie

URL de PolyPublie: PolyPublie URL:	https://publications.polymtl.ca/5471/
Directeurs de recherche: Advisors:	Oussama Moutanabbir
Programme: Program:	Génie physique

Ce fichier a été téléchargé à partir de PolyPublie, le dépôt institutionnel de Polytechnique Montréal
This file has been downloaded from PolyPublie, the institutional repository of Polytechnique Montréal

https://publications.polymtl.ca

POLYTECHNIQUE MONTRÉAL

affiliée à l'Université de Montréal

Towards Ultra-Low Specific Contact Resistance On High Sn-Content GeSn For Mid-Infrared Optoelectronics

SALIM ABDI

Département de génie physique

Mémoire présenté en vue de l'obtention du diplôme de *Maîtrise ès sciences appliquées*

Génie physique

Octobre 2020

© Salim Abdi, 2020.

POLYTECHNIQUE MONTRÉAL

affiliée à l'Université de Montréal

Ce mémoire intitulé :

Towards Ultra-Low Specific Contact Resistance On High Sn-Content GeSn For Mid-Infrared Optoelectronics

présenté par **Salim ABDI**

en vue de l'obtention du diplôme de *Maîtrise ès sciences appliquées*

a été dûment accepté par le jury d'examen constitué de :

Yves-Alain PETER, président

Oussama MOUTANABBIR, membre et directeur de recherche

Bruce B. CLAFLIN Jr., membre externe

DEDICATION

To my family and friends...

ACKNOWLEDGEMENTS

First, I would like to start by expressing my sincerest gratitude to my supervisor Prof. Oussama Moutanabbir, for his continuous guidance throughout the two years of my stay in the Nano and Quantum Semiconductors (NQS) Laboratory, for his wisdom and experience, and for giving me the opportunity to work in a highly promising field of study. I am also grateful to Dr. Jeffrey Warrender at the US Army ARDEC laboratory for his collaboration in laser annealing studies. In addition, I would also like to thank the Jury members Dr. Bruce B. Claflin and Prof. Yves-Alain Peter for their time and comments on my thesis.

I am honored to be part of the team at the NQS group. Our work has always been highly collaborative. Thus, I would also like to deeply thank all of my lab colleagues and friends. I would not have finished this work without them. I would like to start with Dr. Simone Assali for his assistance in my research by growing the material and providing high-quality samples, and for his continuous fruitful discussions. I would like to equally thank Dr. Mahmoud Atalla for openly sharing his experience in designing miniaturized devices and his support during electrical measurements. Moreover, I would like to thank Dr. Sebastian Koelling for arranging the TEM and part of the SIMS measurements, Aashish Kumar and Jérôme Nicholas for their assistance in acquiring part of the XRD and AFM results, and Anis Attiaoui for his ellipsometry measurements. Finally, I convey my thanks to Dr. Samik Mukherjee, Dr. Matthieu Fortin-Deschênes, Lu Luo, and all of my mates. I would also like to sincerely thank the LCM and GCM staff, for their trainings and assistance in multiple tools, especially Christophe Clément, Patricia Moraille, Marie-Hélène Bernier, and Josianne Lefebvre.

Finally, I would like to highlight my appreciation to Alghurair Foundation for Education (AGFE), for their support and scholarship throughout the entire duration of my program, and I especially thank our coordinator Guylaine Larocque for her strategic advices. Last but not least, I would like to thank my family members for their support and encouragement from overseas, and all of my friends here and in Algeria.

RÉSUMÉ

La photonique intégrée à base de silicium (Si), fonctionnant dans le domaine infrarouge IR-B (c-à-d 1,4 à 3 µm) et au-delà, constitue une plateforme importante pour le développement de dispositifs photoniques robustes, abordables et fortement modulables. Dans ce cadre, les semi-conducteurs du groupe-IV à base de germanium-étain (GeSn) ont récemment fait l'objet de plusieurs études. Premièrement, car ils offrent une bande interdite directe qui est accordable dans ce domaine de longueurs d'onde. Deuxièmement, pour leur compatibilité avec la plateforme des semi-conducteurs complémentaires à l'oxyde de métal (CMOS), ainsi permettant leur intégration dans les procédés industriels bien établis de l'électronique en Si, afin de produire des dispositifs électroniques et photoniques sur la même puce. Il peut s'agir d'une révolution dans la fabrication de tels dispositifs, et avoir un impact important sur un large spectre d'applications existantes et futures, telle que la vision infrarouge à cout réduit pour usage militaire ou civil tel que dans les voitures autonomes, la détection des gaz, la spectroscopie et les capteurs intégrés pour les *laboratoire-sur-puce*.

Le succès de la fabrication des dispositifs basés sur GeSn repose sur le développement des jonctions de base, ou des composantes constituant leurs régions actives et passives. D'ailleurs, l'une des jonctions passives les plus importantes de tout dispositif à base de semi-conducteurs est la jonction métal-semi-conducteur (M-S). Ainsi, une solution de traitement adaptée, fournissant des contacts M-S hautement performants est cruciale. Les conditions de traitement doivent également être compatibles avec les limites intrinsèques du matériau, et la nature du contact, car les deux affectent négativement la performance des contacts. De même, la solution doit être pratique, abordable, compatible avec le CMOS, et adaptables aux différentes applications. Dans cette perspective, cette thèse est un aboutissement des efforts réalisés pour développer des étapes fondamentales de traitement des contacts M-GeSn, répondant aux conditions mentionnées ci-dessus, tout en maintenant une grande intégrité des dispositifs pendant le traitement.

La première partie de la thèse se concentre sur l'implémentation du recuit thermique au laser ultra rapide, comme solution potentielle de traitement à faible énergie pour les contacts métalliques sur GeSn. Le but est de fonctionnaliser les contacts sans endommager les couches de GeSn en dessous. Les résultats montrent le potentiel d'application de cette technique sur des dispositifs futurs. En

effet, la résistance de contact spécifique des couches de nickel a diminué par un facteur de 100, alors que les couches de GeSn ont préservé leur qualité lors du recuit en laser, sous certaines conditions.

La deuxième partie se concentre sur la compréhension du processus de dopage de GeSn. Pour le dopage *in situ* de type-p utilisant le bore, la concentration active a été contrôlée dans l'intervalle 10^{17}-10^{19} cm^{-3}, à des concentrations de Sn comprises entre 6 et 9 at.%. D'autre part, pour le dopage *in situ* de type-n en utilisant l'Arsénique, une concentration active très élevée de 10^{20} cm^{-3} a été obtenue à une teneur en Sn de 9 at.%. Les couches GeSn hautement dopées et à haute teneur en Sn servent comme des substrats optimaux pour la fabrication des futures jonctions M-GeSn. Ces résultats préparent le terrain pour le développement de futurs procédés qui visent la fabrication des contacts ohmiques hautement efficaces sur des couches de GeSn à haute teneur de Sn.

ABSTRACT

Silicon-based integrated photonics, operating in the short-wave infrared at the 1.4–3 µm range and beyond, provides a platform for the development of robust, affordable, and highly scalable photonic devices. For this purpose, germanium-tin (GeSn)-based group-IV semiconductors have been extensively studied as they offer a tunable direct bandgap in this infrared range. Moreover, their compatibility with the Si complementary-metal-oxide-semiconductor (CMOS) platform allows for their seamless integration with the well-established Si electronics industry, to produce electronic and photonic devices on the same chip. This could be a revolution in the fabrication of such devices, and can profoundly impact a wide spectrum of existing and future applications, such as affordable infrared vision for military and consumer market including self-driving cars, efficient gas sensing and imaging, and integrated *lab-on-a-chip* sensors.

The success in fabricating GeSn-based devices relies on the development of the essential junctions, or building blocks, constituting their active and passive regions. The metal-semiconductor (M-S) junction is among one of the most critical passive junctions in semiconductor-based devices. Thus, a processing solution tailored to achieve high-performance M-S contacts is crucial. The processing conditions need to be compatible with the intrinsic limitations imposed by the material and the contact properties. Moreover, processing these devices must be practical, affordable, CMOS-compatible, and adaptable to different applications. With this perspective, this thesis is a culmination of the efforts realized to develop key M-GeSn processing steps that meet the conditions mentioned above, while maintaining high device integrity during processing.

The first part of this thesis focuses on investigating ultrafast laser thermal annealing as a potential low thermal budget processing solution for M-GeSn contacts. The goal is to functionalize the contacts without damaging the GeSn layers underneath. Results show the possibility of applying this technique on future devices, as the specific contact resistance in Nickel contacts was lowered by a factor of 100 as a result of forming a Ni-based GeSn alloy, while buried GeSn layers preserved their quality upon annealing at certain conditions.

The second part concentrates on understanding the *in situ* doping process during the growth of relaxed GeSn. Both p-type and n-type doping were studied for this purpose. For p-type doping using boron, the active concentration was controlled in the 10^{17}-10^{19} cm^{-3} range, at Sn

concentrations between 6 and 9 at.%. On the other hand, for n-type doping using arsenic, a very high active concentration of 10^{20} cm^{-3} was achieved at a Sn-content of 9 at.%. The highly doped and high Sn-content GeSn layers serve as optimal substrates for the fabrication of future M-GeSn junctions. These results lay the groundwork for the development of future processes that target the fabrication of highly efficient ohmic contacts on GeSn layers.

TABLE OF CONTENTS

DEDICATION III

ACKNOWLEDGEMENTS IV

RÉSUMÉ V

ABSTRACT VII

TABLE OF CONTENTS IX

LIST OF TABLES XII

LIST OF FIGURES XIII

LIST OF SYMBOLS AND ABBREVIATIONS XVII

CHAPTER 1 INTRODUCTION 1

1.1 Context 1

1.2 Research objectives 3

1.3 Thesis outline 4

CHAPTER 2 LITTERATURE REVIEW 5

2.1 Metastable GeSn alloys: from theory to experimental realization 5

2.2 Metal-Semiconductor contacts 8

2.2.1 Ideal Schottky barriers 8

2.2.2 Influence of the doping level on the current transport in M-S contacts 10

2.2.3 The resistance of ohmic contacts 12

2.3 Ge- and GeSn-based real contacts and Fermi Level-Pinning 14

2.3.1 Fermi-level depinning solutions to Ge and GeSn contacts 16

2.3.2 Effect of Sn incorporation on the performance of ohmic contacts on GeSn 18

2.3.3 Contact solutions for GeSn with high Sn content 19

CHAPTER 3 EXPERIMENTAL METHODS AND TECHNIQUES 21

3.1 Growth of metastable GeSn alloys 21

3.2 Microfabrication of GeSn-based devices 22

3.3 Characterization methods 24

3.3.1 X-ray diffraction 24

3.3.2 Capacitance-Voltage measurements of Metal-Oxide-Semiconductor capacitors 26

3.3.3 Current-Voltage measurements of M-S devices 30

3.3.4 Transmission electron microscopy 33

3.3.5 Secondary ion mass spectrometry 34

3.3.6 Atomic force microscopy 36

CHAPTER 4 LASER THERMAL ANNEALING EFFECTS ON CONTACT RESISTANCE OF NI/$GE_{1-X}SN_X$ AND STABILITY OF RELAXED $GE_{1-X}SN_X$ SEMICONDUCTORS 39

4.1 Introduction 39

4.2 Experimental details 40

4.3 Sn diffusion during LTA of relaxed GeSn semiconductors 42

4.4 Laser annealing of Ni contacts on GeSn 51

CHAPTER 5 *IN SITU* N-TYPE AND P-TYPE DOPING OF PARTIALLY-RELAXED $GE_{0.91}SN_{0.09}$ 57

5.1 Introduction 57

5.2 Choice of the doping process, dopant atoms, and their precursors 57

5.3 p-type GeSn growth and characterization 59

5.3.1 Epitaxial growth 59

5.3.2 Impact of B doping on the growth kinetics and morphological quality of GeSn 60

5.3.3 Boron doping concentration and activation ratio 63

5.3.4 Impact of the growth temperature on B incorporation of GeSn:B 66

5.4 N-type doping of relaxed GeSn 67

5.4.1 Epitaxial growth 67

5.4.2 Impact of As doping on the morphological quality of GeSn 68

5.4.3 Arsenic doping concentration and activation ratio 71

5.5 Impact of boron and arsenic incorporation on the electrical properties of GeSn M-S devices 73

CHAPTER 6 CONCLUSION AND PERSPECTIVES 77

6.1 Main conclusions 77

6.2 Perspectives for future work 79

REFERENCES 81

LIST OF TABLES

Table 4.1 List of the reference Ge-VS and GeSn multilayer samples used in the study 41

LIST OF FIGURES

Figure 2.1 Γ and L conduction bands (CB), valence band (VB), and spin-orbit split-off (SO) energies plotted relative to the vacuum level for the relaxed $Ge_{1-x}Sn_x$. The first two dark shades of gray represent indirect and direct bandgap GeSn, respectively. Reprinted [27] with permission from Polak, M.P., P. Scharoch, and R. Kudrawiec, The electronic band structure of $Ge_{1-x}Sn_x$ in the full composition range: indirect, direct, and inverted gaps regimes, band offsets, and the Burstein–Moss effect. Journal of Physics D: Applied Physics, 2017. 50(19). Copyright 2017 IEEE. 6

Figure 2.2 Sketch of the band diagram of a) separate M and n-type semiconductor (n-S), b) an M/n-S contact. Adapted from [17] 10

Figure 2.3 Sketch of the current transport mechanisms in Metal/n-S contacts a) at low, b) moderate, and c) high doping levels. Adapted from [17] 11

Figure 2.4 Calculated results on the behavior of ρc in TFE as a function of the doping level and SBH for n-type Ge. Reprinted [49] Firrincieli, A., et al., Study of the impact of doping concentration and Schottky barrier height on ohmic contacts to n-type germanium. Microelectronic Engineering, 2013. 106: p. 129-131. (2013) With the permission of Elsevier B.V. 13

Figure 2.5 Experimentally obtained electron SBH on n-Si, n-Ge, and the corresponding original ϕM. Reprinted [18] Nishimura, T., K. Kita, and A. Toriumi, Evidence for strong Fermi-level pinning due to metal-induced gap states at metal/germanium interface. Applied Physics Letters, 2007. 91(12). 15

Figure 3.1 Schematic illustration of a CVD reactor chamber with vertical gas flow 21

Figure 3.2 Illustration of the general steps used in the lift-off approach 23

Figure 3.3 Illustration of the physical X-ray diffraction mechanism 25

Figure 3.4 Schematic illustration of an ideal p-MOScap CV curve (adapted from [109] page 280). The solid line corresponds to low frequencies and the dashed line to high frequencies........27

Figure 3.5 Illustration of the structure and process-flow for device fabrication of Back-to-Back MOScaps a) and c), and conventional MOScaps b) and d), respectively. 28

Figure 3.6 CV plots of a) Si reference sample with a resistivity of 0.1 Ω.cm, b) undoped $Ge_{0.92}Sn_{0.08}$-based B2B, and conventional MOScap devices 29

Figure 3.7 a) Accuracy range of different test structures in the extraction of ρ_c, dashed lines indicate regions where parasitic factors become dominant (© 2016 IEEE. Reprinted, with permission, from [121] Yu, H., et al., Process options to enable (sub-) 10^{-9} Ohm.cm^2 contact resistivity on Si devices, in 2016 IEEE International Interconnect Technology Conference / Advanced Metallization Conference (IITC/AMC). 2016. p. 66-68.), b) one set of CTLM and TLM test structures as-designed in the PL mask, c) process-flow for the fabrication of M-S devices, d) microscopic image of CTLM Ti/Au-on-Si devices...31

Figure 3.8 Schematic illustration of the SIMS components. Reprinted [17] Schroder, D.K., Semiconductor Material and Device Characterization, 654, 2005. With the permission of Wiley & Sons. 35

Figure 3.9 Illustration of the working principle of AFM. Reproduced from ref [130]. Zhong, J. and J. Yan, Seeing is believing: atomic force microscopy imaging for nanomaterial research. RSC Advances, 2016. 6(2): p. 1103-1121. With permission from The Royal Society of Chemistry. 37

Figure 4.1 a) GeSn 8.5 at % Sn (2θ-ω) curves, b) GeSn 11.2 at % Sn (2θ-ω) curves, c) and d) XRD-RSM maps for the 11.2 at% Sn GeSn sample, for the reference and after ED4, respectively 43

Figure 4.2 a) 10 × 10 μm AFM maps for: GeVS: a) as-grown, b) after ED2 and c) after ED4; and GeSn 8.5 at% Sn: d) as-grown, e) after ED2, and f) after ED4. 44

Figure 4.3 1 × 1 μm^2 AFM maps for GeSn at 8.5 at.% Sn: a) Reference. b-e) after ED1-ED4, f) RMS roughness values for GeSn samples obtained from 1 × 1 μm^2 AFM maps 45

Figure 4.4 Higher-resolution Cross-sectional TEM images of the LTA-affected region, Insets are higher resolution images of the top and bottom parts of this region.....................................46

Figure 4.5 a) HAADF image and EDX maps of Ge, Sn, and Pt, of the LTA-affected region, b) lateral EDX compositional profiles (along the length of the blue line in the EDX maps), the solid black line is a profile average along the entire length of the LTA-affected region, c) longitudinal EDX compositional profiles (along the length of the red line in the EDX maps). 47

Figure 4.6 Evolution of the specific contact resistance ρ_c as a function of the laser ED 52

Figure 4.7 Cross-sectional TEM image of the contact Ni/GeSn with 11.2 at.% Sn, after LTA treatment at ED4. The inset on the left-side is a cross-sectional image of the contact edge. Other insets correspond to the HR-STEM images of the regions in small squares. 53

Figure 4.8 a) HAADF image and EDX maps of Ge, Sn, and Ni, of the LTA-affected region, b) EDX compositional depth profile, along the length of the red line in the EDX maps, c-d) longitudinal EDX compositional profiles, along the length of the green and yellow lines in the EDX maps, respectively. 55

Figure 5.1 a) schematic illustration of the GeSn:B growth layout; b) Cross-sectional TEM image of the 10x B_2H_6 sample layer stack; c) GeSn:B samples set (2θ-ω) curves; d-g) 10 × 10 µm AFM maps with their corresponding B_2H_6 flow rates. 61

Figure 5.2 XRD-RSM (224) reflection maps for the GeSn:B samples set with their respective B_2H_6 flows, the arrow indicates the diffraction spot of the topmost layer. 62

Figure 5.3 SIMS composition *vs.* depth profiles for the GeSn:B samples set with their respective B_2H_6 flow rates. 64

Figure 5.4 a) Capacitance-Voltage plots of the GeSn:B MOS Capacitors; b) SIMS Extracted boron intensity as a function of B_2H_6 flows; c) Sn-content and boron active carrier concentration as a function of B_2H_6 flows. 65

Figure 5.5 GeSn:B sample set with the topmost layer grown at 305 °c: a) XRD-RSM (224) map of the 6x B_2H_6 flow sample, b) and c) 10 × 10 µm AFM maps for the undoped reference and doped sample respectively, d) Capacitance-Voltage plots of the 6x GeSn:B MOS Capacitors. 67

Figure 5.6 schematic illustration of the GeSn:As growth layout: a) for the first set, b) and c) for the second set of samples. 68

Figure 5.7 GeSn:As samples: a-c) XRD-RSM (224) maps with their corresponding AsH_3 flows, d) Cross-sectional TEM image of the 25x AsH_3 sample, e-g) 10 × 10 μm^2 AFM maps with their corresponding AsH_3 flows. 69

Figure 5.8 0.1x AsH_3 doped GeSn:As samples: a) 10 × 10 μm^2 AFM map on the doped sample, b) (2θ-ω) curves of the samples; c) XRD-RSM (224) maps of the doped GeSn:As samples. d) SIMS composition *vs*. depth profiles 70

Figure 5.9 Capacitance-Voltage plots of GeSn:As MOSCap devices: a) for the first set, b) for the second set of samples. The negative sign signifies n-type doping.......................................72

Figure 5.10. a) IV plots extracted from TLM devices on the 10x B_2H_6 samples; b) R_T *vs*. d_s for Ti/Au on the GeSn:B samples; c) IV plot extracted from the TLM device with ds=3 μm, of the GeSn:As samples; d) Thermionic field emission lower limits (LL) and upper limit (UL) for n-type carriers in $Ge_{1-x}Sn_x$: $0 < x < 0.2$. 74

LIST OF SYMBOLS AND ABBREVIATIONS

AFM Atomic force microscopy

As Arsenic

AsH_3 Arsine

B Boron

B2B Back-to-back

B_2H_6 Di-Borane

CMOS Complementary metal–oxide–semiconductor

CNL Charge neutrality level

CTLM Circular transmission line model

CV Capacitance-voltage

CVD Chemical vapor deposition

ED Energy density

FE Field emission

FET Field-effect transistor

FLP fermi-level pinning

Ge Germanium

GS Gap-states

IR Infrared

IV Current-voltage

LTA Laser thermal annealing

MIS Metal-interface-semiconductor

MOS Metal-oxide-semiconductor

MS Metal-semiconductor

MSM	Metal-semiconductor-metal
Ni	Nickel
OEIC	Optoelectronic integrated circuit
PIC	Photonic integrated circuit
RMS	Root mean square
RSM	Reciprocal space mapping
RTA	Rapid thermal annealing
SBH	Schottky barrier height
SCR	Space charge region
Si	Silicon
SIMS	Secondary ion mass spectrometry
Sn	Tin
SWIR	Short-wave infrared
TE	Thermionic emission
TEM	Transmission electron microscope
TFE	Thermionic-field emission
Ti	Titanium
TL	Top layer
TLM	Transmission line model
V	Vacancy
VS	Virtual substrate
XRD	X-ray diffraction

CHAPTER 1 INTRODUCTION

1.1 Context

Although silicon- (Si-) based electronics technology is ubiquitous in today's society and has a transformative impact on our daily lives, its Si-based photonics counterpart is still in its infancy. This is particularly true for active and efficient devices operating in the short-wave infrared (SWIR:1.4–3 µm) and mid-infrared (MIR: 3–8 µm) spectral ranges. This limitation stems from the inherently indirect bandgap structure of the commonly used group-IV semiconductors, [1] namely germanium (Ge) and Si, which limits the photon absorption or emission efficiencies. In this regard, germanium-tin (GeSn) alloys have recently been developed to tackle these challenges. They provide a direct bandgap group-IV system, [2] that can be tuned to operate efficiently in the SWIR and MIR spectral ranges, and can be monolithically grown on Si platforms [3]. Their monolithic growth on Si wafers makes them compatible with complementary metal-oxide-semiconductor (CMOS) approaches, which could pave the way to implement scalable innovative photonic and electronic devices on the same chips [4]. This potential makes the long-sought-after all-group-IV photonic integrated circuits (PICs) and optoelectronic integrated circuits (OEICs) closer to realization. Indeed, various GeSn-based optoelectronic (OE) structures have already been demonstrated in recent years [5-9]. PICs and OEICs offer robust platforms that may usher in a new era of technologies. For instance, these technologies would bring a paradigm shift in data transmission by providing effective building blocks to replace copper-based interconnects by photonic ones for inter- and intra-chip communications. This would solve the current technological bottleneck in optical communications and datacomm by allowing faster communication speeds, larger broadbands, and reduced energy consumption resulting from thermal losses in copper-based interconnects.

If successful, all-group-IV photonics would be the cornerstone of an environmentally friendly infrastructure for future Internet and Internet-of-things (IoT) [10]. Moreover, since multiple chemical bonds exhibit a distinct and strong absorption lines in the SWIR and MIR spectra as a result of molecular vibrations, GeSn alloys can also be used as an active sensing material for the spectral identification of a variety of key molecules, such as CO_2, toxic gases, and organic materials [10]. Thus, SWIR/MIR PICs and OEICs based on GeSn can provide viable long-term solutions to

many problems across multiple sectors, [10] including integrated sensors in *lab-on-a-chip*, hyperspectral imaging modules for biomedical applications, gas sensing, and gas imaging, SWIR/MIR vision for military surveillance and self-driving cars, and consumer OEICs for smartphones or wearables [10, 11]. Furthermore, the development of fully monolithic GeSn-based IR active photonic devices, such as integrated photodetectors and lasers, is considered a major leap towards the large-scale manufacturing of cost-effective and high-resolution IR photonic components, operating at room temperature [12]. Additionally, GeSn-based devices offer a powerful alternative to group II–VI and III–V compound materials, which are costly and suffer from limited integration on Si-based electronics. The monolithic growth of GeSn on Si wafer offers scalability, manufacturability, and cost-effectiveness.

Besides the potential of GeSn in Si photonics, this material system has also attracted attention for nanoelectronic applications [4]. In fact, GeSn is currently explored as a next-generation channel material in field-effect transistors (FETs), [13] since the effective masses of holes and electrons are expected to be lower in GeSn as compared to Ge. These characteristics are highly important to enhance the performance of FETs, for instance, by lowering the switching delay [14]. In addition, the direct and small bandgap in GeSn is perfect for enhancing electron band-to-band tunneling, which makes it suitable for tunnel-FETs (TFETs) [15].

Given the potentially broad impact of GeSn-based materials, their success relies on controlling and optimizing their basic properties throughout device processing to engineer their functionalities and improve their performance. One integral and common component in all semiconductor-based devices is the ohmic contacts [16]. These are the essential electrical connections established to drive a current in and out of the device, without impacting the intended performance of its active parts, and with minimal thermal losses induced by Joule heating [17]. To be more specific, the current in metal-semiconductor (M-S) contacts has to vary linearly as a function of the applied voltage bias, *i.e.*, an ohmic behavior, and the corresponding parasitic resistance has to be sufficiently minimized by optimizing the contacts [17]. In addition, the contacts must be optimized for both n-type and p-type doped GeSn layers, as they are needed to implement functional devices. In principle, one has to establish optimal processing conditions for a wide range of doping levels (10^{17}–10^{20} cm^{-3}) and Sn concentrations (5–20 at.% Sn), which are relevant for SWIR/MIR optoelectronics.

For Ge- and GeSn-based devices, achieving optimal contacts is especially difficult, since optimizing the metal work function alone is not sufficient to obtain low contact resistance on p-type and n-type layers. This is even more problematic for n-type junctions [18]. It results from the presence of interface states that pin the FL near the VBE, and this effect is 10x more intense in Ge and GeSn than in Si as a result of their higher interface states' density [18]. Thus, addressing this challenge is crucial, and it must be carried out in a manner that does not influence or degrade these materials, especially since most straightforward processes require post-growth thermal annealing of the contacts [19]. This is particularly true for GeSn at a Sn-content above 7%, which is highly metastable and can only sustain thermal processing below a temperature threshold above which phase separation occurs. Consequently, this thesis addresses these bottlenecks by establishing experimental protocols that target the development of low-resistance contacts to GeSn, while taking into consideration the peculiarities of GeSn alloys, and the nature of GeSn contacts. This is realized by the development of a post-growth low thermal budget processing solution for the treatment of metal-GeSn contacts, which is compatible with the restrictions identified above, additionally, by carrying out systematic studies targeting the control of the n-type and p-type doping processes of GeSn. The established experimental protocols can also be exploited to functionalize other GeSn-based heterostructures and nanoscale devices, such as nanowires and nanomembranes.

1.2 Research objectives

The aim of this project is to develop and optimize low resistance ohmic contacts on GeSn. To accomplish this aim, the work carried out throughout this project was articulated around the following scientific and technical questions:

(1) How can low resistance ohmic contacts on high Sn-content (up to 11.2 at.%) GeSn be achieved? (2) How can metal/GeSn contacts be annealed without compromising the material's structural quality and degrading its properties? (3) How can efficient p-type and n-type doping processes be devised for GeSn thin films? (4) What is the impact of dopant incorporation on their quality and electrical performance? (5) How can the electrical properties of doped GeSn be appropriately measured?

To address these questions, this work focused on the following objectives:

(1) Assessing the compatibility of conventional and CMOS-compatible Si and Ge processing methods with high Sn-content GeSn;

(2) Developing a low thermal budget treatment to improve the electrical properties of metal contacts on GeSn without degrading its structural quality;

(3) Establishing a wide range of doping levels and studying the impact of doping on the properties of GeSn thin films;

(4) Designing and microfabricating test structures to characterize the doping level and the specific contact resistance of M-S devices.

1.3 Thesis outline

This thesis is organized into six chapters to establish and discuss different methods to obtain ohmic contacts on high-Sn-content GeSn. Chapter 2 provides a review on GeSn growth and properties, and theoretical background and state-of-the-art processes for electrical contact engineering on Ge and GeSn. Chapter 3 includes a general description of the methods and techniques used in this work. Chapter 4 presents the impact of laser thermal annealing on the properties of high Sn-content GeSn and Ni/GeSn contacts. Chapter 5 discusses *in situ* dopant incorporation and its effect on the properties of high Sn-content GeSn. Finally, a summary and future perspectives related to this work are presented in Chapter 6.

CHAPTER 2 LITTERATURE REVIEW

2.1 Metastable GeSn alloys: from theory to experimental realization

The following brief review on GeSn is provided to better appreciate our interest in this material system, its growth, its electronic properties, and the fundamental limits faced in developing low resistance ohmic contacts on GeSn. The first mention of GeSn alloys was in 1982 in a theoretical work that shed light on their potential as direct bandgap semiconductors [20]. A few years later, other studies supported these observations, and stressed on the possibility of achieving a direct bandgap at 8.6 at.% Sn-content, lower than initially expected [21]. However, the progress and impact of the early studies were limited by multiple factors. The first is the intrinsic low solid solubility of Sn in Ge, which is of about 1 at.% Sn resulting from the large difference (∼14.7%) in covalent radius between Ge (1.225 Å) and Sn (1.405 Å) [22]. The second factor is the unavailability of growth methods suitable for the fabrication of high Sn-content GeSn at that time [23]. In the following years, novel growth techniques marked a milestone for the revival of interest in GeSn, as they allowed for a better control of the material's quality [24]. This motivated many researchers to understand and implement GeSn-based devices. Currently, this research area transformed into a race towards the development of mature GeSn technology, which can be transferred towards large-scale fabrication [21].

The potential to engineer the band structure and achieve a direct bandgap in GeSn results from two facts. The first is the small separation of 140 meV between the indirect (L) and direct (Γ) conduction band valleys in bulk Ge. The second is that Sn incorporation at increasing concentrations reduces this separation, which happens by lowering the Γ valley at a higher rate than the L valley, [25] as plotted in Fig. 2.1. Combining these effects leads to an indirect-to-direct bandgap transition, or "crossover point", at around 10 at.% Sn [2]. Furthermore, this crossover point was extensively studied, and it was found to depend not only on the Sn-content, but also on the strain in the layer. Indeed, GeSn are typically compressively strained as their growth on Si uses Ge as an interlayer. This residual strain shifts the crossover point to higher Sn-content, and lowers the emission wavelength of GeSn at a fixed Sn-content [2, 26]. Thus, processes realized in this work were developed for high Sn-content, relaxed GeSn films.

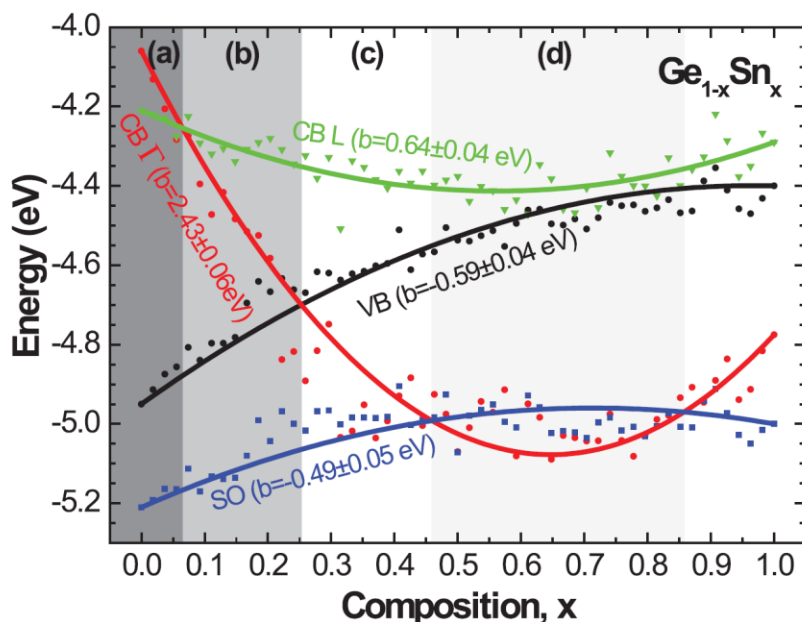

Figure 2.1 Γ and L conduction bands (CB), valence band (VB), and spin-orbit split-off (SO) energies plotted relative to the vacuum level for the relaxed $Ge_{1-x}Sn_x$. The first two dark shades of gray represent indirect and direct bandgap GeSn, respectively. Reprinted [27] with permission from Polak, M.P., P. Scharoch, and R. Kudrawiec, The electronic band structure of $Ge_{1-x}Sn_x$ in the full composition range: indirect, direct, and inverted gaps regimes, band offsets, and the Burstein–Moss effect. Journal of Physics D: Applied Physics, 2017. 50(19). Copyright 2017 IEEE.

The successful growth of GeSn with an order of magnitude higher Sn incorporation than the equilibrium limit of Sn in Ge is an arduous task [3]. Establishing such a process depends heavily on the concomitant development of non-equilibrium growth techniques, which enable growth at low temperatures to kinetically suppress Sn surface segregation and phase separation [3, 28]. Historically, the growth of GeSn was first explored using physical vapor deposition (PVD) techniques, such as molecular beam epitaxy (MBE) [29] and pulsed laser crystallization of amorphous sputtered films [23]. These methods were limited by their very low growth rates and lack of uniformity in the fabricated GeSn layers. Moreover, PVD grown layers are often thin and compressively strained, which lowers the capacity to control their morphological and crystalline quality [21]. The next development in GeSn growth was marked by the establishment of stable

chemical precursors for Sn and Ge, which are dedicated to the growth of GeSn using chemical vapor deposition (CVD) detailed later on. These are monogermane (GeH_4) and tin-tetrachloride ($SnCl_4$), which are currently the major precursors used in the CVD growth of GeSn. GeH_4 is highly stable and cost-effective. Because of its accessibility and stability, $SnCl_4$ enables the CVD growth in both atmospheric and reduced pressures. Finally, the CVD growth of GeSn epilayers using these precursors is usually realized at a temperature window of 250-400 °C [3, 30-32].

The successful growth of metastable GeSn epilayers with high Sn-content on Si wafers relies on minimizing the strain induced on each of the stacked layers, *i.e.,* reducing the lattice mismatch between these layers. The goal is to avoid phase separation and Sn-segregation during the growth. For this purpose, and given the lattice constant of the corresponding cubic diamond crystalline structures for pure Si (a_{Si}= 5,4307 Å), Ge (a_{Ge} 5.657 Å), and α-Sn (a_{Sn}= 6,4912 Å), the growth of high Sn-content GeSn on Si is typically realized as follows. First, a Ge virtual substrate on a Si wafer (Ge-VS/Si) is grown with a thickness of a few µm. The structure is then annealed *in situ* with a cyclic process to reduce the dislocation density caused by the lattice mismatch between Si and Ge [33-35]. Next, GeSn epilayers with step-graded Sn-contents are grown, each having a layer thickness that exceeds the critical thickness allowing for plastic strain relaxation, which results from the nucleation of dislocations close to the interface with the Ge-VS. This growth layout can yield uniform high Sn-content GeSn [3, 36, 37]. In fact, it was followed in a previous study to fabricate GeSn heterostructures with atomically homogeneous 18 at.% Sn GeSn top layers (TLs) [32]. We note that the growth parameters of these heterostructures need to be optimized to control strain relaxation during the growth and restrict defects induced by lattice-mismatch to the bottom GeSn layers, thereby achieving defect-free high Sn-content TLs, which preserves their basic properties.

Because of the low thermal stability of GeSn, the material is highly sensitive to post-growth thermal treatments [38]. For this reason, a critical temperature that is close to the growth temperature is determined as an upper-limit to functionalize devices using post-growth treatments. Processing samples at temperatures above this critical limit activates Sn diffusion, which leads to phase separation and surface segregation. This results in the formation of β-Sn droplets with diameters of few µm on the surface, while the residual GeSn shows a reduced Sn composition at the equilibrium content (1 at.% Sn) [28, 36]. Moreover, it was revealed that the presence of threading

dislocations enhances Sn diffusion around the dislocations' core during the growth. This mechanism is known as pipe diffusion, and it could be considered as a faster Sn diffusion route in relaxed GeSn layers compared with pseudomorphic ones [28]. Overall, this critical temperature is sensitive to the growth method, Sn-content, and strain. For instance, it should not exceed 320 °C for CVD-grown partially-relaxed GeSn with 12 at.% Sn, as established in [39], whereas this critical temperature goes down to 230 °C for MBE-grown pseudomorphic GeSn with 10 at.% Sn [40]. Thus, careful considerations must be taken in the development of post-growth treatments. The processing temperature needs to be compatible with these instabilities to preserve the integrity and the optical performance of GeSn layers. Hence, high-temperature treatments typically used for Ge processing are inherently incompatible with high Sn-content GeSn, as discussed in Section 2.3, for example, rapid thermal annealing (RTA) for metal contacts processing on Ge at 350 °C, [41] ion implantation and activation for n-type and p-type doping using conventional processing at temperatures above 400 °C, [42] and finally, the ALD growth of high-*k* dielectrics at 350 °C [43].

2.2 Metal-Semiconductor contacts

As discussed earlier, optimizing the M-S interfacial properties is central to achieve ohmic contacts on both n-type and p-type regions and minimize the contact resistance. In this section, we discuss the physical properties of electrical contacts in a general sense, and how their properties influence these devices' performance. First, we introduce the case of ideal contacts, and we define the Schottky barrier height and how it affects current transport in these junctions. Second, we detail the effect of varying the doping level (N) on electrical contacts' current transport properties. Finally, we introduce the specific contact resistance (ρ_c) as a figure-of-merit for contact engineering, which will be used later to assess the contact performance of devices fabricated in Chapters 4 and 5.

2.2.1 Ideal Schottky barriers

The current flow in most abrupt M-S contacts is restricted by the presence of a potential barrier. The latter results from the discontinuity in the electronic structures of the metal and the semiconductor, as displayed in Fig. 2.2.a [17]. A simple and ideal representation of the barrier's origin for a metal layer on a lightly doped n-type semiconductor substrate is displayed in Fig. 2.2.

The resulting Schottky barrier height (SBH) is denoted by ϕ_B, ϕ_M is the metal's work function, χ_s is the semiconductor's electron affinity, E_c its conduction band edge (CBE), E_v its valence band edge (VBE), E_f its fermi level (FL), and E_G its bandgap. When the M and S layers are in direct contact (Fig. 2.2.b), majority carriers (e^-) are transferred from the semiconductor side to the metal until an equilibrium of their fermi-levels is reached. This leads to the formation of a charge-depleted region called the space charge region (SCR) in the semiconductor. The SCR is characterized by its width (w) and a Schottky barrier height (ϕ_B). The value of the latter can be calculated using E.q. 2.1, given by:

$$\phi_B = \phi_M - \chi_s \tag{2.1}$$

The first mathematical model that describes this ideal case is the Schottky-Mott model published in 1939 [44, 45]. Hence, the ideal case is often referred to as the "Schottky-Mott limit" in the literature. Most importantly, for $\phi_B > 0$, the junction exhibits a rectifying behavior, whereby the flow of e^- is restricted from the metal to the semiconductor and allowed in the opposite direction. On the other hand, for $\phi_B \leq 0$, an unrestricted flow in both directions is allowed. These types of junctions are referred to as neutral and accumulation contacts for $\phi_B = 0$ and $\phi_B < 0$, respectively. However, they are not included in this description nor in the following sections, since they are rarely encountered in real contacts on most semiconductors, and this also extends to Ge and GeSn contacts. Moreover, for electrical contacts on p-type semiconductors, an analogous description is applicable, since the same physics govern the transfer of majority carriers, except that the sign of ϕ_B is the opposite for a similar behavior on n-type semiconductors.

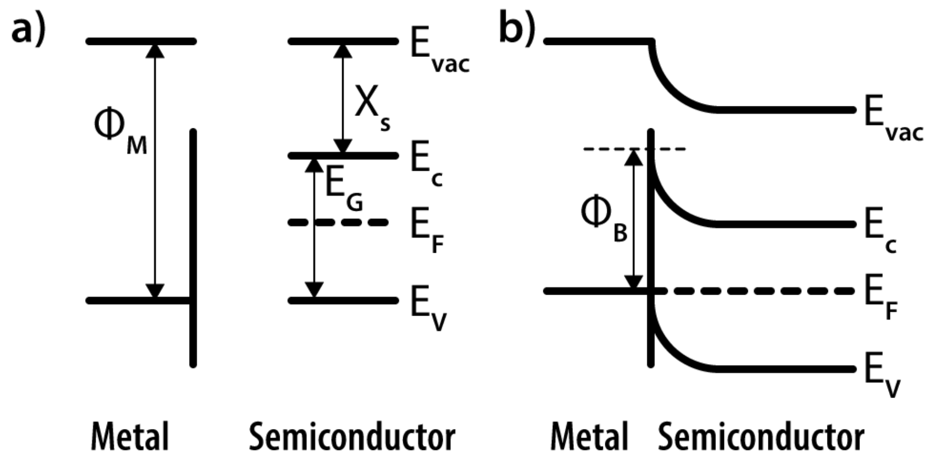

Figure 2.2 Sketch of the band diagram of a) separate M and n-type semiconductor (n-S), b) an M/n-S contact. Adapted from [17]

2.2.2 Influence of the doping level on the current transport in M-S contacts

Here, we address the current transport mechanisms in M-S junctions with $\phi_B > 0$ at various doping levels, *i.e.,* at different active carrier concentration in the semiconductor region. Since the doping level acts on the barrier's width as $W \sim N_D^{-1/2}$, [17] three main current transport mechanisms originate at various active carrier concentration ranges. These mechanisms govern charge transfer of majority carriers in M-S contacts, as illustrated in Fig. 2.3.

.

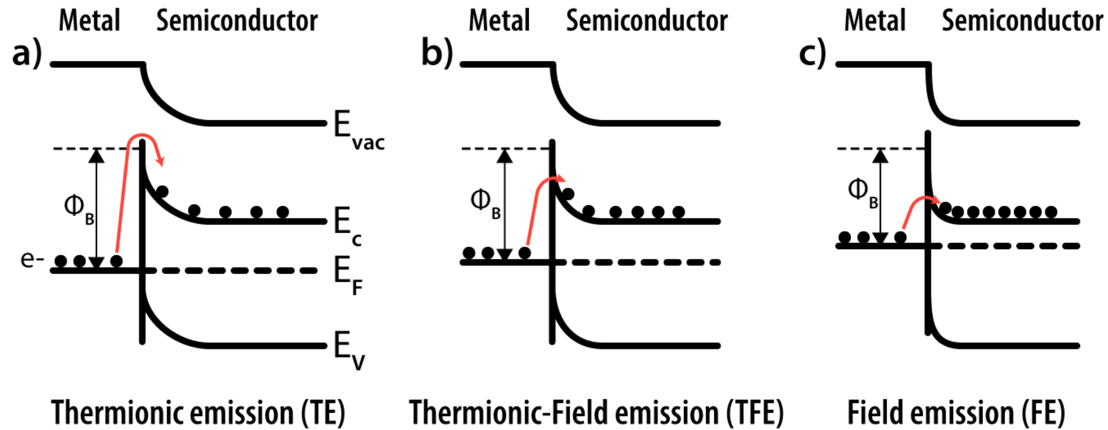

Figure 2.3 Sketch of the current transport mechanisms in Metal/n-S contacts a) at low, b) moderate, and c) high doping levels. Adapted from [17]

For low doping levels (Fig. 2.3.a), the SCR's width is very large, and the dominant transport mechanism is thermionic emission (TE). In this case, only thermally excited electrons that have enough energy to jump above the barrier contribute to the current flow. Hence, the junction's behavior is rectifying, which reflects on its current-voltage (IV) curve. For instance, in a M-S junction with a low n-type doping level, the current is proportional to the applied voltage at positive biases. In contrast, negative biases here yield a low and stable current value [17]. For very high doping levels (Fig. 2.3.c), the SCR is very narrow and the semiconductor's FL is near the conduction band edge (CBE). These conditions allow for electrons to tunnel through the barrier despite the presence of a high SBH, which yields a linear IV curve, *i.e.,* and ohmic behavior. The dominant current transport mechanism here is referred to by field emission (FE) [17]. Finally, for intermediate doping levels (Fig. 2.3.b), thermionic field emission (TFE) dominates current transport. The barrier here is only thin enough at a certain energy level. Thus, the current flow is dominated by electrons with enough thermal energy to jump above this barrier difference and tunnel through the SCR [17]. Moreover, since the applied voltage on the M-S junction affects the SCR's width, a near-ohmic behavior is observed in the IV curves in TFE. Generally, distinguishing between these current transport mechanisms at different doping levels is done by comparing the

tunneling probability (E_{00}) of the M-S junction to the thermal energy (kT), as described in Section 5.5.

Furthermore, as implied in Fig. 2.3, there exists a weak relationship between the SBH and the doping level. It results from the image-force lowering mechanism, and its details are well-documented in [46]. The effect of this mechanism increases with the doping level following $\Delta\phi_B \sim N_D^{1/4}$relationship, where $\Delta\phi_B$ is the reduction that is caused by image-force lowering from the absolute SBH value ϕ_B. Thus, this mechanism can contribute to the current flow especially at high doping levels. For instance, it needs to be accounted for in M-n-Ge contacts with doping levels above 10^{19} cm^{-3} [47]. The exact values for $\Delta\phi_B$ of a M-S junction can be experimentally measured as well. This is done by calculating the difference in the absolute SBH value extracted from CV (capacitance-voltage) measurements and the effective SBH from IV measurements.

2.2.3 The resistance of ohmic contacts

As discussed earlier, on top of achieving an ohmic behavior during the optimization process of M-S junction, it is equally important to minimize the total resistance R_T to guarantee the proper functionality of devices that implement these junctions. R_T is composed of three series resistances. The first is the metal resistance R_M. It can be minimized by optimizing the metal stack's sheet resistance using a thick metal layer, or alternatively, by using layered metal stacks, such as those commonly used for the fabrication of devices based on III-V compound semiconductors [48]. The second is the semiconductor resistance R_S, which is directly controlled by an inverse relationship with the doping level. Finally, the interface's contact resistance R_C, which is the general limiting factor in the design of high-performance M-S ohmic contacts, and the most crucial element in the optimization process. The latter is studied by calculating the specific contact resistance (ρ_c), which a figure-of-merit given by:

$$\rho_c = \left.\frac{\partial V}{\partial J}\right|_{V=0} in\ (\Omega.\mathrm{cm}^2), \tag{2.2}$$

whereby J is the current density (A/cm^2).

The $\rho_c = f(N, SBH)$ equations, where N is the doping level, for each of the three current transport mechanisms are extensively detailed in [17]. Here, we only describe the effect of N and the SBH

on the values of ρ_c for these different mechanisms. Starting with low doping levels where TE is dominant, ρ_c here is mainly controlled by the SBH. As for moderate doping levels, TFE is dominant, and both of the SBH and N notably affect ρ_c. An example of this trend for n-Ge is found in Fig. 2.4 [49]. Finally, for high doping levels, FE is dominant, and ρ_c is mainly affected by N.

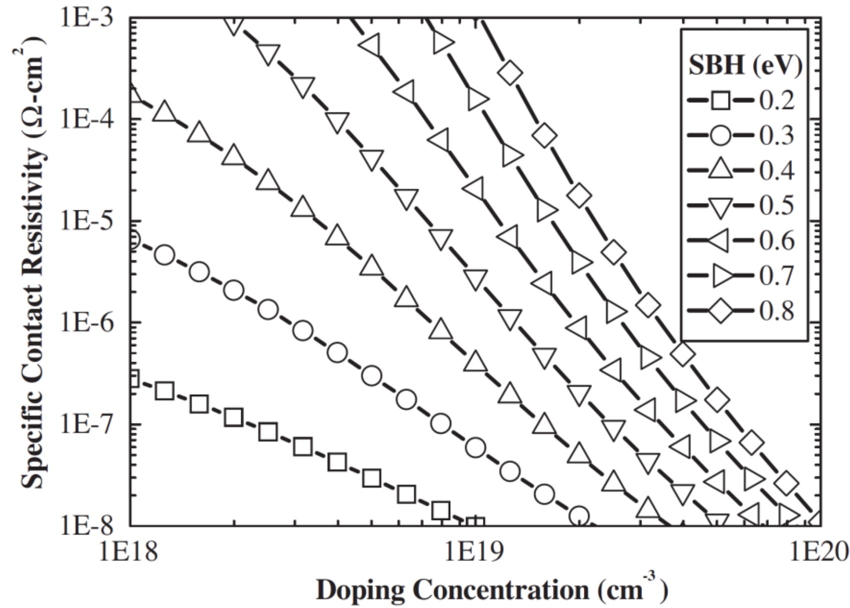

Figure 2.4 Calculated results on the behavior of ρ_c in TFE as a function of the doping level and SBH for n-type Ge. Reprinted [49] Firrincieli, A., et al., Study of the impact of doping concentration and Schottky barrier height on ohmic contacts to n-type germanium. Microelectronic Engineering, 2013. 106: p. 129-131. (2013) With the permission of Elsevier B.V.

From Fig. 2.4, it is clear that achieving high doping levels is crucial to reduce ρ_c. In fact, the lowest ρ_c values reported in the literature for GeSn are in the order of 10^{-9} Ω.cm^2 for heavily doped (10^{20} cm^{-3}) n^+-$Ge_{0.94}Sn_{0.06}$, [50] and in the 10^{-10} Ω.cm^2 range, close to its physical limit called Landauer limit, [51] for p^+-$Ge_{0.93}Sn_{0.07}$ (10^{20} cm^{-3}) [52, 53]. These high doping levels can be achieved through conventional ways discussed in Chapter 5, and using emerging methods that include, and not restricted to, surface segregation of dopants during germanidation [54, 55] and carrier activation techniques [56]. All of these techniques were successfully implemented to reach ultra-low ρ_c in n-

Ge, and could potentially be implemented in GeSn as well. However, the sole optimization of the doping level is not a viable solution for the design of efficient ohmic contacts. Controlling the SBH plays an essential role to further improve the contact's performance and achieve the targeted ultra-low ρ_c values. For this reason, we discuss in the next section the SBH of real electrical contacts on Ge and GeSn.

2.3 Ge- and GeSn-based real contacts and Fermi Level-Pinning

We start this section by detailing the real case of fabricated Ge- and GeSn-based contacts and their electrical performance. Next, we introduce fermi-level pinning as the mechanism of origin of this divergence from the ideal case, and the existing layout structures that were designed to circumvent this issue. Finally, we showcase the implications of the Sn-content on the intrinsic contact properties, and on the effectiveness of M-S structures in solving the contact problem for high Sn-content GeSn.

In reality, the values of real SBHs diverge from the equation given by the Schottky-Mott model (E.q. 2.1) for almost all M-S contacts [17]. This divergence arises from the presence of intrinsic interface states or gap states (GSs) in the semiconductor's side of the junction. GSs are different in their electronic structure from that of bulk states. However, these GSs have donor-like and acceptor-like levels just as in bulk semiconductors. Their distribution yields a charge neutrality level (CNL) measured in eV, which has the same analogy to bulk FL. If the distribution of GSs falls inside the forbidden bandgap of the semiconductor's bulk, their influence on majority carriers' transport becomes notable. For instance, in n-type semiconductors, if the CNL is below the FL of the bulk, the interface's acceptor-like states become negatively charged, *i.e.* occupied, which leads to a band-bending to establish charge equilibrium between the interface and bulk. Thus, the FL near the interface becomes pinned to the CNL.

Regardless of these states' origin, their presence in a M-S contact can significantly affect the junction's behavior, whereby the SBH modulation by the metal work function becomes less effective. This case was first described by the Bardeen model [57] and was later given the term fermi-level pinning (FLP) [58]. In this case, the SBH equation is given by:

$$\phi_B = S(\phi_M - \chi) + (1 - S)\phi_{CNL} \quad (2.3)$$

Here, $S = \frac{\partial \phi_B}{\partial \phi_M}$, which is the slope of $\phi_B = f(\phi_M)$ curve. It is a dimensionless factor that is directly proportional to the density of GSs [59]. A value of $S = 0$ is referred as "the Bardeen limit", in which a complete loss of SBH modulation via ϕ_M occurs. In contrast, a S value of 1 leads back to the Schottky-Mott limit.

For Ge-based contacts, the FLP is strong. Experimentally-extracted S values vary in the 0.02-0.05 range, whereas the CNL is exactly at 0.09 eV above the VBE [18, 60]. We note that the S value in Ge is an order of magnitude lower than that reported for Si. As a result, almost all pure and non-processed metal contacts on p-Ge/n-Ge are ohmic/Schottky, respectively, regardless of their ϕ_M values. The latter was previously revealed in systematic experiments that showed a high disparity between the variation level in ϕ_M and the corresponding SBHs, as illustrated in Fig. 2.5.

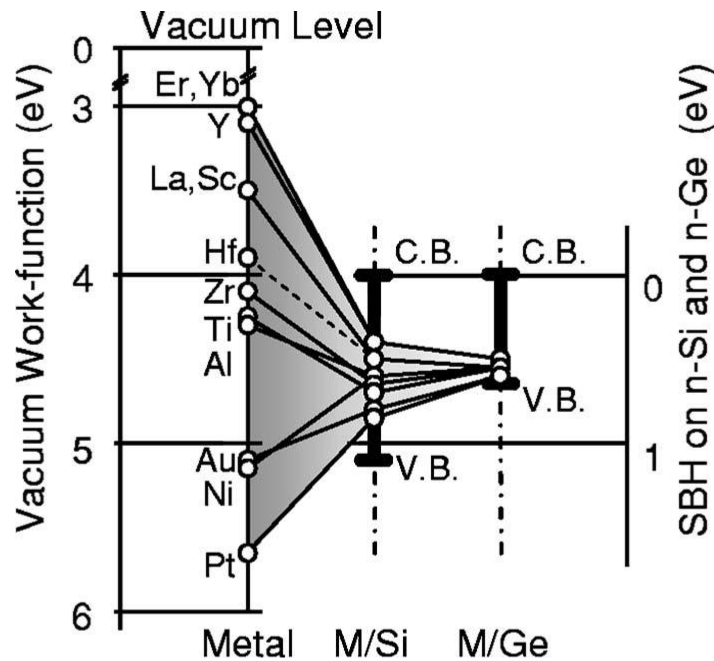

Figure 2.5 Experimentally obtained electron SBH on n-Si, n-Ge, and the corresponding original ϕ_M. Reprinted [18] Nishimura, T., K. Kita, and A. Toriumi, Evidence for strong Fermi-level pinning due to metal-induced gap states at metal/germanium interface. Applied Physics Letters, 2007. 91(12).

As discussed earlier, the S factor is directly proportional to the density of GSs. Thus, it is essential to list the extrinsic mechanisms that affect the density of GSs, to understand the functionality of layout structures for ohmic contacts designed to lower this density, thereby alleviating FLP [61]. In brief, the origin of the FLP in most group-IV semiconductors has been explained through various models. First, the metal-induced gap states (MIGS) model, [62] which correlates the metal states' influence on FLP. GSs in this model can be mitigated by using low electron density contacting layers, or by forming an interlayer that separates the metal from the semiconductor, which reduces GSs' effect. Second, the other mechanisms that can be controlled, *i.e.* possibly engineered, are related to the semiconductor's interface structure and the presence of defects at the M-S interface, such as dangling bonds [63].

In Ge and Si, it has been thoroughly proven in multiple systematic experimental studies and *ab initio* calculations that MIGS are dominant [18, 63-66]. Moreover, controlling other-defect related mechanisms helps in approaching the Schottky-Mott limit at a wide range of doping levels for these devices [67]. However, for GeSn, exact knowledge on the strength of FLP as a function of Sn-content and strain, *i.e.* the S factor and CNL values, is still missing in the literature. However, a strong FLP behavior was demonstrated in GeSn for multiple studies that treated this aspect in a non-systematic manner, [68] and generally in all ohmic contacts formation studies on GeSn [50, 69].

2.3.1 Fermi-level depinning solutions to Ge and GeSn contacts

In this section, we review the performance and intrinsic limitations of the various structures designed to alleviate FLP in Ge-based contacts at a wide range of doping levels. Moreover, we reveal the possibilities of applying these methods to GeSn alloys by reviewing their compatibility with post-processing limitations of GeSn, and their flexibility at a high Sn-content range.

2.3.1.1 The Metal-Semiconductor layout

The first type of structures dedicated to ohmic contact formation is the M-S alloyed contacts. These have been conventionally used for fabricating Si-based devices in the CMOS industry for decades, and are still in use currently [70]. In the M-S layout, the pure metal is alloyed with the

semiconductor to achieve silicide (M_xSi_{1-x}), germanide (M_xGe_{1-x}), or stanogermanide ($M_x(Ge_{1-y}Sn_y)_{1-x}$) contact layers, for Si-, Ge-, and GeSn-based contacts, respectively. As a result, lower sheet resistance and higher active contact areas are achieved after alloying [16]. Moreover, the electronic structure of these phases helps in alleviating the FLP as a result of their 100x lower electron carrier density compared with pure metals, [67, 71] which lowers the density of MIGS, as discussed in the previous section. However, a fixed S factor cannot be applied to all phases formed for a specific semiconductor using different metals and processing treatments. The alloys' crystalline structure and interface quality with the semiconductor affect FL depinning as well [67, 71].

For Ge and GeSn, nickel-based alloyed contacts are the predominantly studied in the literature, despite the high work function of nickel $\phi_{\mathrm{Ni}} = 5.15\ eV$ [72]. This is because a NiGe phase can form at a temperature of 325°C, and maintain its properties during annealing with no corrosion signs [73]. Moreover, NiGe offers the lowest resistivity value relative to other metal germanides [41, 74, 75]. For GeSn, the equivalent stanogermanide is the stochiometric $Ni(Ge_xSn_{1-x})$ [76, 77]. Fabrication of the later on a n^+-$Ge_{0.94}Sn_{0.06}$ layer recorded the lowest ρ_c reported in the literature, with values in the 10^{-9} $\Omega.cm^2$ range [50].

2.3.1.2 The Metal–Interlayer–Semiconductor layout

The second type of ohmic contact structures is metal–interlayer–semiconductor (M-I-S) contacts. These are recognized by the presence of an interfacial layer (IL) between the metal and the semiconductor. There exist two types of ILs depending on their electrical properties. The first is semiconducting ILs. These layers are epitaxially deposited before metallization. They rely on their epitaxial quality to lower the density of surface defects, and their thickness to reduce the MIGS' density by separating the metal from the semiconductor. For Ge and GeSn, the reported semiconducting ILs include Si ILs, [78] lattice-matching SiGeSn, [79] Sn-rich GeSn ILs, and surface segregated GeSn [80, 81]. Pure Sn or high Sn-content GeSn ILs demonstrated an even lower SBH on n-Ge than the former semiconducting ILs. This results from the strong FLP near the VBE in GeSn, and upward shift of the VBE for increasing Sn concentrations, which offsets the SBH to n-Ge. Other semiconducting ILs include using 2D materials, such as multilayer black phosphorus IL, [82] and multilayer graphene, [83] and their effectiveness is similar to Si ILs.

The second category of ILs is tunnel barriers. They consist of ultra-thin (< 10 nm) oxide or nitride layers, and their primary function is to separate the metal from the semiconductor to reduce the density of MIGS. A S factor near unity, *i.e.* at the Schottky-Mott limit, can be reached using this method [84-87]. In fact, a neutral SBH was already reported for Ge_3N_4 ILs on n-Ge [88]. However, one of the drawbacks of tunnel barriers is that even after optimizing the IL thickness, the resistance in M-I-S devices is limited by the tunneling probability of e^- through the IL, especially at high doping levels. Minimizing this resistance relies on reducing the conduction band offset (CBO) between the IL and the n-type semiconductor. This process reduces the choice of tunneling ILs to few options. The most efficient M-I-S structures with tunnel barrier ILs for n-Ge consist of Ti or Al metals, and ALD deposited TIO_2 [89-91] and ZnO [92] oxides.

However, despite the meticulous choice of these materials, tunnel barriers are effective in reducing ρ_c only at moderate doping levels (< 10^{19} cm^{-3}), [93] since their tunneling resistance becomes dominant at higher doping levels. This also extends to doped tunnel barriers specifically designed to lower this resistance [94]. Therefore, M-I-S with tunnel barrier structures are not viable for semiconductors with higher doping concentrations. Moreover, M-I-S structures with tunnel barriers on Ge require the use of reactive metals, as discussed earlier. The latter makes it harder to preserve their optimized properties upon thermal annealing, since the metal can react with the barrier and reduce its optimal thickness even at a low temperature of 250°C [95]. Moreover, since the CBO between the IL and the semiconductors' CBE needs to be minimized, and given the downward shift of the CBE with increasing Sn-content in GeSn (Fig. 2.1), tunnel barriers optimized for Ge contacts cannot be extended to GeSn.

2.3.2 Effect of Sn incorporation on the performance of ohmic contacts on GeSn

Regardless of the contact layout type, it is crucial to be aware of the other GeSn material-related intrinsic factors that affect the ohmic junction's performance. This helps in designing contacts tailored for GeSn with higher Sn-contents (above 10 at.% Sn). These effects are related to the variation of the bandgap in GeSn as a function of the Sn incorporation. The first direct and positive implication of increasing the Sn-content is the reduction of SBH to n-GeSn, given the FLP. The latter is a result of the combined effect of strong FLP near the VBE that persists in GeSn, and the upward shift in this VBE for higher Sn contents (Fig. 2.1).

Secondly, it was found through modeling of ρ_c of M/n-$Ge_{1-x}Sn_x$ ($0 \leq x < 0.11$) junctions at a wide doping range, that by increasing the Sn-content, *i.e.* reducing the offset between the L valley and Γ valley, the Γ valley can accommodate a higher electron population [96]. This enhances electron tunneling from the metal to the Γ band. Thus, further increasing the Sn-content above the crossover point makes Γ valley the dominant band for current transport. Furthermore, the effective mass of electrons in the Γ band reduces significantly by increasing the Sn-content [97]. Hence, ρ_c is positively affected following that trend. However, this enhancement is only possible for active concentrations below 10^{20} cm^{-3}, for which tunneling to the Γ valley is dominant with its lower effective mass. For higher doping levels, tunneling to the L band remains dominant for high Sn-content GeSn as a result of its higher density of states. Moreover, given the fact that the Sn-content does not influence the L band's effective mass [97]. ρ_c values remain similar for increasing Sn concentrations at doping levels above 10^{20} cm^{-3}. One way to reduce ρ_c in junctions with doping levels above 10^{20} cm^{-3} is to use metals with higher effective masses, which increases the tunneling probability in the L valley [96].

2.3.3 Contact solutions for GeSn with high Sn content

As demonstrated earlier, M-S structures will remain the optimal solution for achieving ultra-low ρ_c in semiconductors used in the CMOS technology [95, 98]. For GeSn, Ni-based M-S structures provided the lowest ρ_c reported on n-GeSn, [50] and were selected as the best contacts for GeSn with 8 at.% Sn among other metals based on their thermal and electrical properties [19]. Therefore, it is equally important to address the effect of Sn incorporation in GeSn layers on the formation of Ni-based alloys with GeSn. It was found that increasing the Sn-content in GeSn layers having similar strain values increases the formation temperature of this phase [99]. Furthermore, $Ni(Ge_xSn_{1-x})$ has a lower thermal stability than NiGe, and its sheet resistance degrades faster with increasing temperatures relative to NiGe [19, 99]. For GeSn with Sn content above 8 at.%, the thermal budget required to form $Ni(Ge_{0.42}Sn_{0.04})$ already leads to the activation of Sn diffusion and phase separation [100]. This significantly reduces the effectiveness of conventional annealing techniques like RTA for GeSn with 8 at.% Sn and above, which prompted the study reported in Chapter 4.

As a general conclusion, this literature review covered the origin of interest in GeSn, state-of-the-art of GeSn-based electrical contacts, and potential processing methods for obtaining ultra-low ρ_c on high Sn-content GeSn, by reviewing the published processing methods realized on pure Ge and low Sn-content GeSn. These contacts are necessary for the proper functionality and controlled thermal losses by Joule heating of future GeSn-based devices for MIR optoelectronic applications. Moreover, this review highlights the importance of developing processes, compatible with the thermal limitation of high Sn-content GeSn, to highly dope GeSn and functionalize GeSn contacts, thereby achieving ultra-low contact resistance values in these passive junctions. The following chapter provides a general description of the methods and techniques used in the experimental part of this work.

CHAPTER 3 EXPERIMENTAL METHODS AND TECHNIQUES

In this chapter, we review the growth of metastable GeSn alloys, microfabrication of GeSn-based devices, and characterization tools employed in this work. Additionally, we provide justifications on major choices realized for device fabrication and characterization.

3.1 Growth of metastable GeSn alloys

Samples listed in Chapters 4 and 5 were grown using a Chemical Vapor Deposition (CVD) system. It is an essential growth technique in the semiconductor manufacturing sector. It relies on the decomposition of gaseous precursor molecules containing the growth elements, upon reaching a hot substrate that is placed on top of a susceptor inside of the reactor chamber. These reactions cause the decomposition of these precursors, and adhesion of only the desired growth elements on top of the substrate's surface to create "adatoms". Subsequently, the adatoms minimize their energy by surface diffusion and lattice-site occupation, thereby ensuring the crystallinity of the grown thin films [101].

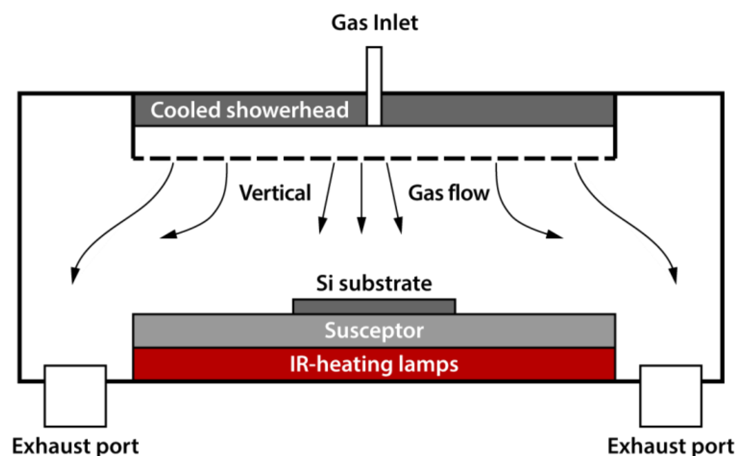

Figure 3.1 Schematic illustration of a CVD reactor chamber with vertical gas flow

This technique allows for the growth of multi-stacking layers with different chemical compositions [101]. Thus, the difference in lattice constant of two consecutive layers can cause two growth schemes. First, epitaxial or pseudomorphic growth is realized if the upper layer's in-plane lattice

constant matches that of the underlying layer [3]. This growth is possible via a tetragonal lattice distortion of the upper layer's crystalline structure, governed by the Poisson ratio [3]. In the second case, strain relaxation occurs via the formation of misfit dislocations and propagation of threading dislocations towards upper layers, whereby the distortions mentioned earlier become less significant [3, 102].

In this work, GeSn multi-stacks were grown on Ge-VS. The growth parameters were optimized to ensure a high degree of relaxation for GeSn layers, which offers multiple advantages as established earlier [2, 3]. The growth system is a vertical flow reduced-pressure CVD (RPCVD) with a configuration illustrated in Fig. 3.1. In this setup, the Si substrate is placed below the showerhead. Its "temperature *vs.* elapsed time" profile is controlled via an active thermocouple sensor, which monitors the intensity of IR heating lamps. The precursors are diluted and carried in H_2 gas at controlled flow rates using mass flow controllers. They are subsequently injected in the reactor chamber through a showerhead, and the residual chemicals are simultaneously pumped out of the system. The precursors used in our growth are monogermane (GeH_4) and tin-tetrachloride ($SnCl_4$), for Ge and Sn, respectively. Note that an H_2 bubbler is needed to achieve the desired gas flow from the liquid $SnCl_4$ precursor. As for *in situ* doping treated in Chapter 5, the dopant atoms are incorporated during the RPCVD growth, and their precursors are Arsine (AsH_3) for As doping, and Di-Borane (B_2H_6) for B doping. Further details on the growth process of Ge-VS and metastable GeSn are found in [33-35] and, [3, 30-32] respectively.

3.2 Microfabrication of GeSn-based devices

Microfabrication techniques are the backbone of building miniaturized devices. They are mainly based on replicating master patterns on the desired substrates via the addition or removal of matter. In this work, the lift-off approach was extensively used in Chapters 4 and 5 to build the necessary devices for electrical characterization. Although the detailed microfabrication process-flow varied depending on the devices' structure, the basic fabrication principles in the lift-off approach remain similar. A general illustration of these steps is shown in Fig. 3.2. Comprehensive details on other microfabrication methods are found in refs [101, 103].

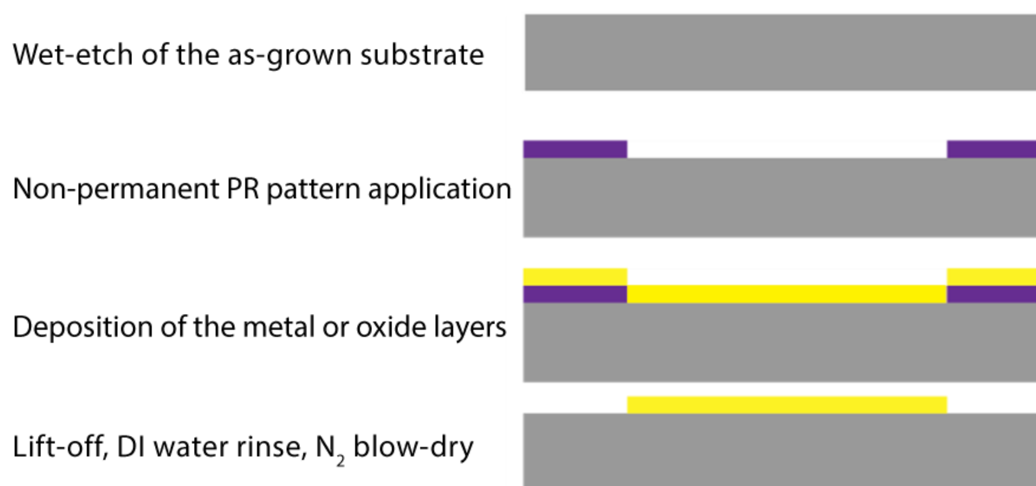

Figure 3.2 Illustration of the general steps used in the lift-off approach

The fabrication was carried out in its entirety in the LMF cleanroom facility. It starts with cleaning the as-grown samples from organic contaminants and dust particles using acetone for several minutes. This is followed by a wet-etch of the native oxides on the top using diluted HF or HCl. We note that concentrations of these solutions were carefully chosen to limit undesired effects, such as the significant regrowth of native oxides and the adhesion of carbon residuals. More details on the etching process followed in this work are found in [104, 105].

Next, a temporary pattern is applied on top of the sample using photolithography (PL). It starts with spin-coating and hard baking a photosensitive resist (PR). The positive (PR AZ5214) was used in our case, along with a neutral resist (LOR5A). The stack is exposed to UV light using the MA6 tool, which breaks the polymer chains of regions exposed through the mask. Afterward, the stack is submerged in a developing solution (AZ726MIF) to dissolve the exposed part and achieve a non-permanent pattern. Finally, choices of the PRs and their thickness were motivated by establishing a replicable recipe, which ensured a high resolution and flexibility towards multiple deposition methods and material thicknesses.

The subsequent step is the deposition of thin films. It is crucial to define functional and permanent patterns. This step was realized using two deposition systems. The first is the e-beam Thermionix tool, which allows for *in situ* deposition of both metals and oxides in the same run. The latter vastly

helped in the fast fabrication of B2B MOScap devices used in Chapter 5, by discarding a whole step from the fabrication process. The second system is the sputtering and e-beam deposition system. It features a load-lock for rapid venting to vacuum levels in the 10^{-8}-10^{-7} Torr range, and it is only dedicated to the deposition of pure metals, which ensured the high fabrication quality of M-S devices used in Chapters 4 and 5.

For the final fabrication step, the remaining PR is lifted-off in an organic solvent (REMOVER1165) to achieve a functional layer. After this step, some samples were immediately used to verify the desired thickness and uniformity, using reflectometry for oxide layers and profilometry for metallic ones. As a note, the fabrication of some devices requiring additional PL steps is done in the same manner, with special care in the exposition part to ensure the proper alignment of patterns constituting the devices.

3.3 Characterization methods

3.3.1 X-ray diffraction

X-ray diffraction (XRD) is a non-destructive method used in materials science to extract specimens' structural and chemical information. This method applies to a vast range of materials, starting from bulk and down to nanometric thin films [106]. It has been widely used to study epitaxially grown semiconductors, as it allows for the direct extraction of their macroscopic properties, including their chemical composition, strain, degree of crystallinity, and homogeneity [107]. Therefore, it was highly crucial for the characterization of pristine and processed samples used in this work. As illustrated in Fig. 3.3, this method relies on the diffraction of an incident X-ray beam, resulting from the cooperative elastic scattering of X-ray photons as they pass through an ordered material. The constructive interference of the scattered beam generates material-specific reflections, *i.e.* peaks, which can be correlated to the material's crystalline structure using Bragg's law [106].

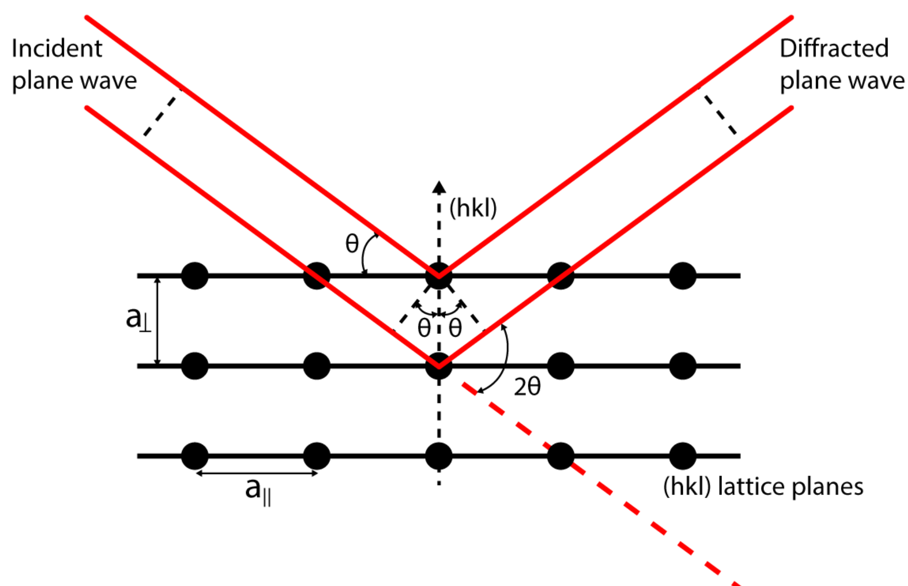

Figure 3.3 Illustration of the physical X-ray diffraction mechanism

The instrument used in this work is Bruker D8 Discovery. Here, the incident beam is generated with a Copper (Cu) source, and a monochromator is added to isolate the $CuK_{\alpha 1}$ = 1.5406 Å peak. A slit is then added if a smaller beam is needed. Measurements using this slit require a higher integration time for an acceptable S/N ratio. The tool was utilized in two modes. The first is standard symmetric (2θ-ω) scans in the (004) direction of Si, whereby 2θ is the angle between the incident (source) and diffracted (detector) beams, and ω is the angle between the incident beam and the sample's surface. For these scans, the sample and detector are carefully aligned to maintain symmetry between the incident and diffracted beams with respect to the sample throughout the entire 2θ scanning range. This mode allows for the symmetric crystal-diffracted peaks to be captured. It is used to gain quick information on the lattice parameter perpendicular to the surface, as indicated in Fig. 3.3. However, since the lattice parameters' values are influenced by both the strain and composition of the multi-stacking GeSn layers, obtaining the decoupled contributions of Sn-content and strain is not possible using this mode and would require higher-order scans.

For this purpose, XRD reciprocal space mapping (XRD-RSM) is employed. Here, the angle ω is incrementally readjusted around a starting value (ω_0) to obtain multiple scans throughout well-

defined (relative θ) and (relative ω) ranges. The resulting map is then reconstructed to obtain a representation of the reciprocal space, by converting θ to q_x and ω to q_z. The mapping is done around asymmetric peaks such as the (224) Si peak, which is the lowest index asymmetric peak contained in the Ewald sphere for cubic silicon. The map is then used to extract the strain and composition of the GeSn epilayers, using the method described in detail in [108]. In this regard, In our measurements, we used a bowing parameter value of 0.041 Å to account for the readjustment of Vegard's law, and the Poisson coefficient was also approximated based on multiple parameters that are all listed along with other minor details in [3].

3.3.2 Capacitance-Voltage measurements of Metal-Oxide-Semiconductor capacitors

Metal-Oxide-Semiconductor capacitors (MOScaps) are one of the most crucial parts of many electronic devices. In this work, Si-, Ge-, and GeSn-based MOScaps were fabricated. Capacitance-Voltage (CV) measurements of MOScaps were carried out to extract the underlying layers' active carrier concentrations. The complete theoretical background behind this technique is described in [109]. The general shape of an ideal p-MOS CV curve is presented in Fig 3.4 as a reference for comparison to the CV curves extracted from GeSn-based n-MOS and p-MOS devices, as discussed in Chapter 5.

For the experimental part of this work, two device layouts were fabricated, as illustrated in Fig. 3.5. Although conventional devices are more commonly found in literature, Back-to-Back (B2B) devices were also reported in multiple studies on GeSn [105, 110]. In this work, B2B devices were extensively used relative to the conventional ones. The reason is the 3x more work-intensive fabrication of conventional devices, which require 3 separate photolithography steps relative to a single step for B2B devices (Figs. 3.5c, 3.5d). Additionally, since B2B MOScaps do not contain a metal-semiconductor interface, establishing ohmic contacts is not an issue in their fabrication. The latter can introduce an additional Schottky capacitance effect on the CV curves.

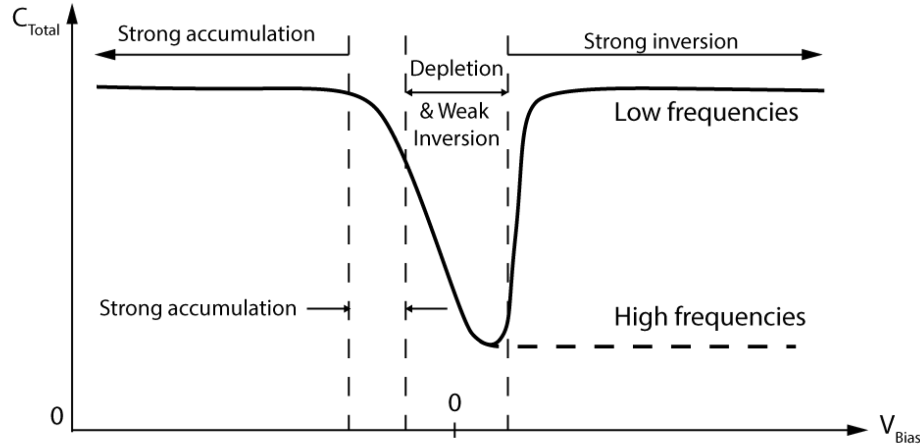

Figure 3.4 Schematic illustration of an ideal p-MOScap CV curve (adapted from [109] page 280). The solid line corresponds to low frequencies and the dashed line to high frequencies

For the optimization of these structures, the gate oxide used was e-beam deposited SiO_2, which has a relative permittivity of 3.9. For this reason, a thickness of 23 nm was chosen to achieve the highest capacitance, or in other terms, lowest equivalent oxide thickness without leading to large leakage currents or dielectric voltage breakdowns [111]. Indeed, the measured current for this thickness at a bias of 2V still is in the pA range. For the case of highly doped semiconductors with a doping level above 10^{19} cm^{-3}, the difference between the capacitance in strong inversion and strong accumulation regions becomes minimal. The latter reduces the precision of devices produced in using 23 nm thick SiO_2 gates, which implies the necessity to develop a low thermal budget solution to deposit high-*k* dielectric oxides with thicknesses below 10 nm, to precisely determine the doping level of high Sn-content GeSn at these high doping ranges [112].

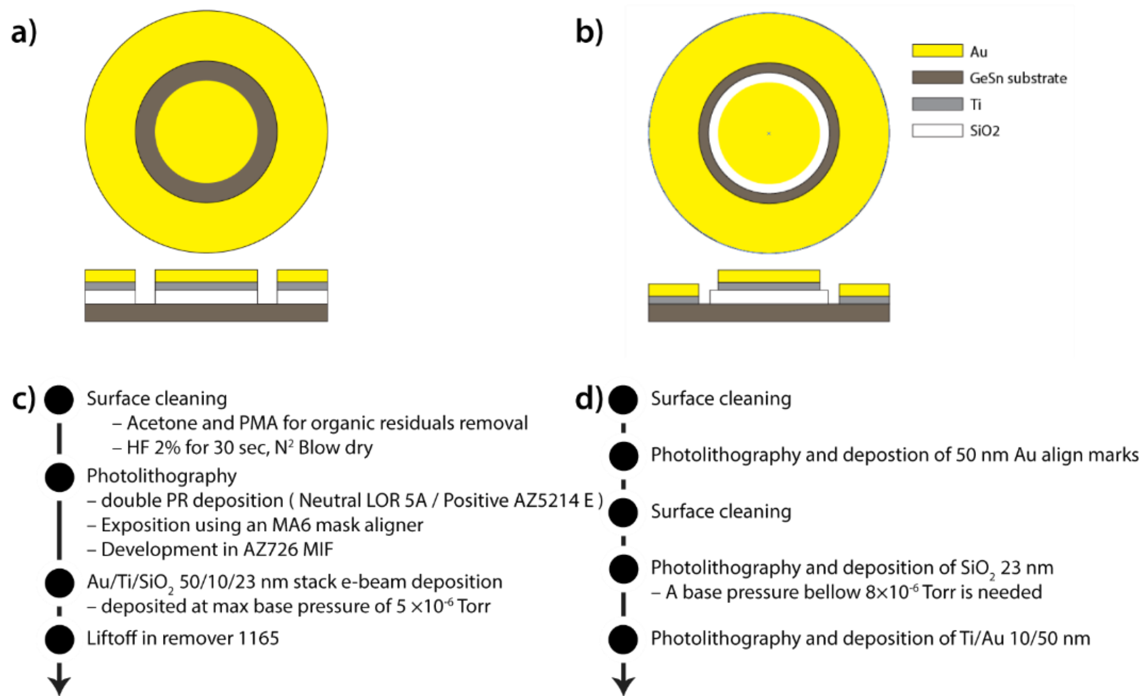

Figure 3.5 Illustration of the structure and process-flow for device fabrication of Back-to-Back MOScaps a) and c), and conventional MOScaps b) and d), respectively.

The electrical measurements were carried out in the Keithley 4200A-SCS parameter analyzer at room temperature. This tool's software environment allows for creating virtual MOS devices, and the extracted curves can be automatically analyzed. Before carrying out the carrier concentration analysis in GeSn, several steps were followed. First, the effect of the frequency on the CV curves was studied and optimized. It is done to ensure the use of high frequencies required for the proper strong inversion response, which is crucial for the accurate extraction of the doping level. Thus, the chosen frequency for reliable CV measurements of GeSn MOScaps is 1 MHz. During data acquisition, the voltage sweep is realized starting with the inversion region first. This was done to avoid the effect of the delay time during voltage incrementation on the carrier response, which can modify the CV slope of the inversion region [113]. Furthermore, given that all M-S contacts in the conventional MOScaps are front-side contacts, no compensation was done for the effect of the MOScap series resistance on the CV curves [113]. Finally, the extraction of the doping level from the CV curves was done using E.q. 3.1:

$$N_{sub} = \frac{2}{q\varepsilon_s A^2 \left(\frac{\Delta 1/c^2}{\Delta V_g}\right)}, \quad (3.1)$$

where ε_s is the relative permittivity of the semiconductor S, in $F.cm^{-1}$, A is the area of the gate, and $\left(\frac{\Delta 1/c^2}{\Delta V_g}\right)$ is the averaged slope of the linear part in the transition region of the CV curves [109]. The relative permittivity of GeSn (ε_{GeSn}) was assumed to be close to pure Ge ($\varepsilon_{Ge} = 16$), since the Sn composition range for samples used in this work is below 15 at.%.

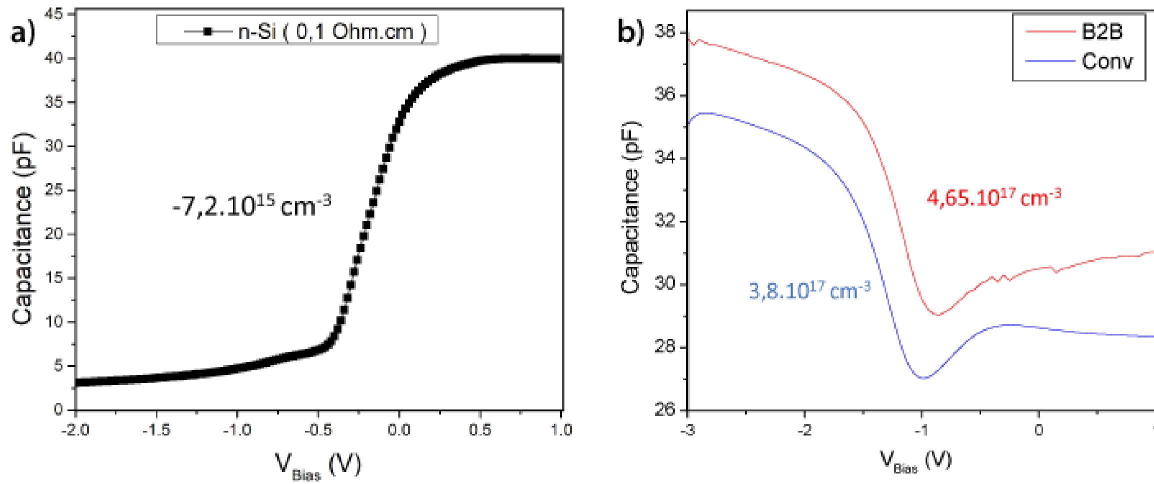

Figure 3.6 CV plots of a) Si reference sample with a resistivity of 0.1 Ω.cm, b) undoped $Ge_{0.92}Sn_{0.08}$-based B2B, and conventional MOScap devices

Moreover, a benchmark was done to assess conventional and B2B device structures' viability in obtaining reliable results. In addition, we note that all fabrication batches included a known reference, to ensure the microfabrication quality of the characterized devices. For instance, phosphorus doped n-Si samples with standard resistivities of 0.1 Ω.cm (Fig. 3.6a) and 0.005 Ω.cm were used. Their respective MOScap devices' extracted resistivities are 0.61 Ω.cm and 0.0054 Ω.cm, assuming a mobility value of 1400 cm^2/Vs for donor carriers in Si [114]. The extracted values are very close to the standard values. Hence, the experimental results can be considered

reliable if. Furthermore, the variation of doping level between conventional and back-to-back MOScaps falls within a factor of 5x in all devices, as plotted in Fig. 3.6b. This motivated the continuous use of the latter structures. Finally, it is worthy to note that our results on the background doping level of Ge-VS and GeSn agrees with the published values in the literature. Where the Ge-VS doping level is in the mid-10^{16} cm^{-3} doping range, and the GeSn doping level is in the mid-10^{17} cm^{-3} doping range [55, 110, 112, 115].

3.3.3 Current-Voltage measurements of M-S devices

Current-Voltage (IV) measurements of Ge- and GeSn-based M-S devices are an integral component in this work. They allowed for the extraction of the specific contact resistance ρ_c of the M-S interface and the sheet resistance Rs of the semiconductor. In this work, we fabricated Si-, Ge-, and GeSn-based devices dedicated to ρ_c measurement. Two design layouts were followed, the Transmission Line Model (TLM), [116] and Circular TLM (CTLM) [117]. Their accuracy in the extraction of ρ_c is shown in Fig. 3.7a. The used mask designs for these configurations are shown in Fig. 3.7b. These layouts were chosen because of their common usage at research and industrial scales as a result of their simplicity and flexibility.

All of the devices were microfabricated using the process-flow illustrated in Fig. 3.7c, and resulting CTLM structures are shown in Fig. 3.7d. The reason for choosing both layouts is to examine their accuracy and precision in extracting ρ_c values at multiple orders of magnitude in range, given that the latter was unknown in our material system. For the mask design, two device sets with different dimensions were implemented for both TLM and CTLM layouts to increase our measurements' accuracy. Moreover, the contacts' dimensions were chosen and optimized according to the notes in ref [118]. For the device structures, the metal stack was optimized to minimize its resistance, which can affect measurements' precision [118-120]. To be precise, and given the resistivity ρ values at 20 °C for Titanium (Ti), Gold (Au), and Ni of 4.20×10^{-7}, 2.44×10^{-8}, and 6.99×10^{-8} Ω.m, respectively. The minimization of the sheet resistance of Ni-based layers used in Chapter 4 consisted of choosing a high thickness of 30 nm. As for Chapter 5, Ti/Au stacks of 10/50 nm were chosen, instead of using a single and thick Ti layer, because Ti has a 17× higher resistivity than Au. Finally, the fabricated TLM devices included no lateral electrical isolation. Hence, their fabrication required a single photolithography step.

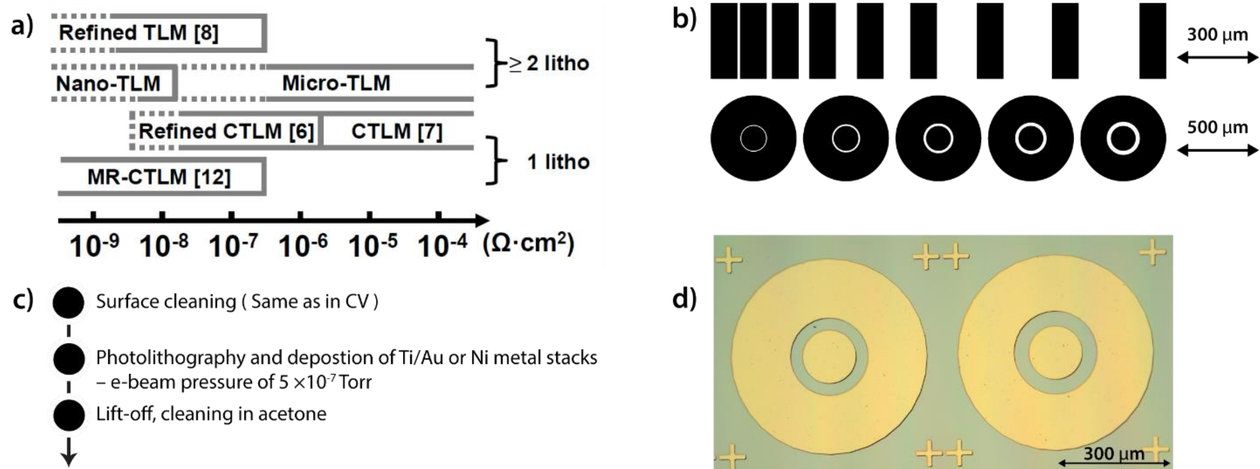

Figure 3.7 a) Accuracy range of different test structures in the extraction of ρ_c, dashed lines indicate regions where parasitic factors become dominant (© 2016 IEEE. Reprinted, with permission, from [121] Yu, H., et al., Process options to enable (sub-) 10^{-9} Ohm.cm^2 contact resistivity on Si devices, in 2016 IEEE International Interconnect Technology Conference / Advanced Metallization Conference (IITC/AMC). 2016. p. 66-68.), b) one set of CTLM and TLM test structures as-designed in the PL mask, c) process-flow for the fabrication of M-S devices, d) microscopic image of CTLM Ti/Au-on-Si devices.

Electrical measurements were carried out using the same system mentioned in Section 3.3.2. A two-point probe (2pp) setup was used, and measurements were acquired at room temperature. The total resistance R_T was extracted for each of the neighboring M-S contacts in the device set (Fig. 3.7b). Next, these values were plotted against the separation distance d_s. For TLM-based devices, the resulting plot is a linear curve with a positive y-intercept that can be fitted using Eq. 3.2.

$$R_T = 2R_c + \frac{R_s}{Z} d_s, \quad (3.2)$$

where R_c is the contact resistance, R_s is the semiconductor sheet resistance, and Z is the contact pads' height[116]. Next, ρ_c is extracted using Eq. 3.3.

$$\rho_c = R_c . L_T, \quad (3.3)$$

where L_T is the transfer length, which is half the x-intercept of the R_T $vs.$ d_s curve.

As for CTLM-based devices, a similar curve is obtained. However, the latter must be linearized using a conventional factor that evolves with d_s, [117] to extract ρ_c successfully. We also note that results are considered in this work only if the fitting process yields a high root square value, as the x-intercept is highly sensitive to the fitting quality and is a crucial component in the accurate estimation of ρ_c [117].

Before carrying out IV measurements on GeSn devices, a benchmark was done to examine the accuracy of TLM and CTLM structures, and their capacity in detecting low ρ_c values with precision. First, to assess their accuracy, 30 nm thick Ni contacts were deposited on RPCVD-grown p-type GeVS with background doping level in the 10^{16} cm^{-3} range. The average ρ_c values extracted from CTLM and TLM devices are 1.5×10^{-4} and 2.9×10^{-4} $\Omega.cm^2$, respectively. The latter is higher as a result of the unrestricted lateral current flow with the absence of a mesa-etch in our TLM devices. As for their capacity in detecting low ρ_c values, n-Si with a doping level in the 10^{19} cm^{-3} range was used to fabricate Ni silicide-based contacts via RTA, following the methodology described in [122]. The extracted ρ_c from these structures is 3.05×10^{-5} $\Omega.cm^2$, which is $10 \times$ higher than the published results [122]. The reason for this discrepancy is the dominance of parasitic series resistances in our setup over the contact resistance R_c, at this ρ_c range [121]. We identified two sources of parasitic resistances in our measurements. The first is the sheet resistance of the metal in the M-S contact. Solving this usually requires further processing to optimize the contacts depending on the metal and chosen layout [123]. The second is using a 2pp setup, which does not eliminate the probes' resistances, as compared with more specialized equipment such as Kelvin probes (4pp) [123]. Indeed, the smallest y-intercept value in the Ni/n-Si sample had an average of 12.3 Ω, whereas the measured probes resistances were in the 8-12 Ω range. Thus, the probes' resistances are the dominant source of parasitic resistance in our IV measurements.

Finally, it is worthy to note that the delicate task of precisely measuring ultra-low ρ_c values in future M-GeSn devices can be met by eliminating the device-related parasitic resistances. This can be done by implementing novel device layouts that offer high precision down to the low 10^{-10} $\Omega.cm^2$ range, as established in [124]. Also, the analysis of these devices must incorporate equations

that account for the non-uniformity in thickness of M-S contacts, which happens after alloying [125].

3.3.4 Transmission electron microscopy

Transmission Electron Microscopy (TEM) is considered an essential experimental tool in the materials science community, because of its higher spatial resolution compared with other techniques. This results from the highly-accelerated electrons with energies above 100 keV used in TEM, which decreases their wavelength significantly, thereby allowing sub-Ångstrom spatial resolutions [126].

For TEM samples' preparation, the samples need to be thinned down to create lamellas from the region of interest with thicknesses below 200 nm [126]. This process is usually achieved via focused ion beam (FIB) milling [126]. During characterization, the highly energetic e^- beam pass through this lamella, and their interaction with atoms allows for multiple imaging and diffraction modes to be obtained. Comprehensive details on all of the state-of-the-art techniques involved in TEM characterization are found in ref [126], whereas the following descriptions are restricted to techniques used in the scope of this work solely.

Cross-sectional TEM images shown in Chapters 4 and 5 were acquired along the [110] zone axis, either in the dark-field or bright-field modes. These are diffraction contrast modes obtained by capturing the main beam or one of the diffracted, *i.e.* Bragg-scattered, beam spots, for the bright- and dark-field modes, respectively. The latter is possible via an aperture located in the back focal plane of the objective lens [126]. The obtained images can be used to determine the epitaxial quality, reveal defects such as threading dislocations and Sn-segregation in GeSn, and assess the scale of these features [126]. HR imaging mode also falls in this category, it uses additional correction lenses to reach higher resolutions, and the obtained images can be used for quantitative analysis of the local lattice parameters.

The following techniques were used in Chapter 4 solely. The first is high-angle annular dark-field imaging (HAADF). It is a STEM technique that forms images based on incoherently scattered e^- instead of Bragg-scattered e^- discussed earlier. If the scanned area is uniform in thickness, the contrast in the obtained images using HAADF is heavily dependent on the atomic number Z, *i,e* a

compositional contrast. Here, atoms with a higher number Z allow for more e^- scattering, and thereby appear brighter in the image. Second, nano-beam diffraction was also used to obtain electron diffraction patterns from regions-of-interest down to a few nm in scale. In our case, the resulting patterns were used to verify the regions' crystallinity. Third, Energy Dispersive X-Ray Analysis (EDX) was employed to detect X-rays emitted from a specimen during bombardment with the highly energetic e^-. EDX is used in conjunction with TEM via a separate EDX detector to identify the chemical composition of a specimen. Results can be individual profiles or 2D maps that show the distribution of elements in the sample, with a spatial resolution below 10 nm and good composition resolution.

As for the equipment, the used FIB is a FEI Helios Nanolab 660 DualBeam, and the TEM is a Titan 80-300 LB. The latter is corrected for spherical aberrations via a CEOS hexapole to allow for HR-TEM imaging. Additionally, the tool was operated at an accelerating voltage of 300 keV.

3.3.5 Secondary ion mass spectrometry

Secondary ion mass spectrometry (SIMS) is a powerful ion-beam technique. It permits the accurate analysis of composition as a function of depth in the first few micrometers of the material [127, 128]. It is one of the most used techniques in the study of doped semiconductors, as it allows for the detection of most impurity elements in the periodic table, and with compositional resolution down to few part-per-billions ppb [127, 128]. For this reason, it was extensively used in Chapter 5 to reveal the doping profiles.

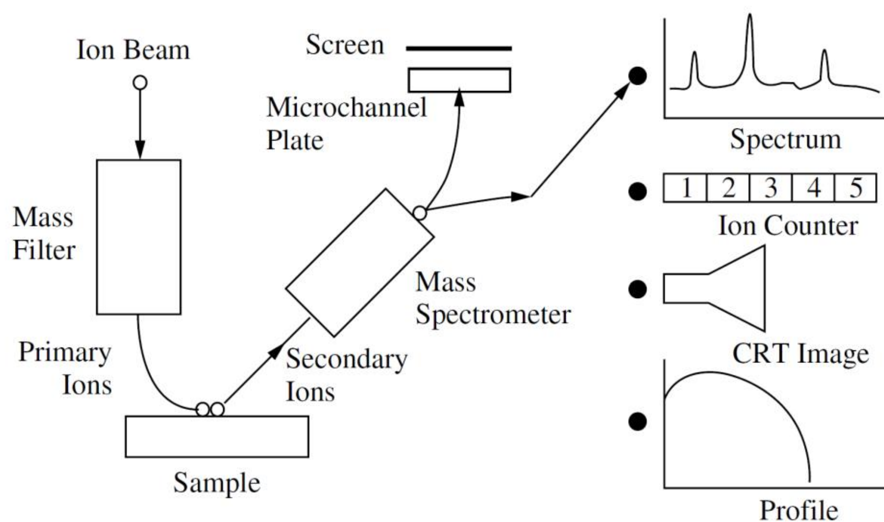

Figure 3.8 Schematic illustration of the SIMS components. Reprinted [17] Schroder, D.K., Semiconductor Material and Device Characterization, 654, 2005. With the permission of Wiley & Sons.

The technique is illustrated in Fig. 3.8. It relies on the bombardment of the sample's surface with a primary ion beam, which usually consists of O^{2+} or Cs^{+} ions accelerated at an energy below 20keV. This collision's impact allows for the ejection or sputtering of more than a single atom per single incident ion. The yield of ejected particles consists of more than 98% neutral atoms that are not detected. However, the 2% or less charged atoms are sufficient for an accurate compositional analysis of a specific element [127]. These charged ions are called secondary ions and can be positively or negatively charged depending on the targeted element. A high voltage is used to accelerate and collect them in the mass spectrometer [127].

In the Dynamic-SIMS configuration used in this work, the detector permits the continuous acquisition of datapoints in the mass spectrum during the surface bombardment. These mass spectra are then fitted for each element of interest to extract its "intensity *vs.* sputtering time" profile [127]. Generally, these profiles are converted to the depth instead of time, by assessing the final crater for its depth and calibrating it to the total sputtering time. This conversion necessarily includes the assumption of a constant sputtering rate throughout the analyzed depth, which is not always the case for heterostructures [127].

We note that optimizing the primary ion beam parameters, for each of the studied samples, is important to reach high mass resolutions and ionic yields in the acquired spectra. For highly resolved spectra, yield intensities can be calibrated to impurity concentration either by measuring well-known standard samples under the exact conditions, or by calibrating results to externally-obtained values on the samples's composition. Generally, despite this optimization, a signal spike is seen in the profiles' first few nms. This effect is encountered in most of the SIMS profiles. It arises from some artifacts that delay the attainment of a steady-state total yield of secondary ions to a certain depth, [129] which is apparent in the SIMS profiles shown in Chapter 5. In this work, samples were analyzed using a Cameca IMS-3f ion microprobe, employing a Cs^+ beam accelerated at an energy of 5 keV. Ion monitoring was done for various negative secondary ions of interest. The conversion of profiles to the depth was possible after assessing the final crater's depth, using an *in situ* Tencor P-17 surface profilometer.

3.3.6 Atomic force microscopy

Atomic Force Microscopy (AFM) is considered as one of the widely used tools for nanoscale surface topography related measurement in the scanning probe microscopy toolset. This results from the high resolution achieved in AFM, which is a fraction of nm in the depth scale, and a few nm in lateral dimensions [130, 131]. The use of this tool in both industrial and research purposes is not restricted to topographic mapping. Instead, multiple mapping modes are possible depending on the studied properties, such as its composition, mechanical, electrical, and magnetic contrast mapping. In this thesis, AFM was employed to reveal the topographic and compositional contrasts of the samples studied in Chapters 4 and 5.

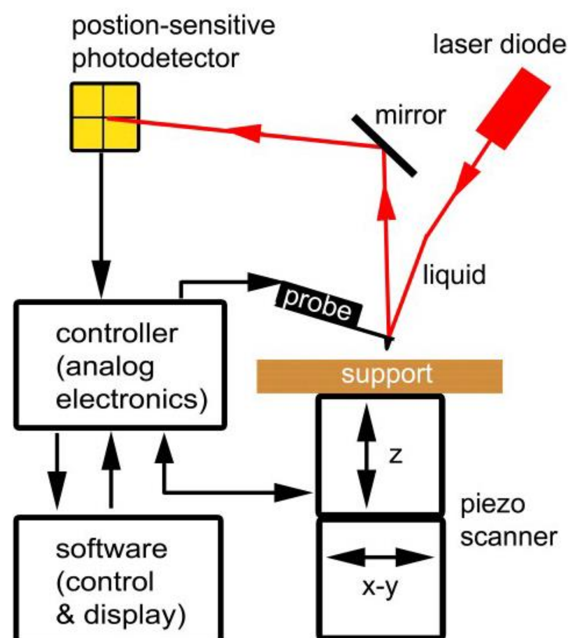

Figure 3.9 Illustration of the working principle of AFM. Reproduced from ref [130]. Zhong, J. and J. Yan, Seeing is believing: atomic force microscopy imaging for nanomaterial research. RSC Advances, 2016. 6(2): p. 1103-1121. With permission from The Royal Society of Chemistry.

As illustrated in Fig. 3.9, the main functionality of AFM comes from the interaction of a probe, a Si cantilever in general, with the sample's surface. The probe's accuracy in movement is ensured by piezoelectric motors [130]. During the acquisition of 2D topographic images, the laser is deflected through the cantilever. The surface's topography is simultaneously sensed by detecting the deflected laser's position on the photodetector array [130]. Height imaging in this thesis is performed using tapping-mode in AFM. For this mode, the cantilever oscillates close to its resonance frequency. As the tip approaches surface features, the oscillation amplitude is damped, which permits revealing the topographic features. Afterward, the root mean square (RMS) roughness can be calculated using the height curves. The latter is a figure-of-merit for surface roughness [130]. Moreover, phase images are also extracted in tapping mode. These are plots of the phase difference between the cantilever's oscillation and the piezoelectric driving signal [130]. The resulting phase contrast can be influenced by many interaction mechanisms, including composition, friction, and elasticity. However, if the analyzed surface is flat, the contrast in these

maps mainly results from compositional variations. As a note, using tapping mode preserves the cantilever from damage for maximum usage time compared with other modes. Finally, the AFM maps reported in this thesis were acquired using a Digital Instrument Dimension 3100 AFM model. Samples are generally blow-dried using nitrogen gas or cleaned with acetone before AFM mapping to eliminate dust particles on the surface. In the next chapter, we discuss the experimental results obtained on laser annealing of GeSn and Ni/GeSn heterostructures, as a processing tool to functionalize future high Sn-content GeSn-based devices.

CHAPTER 4 LASER THERMAL ANNEALING EFFECTS ON CONTACT RESISTANCE OF NI/GE1-XSNX AND STABILITY OF RELAXED GE1-XSNX SEMICONDUCTORS

4.1 Introduction

The growth temperature of GeSn with high Sn-contents is typically below 400 ºC to avoid Sn segregation and material degradation. However, this draws an upper limit in terms of the thermal budget needed in the subsequent steps for device processing and functionalization. This anticipated limited thermal budget must be considered in optimizing ohmic contacts, since these are essential for electronic and optoelectronic devices. These devices commonly require an extremely low specific contact resistivity ρ_c on both n-type and p-type doped junctions. Achieving such performance could be especially challenging for n-type GeSn due to the Fermi-Level-Pinning (FLP) near the valence band edge, similar to Ge [18]. To circumvent this issue, semi-metallic nickel alloyed contacts NiGe and $Ni(Ge_{1-x}Sn_x)$ were developed to act as an intermediary layer between the pure metal and Ge or GeSn contacted region, thereby reducing the FLP [67]. This process was explored earlier for GeSn at Sn-contents below 6 at.% using rapid thermal annealing (RTA) at temperatures below 400 ºC [50, 52]. However, the use of RTA cannot be effective as the Sn-content increases due to the associated reduced thermal stability, and the concomitant higher temperature needed for $Ni(Ge_{1-x}Sn_x)$ formation. For instance, it was found that the $Ni(Ge_{0.9}Sn_{0.1})$ forms at 80 °C higher than NiGe [99]. Moreover, RTA processing of GeSn with Sn-contents above 7-8% at 460 ºC leads to severe phase separation and the formation of holes on the surface [132].

Therefore, a different process is needed to meet thermal processing requirements for $Ge_{1-x}Sn_x$. In this regard, laser thermal annealing (LTA) appears to be a promising method. It provides total control of the treated surface's depth and temperature and allows for ultra-fast heat dissipation at the microsecond scale, thus only affecting the surface. As such, LTA is suitable for shallow and fast thermal surface treatments required to process stacked epilayers such as multi-quantum wells, without promoting dopant diffusion or compromising the sharpness of their buried interfaces [133, 134]. The underlying physics and the limitations of this approach are well-understood and controlled [133, 134]. Moreover, LTA has already been successfully implemented in surface-

related processes for a wide variety of material systems. For instance, improved electrical properties of hafnium oxide gate stacks were achieved using LTA [135]. In addition, LTA processing of metal-Ge contacts yields very high and shallow dopant activation well above 10^{20} cm^{-3}, exceeding their solid solubility limits in Ge [136, 137]. Moreover, these contacts can be further enhanced, by forming a continuous and atomically flat epitaxial nickel germanide layers ($NiGe_2$), which further reduces the FLP [138, 139]. Consequently, the combination of high dopant activation near the surface, and higher quality of the formed germanide, resulted in Ni/n-Ge contacts with ρ_c values 100x lower than that established by conventional RTA processing [140]. LTA is also well-suited to minimize the impact of thermal treatments on the structural properties of Ge and GeSn. This results from their high absorption coefficient at UV wavelengths and low melting temperatures [133]. Note that recent studies on LTA-processed pseudomorphic GeSn layer showed the potential of pursuing this method to functionalize GeSn-based devices, by proving the existence of a large thermal budget range in which these devices can be processed without compromising the thin films' quality [141].

In this chapter, we experimentally study the laser interaction mechanisms with undoped and relaxed Ge_xSn_{1-x} multilayer stacks, where x was varied between 4.6 at.% and 11.2 at.%. A broad range of annealing conditions was investigated and tailored to target multiple interaction modes. The resulting microstructure was comprehensively studied based on TEM analyses. Finally, we also addressed the effect of LTA processing on the resistance of Ni-based contacts on these GeSn samples.

4.2 Experimental details

The investigated GeSn layers were grown using a RPCVD system, following the experimental protocol described in Section 3.1. Ge-VS with a thickness of 1.6 µm is used as a substrate for the subsequent growth of GeSn multilayer heterostructures. The growth temperature of the top GeSn layers was in the 310-340 °C range. The Sn concentrations were extracted from XRD-RSM around the asymmetrical (224) peaks. Layer thicknesses were estimated from spectroscopic ellipsometry (SE) and TEM measurements. Our studies focused on three sets of GeSn samples at Sn-contents in the upmost layer of 4.6 at.%, 8.5 at.%, and 11.2 at.%. Table 1 summarizes the characteristics of the investigated layers. Note that each sample consists of several stacked GeSn layers.

Table 4.1 List of the reference Ge-VS and GeSn multilayer samples used in the study

	Thickness (nm)	**Sn-content (at. %)**	**Strain (%)**
Ge-VS	1674	0	0.16
$Ge_{0.954}Sn_{0.046}$	420	4.6	-0.54
$Ge_{0.915}Sn_{0.085}$	390/340/300	8.5/6.2/4.9	-0.42/-0.22/-0.18
$Ge_{0.888}Sn_{0.112}$	360/350/220/250	11.2/8.6/6.0/4.9	-0.33/-0.13/-0.11/-0.10

After the growth, the samples were cleaned in 1 % HF for 1 min, and then a 30 nm-thick Ni layer was deposited by electron beam deposition. Contacts were fabricated using optical lithography with a pattern designed for the Transfer Length Method (TLM). Two sets of rectangular structures with dimensions of 20×60 and 30×60 μm^2 were fabricated, with spatial separations varying from 4.6 to 21.6 μm.

LTA treatments were performed at the U.S. Army ARDEC Benet Laboratories. A frequency-tripled Nd:YAG laser (Ekspla) with a wavelength of 355 nm was used, with a fixed FWHM pulse duration of 6 ns. The laser beam was spatially homogenized and passed through a 3×3 mm^2 square aperture. Laser pulsing was repeated 20 times on the same area before moving to the next location in raster mode. This covered a 2×2 grid with a minimum overlap of less than 10 μm between the grid cells. The shot-to-shot variation was ensured to be low. Four different energy densities of 0.20 J/cm^2 (ED 1), 0.25 J/cm^2 (ED 2), 0.35 J/cm^2 (ED 3), and 0.45 J/cm^2 (ED 4) were selected for the LTA experiments to span the various laser-GeSn interaction modes, which will be discussed later on. All of the EDs were calibrated by melting bare Si and Ge. Time-resolved reflectivity with a 496 nm laser was used to monitor the melt duration, which was then compared to one-dimensional heat flow calculations that employed conventional thermophysical parameters for Si and Ge. The treated samples were cleaned for several minutes in acetone before carrying out any further experimental characterization.

4.3 Sn diffusion during LTA of relaxed GeSn semiconductors

To determine the effect of the LTA on the crystal quality and composition of GeSn, X-ray diffraction (XRD) measurements were performed. (2θ-ω) scans around the (004) diffraction order were acquired. For this, we used a circular slit with a diameter of 0.5 mm to restrict the beam to the area of interest between the contact pads. In the (004) XRD measurements for $Ge_{0.915}Sn_{0.085}$ (Fig. 4.1a) and $Ge_{0.888}Sn_{0.112}$ (Fig. 4.1b), the Ge-VS peak is visible at 66.06°, while the GeSn multilayers stacks are observed at lower angles. We first focus on the $Ge_{0.915}Sn_{0.085}$ sample, where a strong reduction in the intensity of the peak at 64.8 ° (TL 8.5 at.%) with increasing LTA dose is accompanied by a simultaneous increase in the intensity of the peak at 65.2 ° (#2 corresponding to a Sn-content of 6.2 at.%), while the peak at 65.4 ° (#1 - 6.2 at.%) remains unaffected. A similar trend is also observed in the $Ge_{0.888}Sn_{0.112}$ (Fig. 4.1b), where the intensity of the peak at 64.6 ° (TL 11.2 at.%) decreases, while a low-intensity additional signal develops at ~65.2 ° at the highest LTA exposure ED 4. The XRD signal shift to larger angles would indicate a reduction in Sn-content, strain relaxation, or both in the TL.

To decouple strain and composition effects, XRD-RSM maps were acquired around the asymmetrical (224) XRD peak. The measurements on as-grown $Ge_{0.888}Sn_{0.112}$ and after LTA at ED4 are shown in Fig. 4.1c and 4.1d, respectively. A small residual tensile strain $\varepsilon_{||}$~0.16 % is visible in the Ge-VS because of the difference in the thermal expansion coefficient between Ge and Si, leading to strain buildup during thermal cyclic annealing prior to GeSn growth. In the as-grown sample, the four highly relaxed GeSn layers with a composition of 4.9, 6.0, 8.6-9.4, 11.2 at.% are visible, with a compressive strain $\varepsilon_{||} \sim -0.3$ % in the TL. After ED4 annealing, the positions of all peaks remain unchanged. However, the TL intensity decreases, and a new slightly tensile-strained GeSn at ~9 at. % Sn peak develops (circle in Fig. 4.1d). The reduction in the TL intensity is in agreement with the (004) XRD scan (Fig. 4.1b) and indicates that a portion of this layer was partially depleted by Sn diffusion. However, no ~1 at.% Sn equilibrium phase is observed in the samples even after ED 4 treatment, indicating that GeSn still exhibits metastable compositions without signs of significant phase separation.

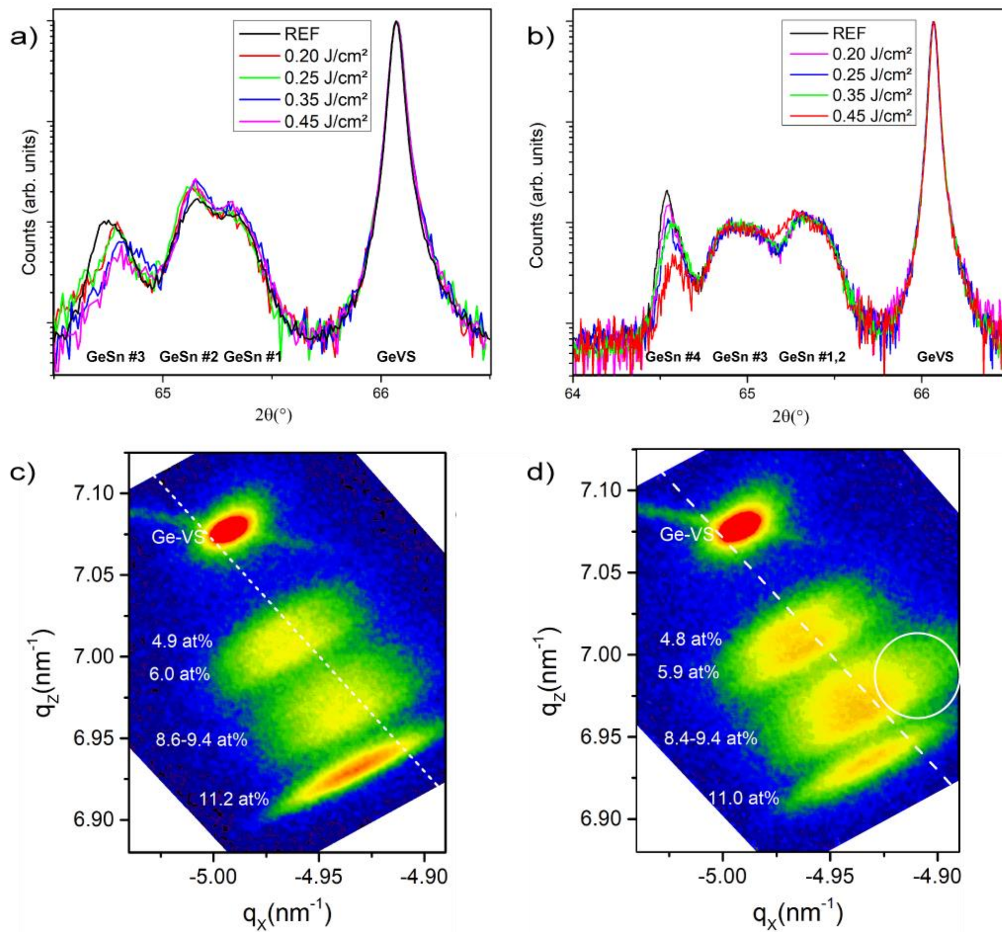

Figure 4.1 a) GeSn 8.5 at % Sn (2θ-ω) curves, b) GeSn 11.2 at % Sn (2θ-ω) curves, c) and d) XRD-RSM maps for the 11.2 at% Sn GeSn sample, for the reference and after ED4, respectively

The missing Sn atoms are expected to diffuse and accumulate at the surface of the sample. To investigate this behavior, atomic force microscopy (AFM) measurements were performed (Fig. 4.2). We first focus on the Ge-VS. In the 10×10 μm^2 AFM map for the Ge-VS (Fig. 4.2a), the <110>-oriented crosshatch pattern is visible, originating from the gliding of dislocations along the (111) planes during growth. A RMS roughness value of 0.9 nm is estimated. After treatments ED2 to ED4, the RMS surface roughness increases to ~1.2 nm, and the crosshatch pattern becomes hardly distinguishable. This behavior might be attributed to surface diffusion of Ge atoms induced by the LTA process. In the as-grown $Ge_{0.915}Sn_{0.085}$ (Fig. 4.2d), the crosshatch pattern is clearly visible with a higher RMS roughness of ~8 nm. Upon ED2 or ED4 annealing, the RMS roughness

increases to ~10 nm (Fig. 4.2e-f), and additional features with lateral dimensions well below 100 nm develop at the highest dose. Similar behavior was observed for the other samples with a higher Sn-content.

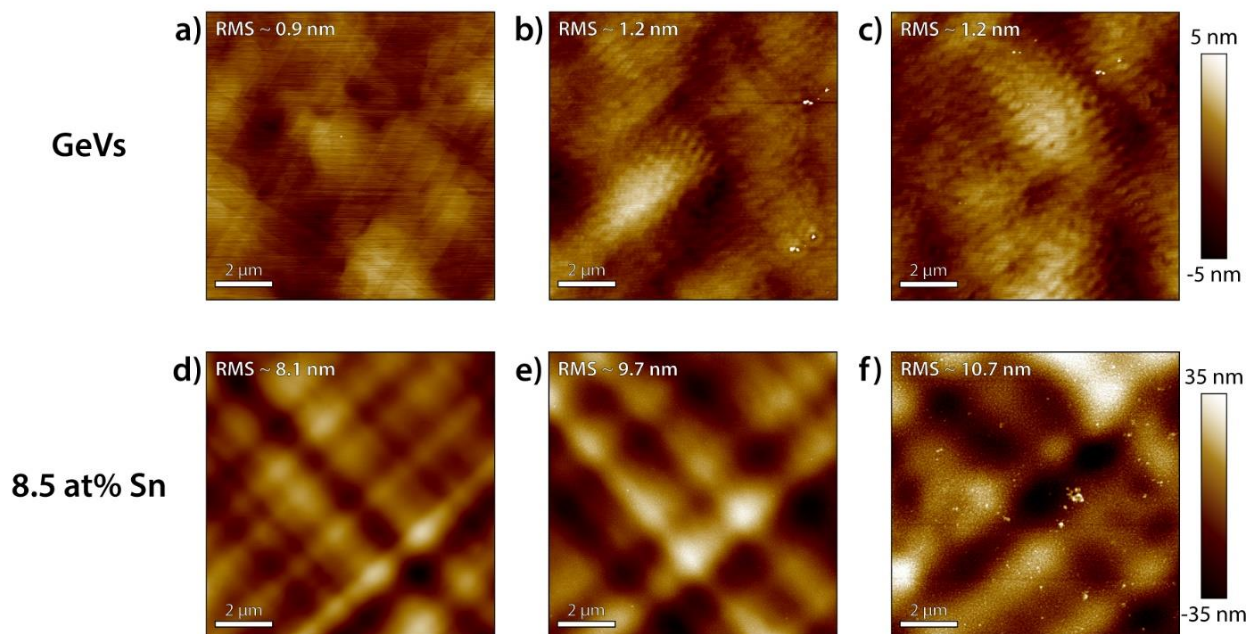

Figure 4.2 a) 10 × 10 µm AFM maps for: GeVS: a) as-grown, b) after ED2 and c) after ED4; and GeSn 8.5 at% Sn: d) as-grown, e) after ED2, and f) after ED4.

To further investigate this nanoscale roughening, 1×1 μm^2 AFM maps were acquired on the $Ge_{0.915}Sn_{0.085}$ sample, as shown in Fig. 4.3. While the as-grown sample has no observable features (Fig. 4.3a), after ED1 treatment, nanoislands with a diameter smaller than 50 nm and a height up to ~5 nm develop (Fig. 4.3b), and their density and size further increase at higher exposures ED2-ED4 (Fig. 4.3c-e). Similar behavior is observed in $Ge_{0.888}Sn_{0.112}$ sample, and the only difference lies in the slightly higher volume and density of these nanoislands for the latter (not shown), while in $Ge_{0.954}Sn_{0.046}$, the nanoislands are formed starting from ED2, and their density is lower than in the $Ge_{0.915}Sn_{0.085}$ sample (not shown).

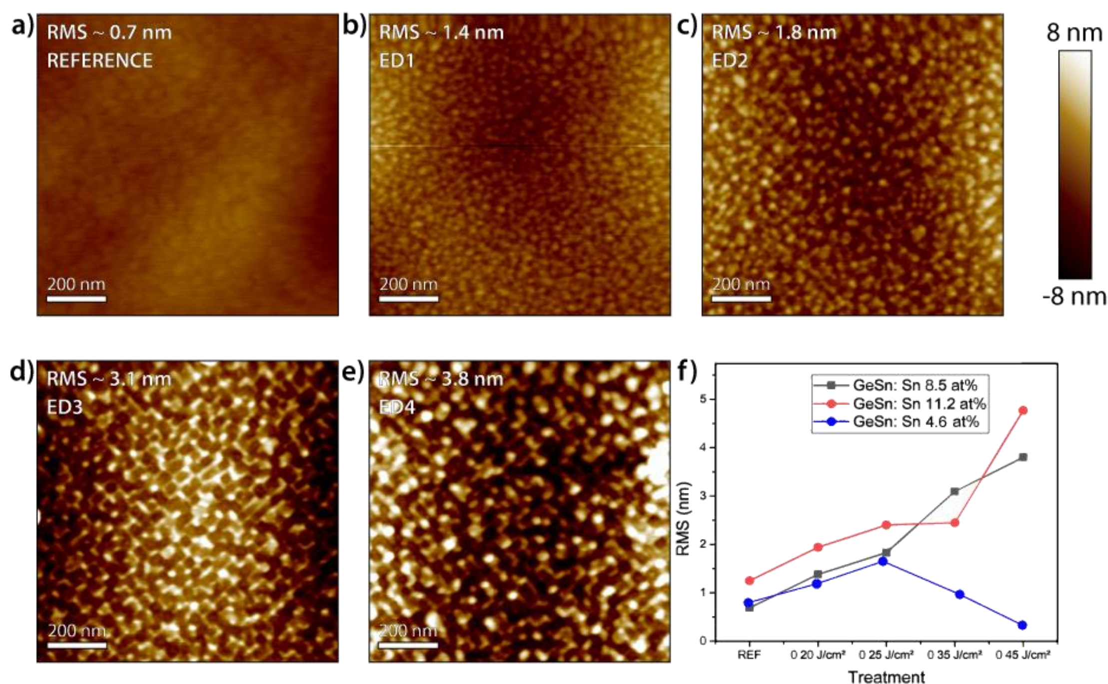

Figure 4.3 1 × 1 μm^2 AFM maps for GeSn at 8.5 at.% Sn: a) Reference. b-e) after ED1-ED4, f) RMS roughness values for GeSn samples obtained from 1 × 1 μm^2 AFM maps

The RMS roughness values were extracted from the AFM 1 × 1 μm^2 maps for GeSn samples, and results are plotted in Fig. 4.3f. Overall, the RMS roughness increases with increasing LTA power for the $Ge_{0.888}Sn_{0.112}$ and $Ge_{0.915}Sn_{0.085}$ samples. However, a higher horizontal onset is obtained for $Ge_{0.954}Sn_{0.046}$. These results effectively connect the higher surface roughening to the increasing Sn-contents at the surface for similar LTA power, and point to the strong influence of the thermal stability of GeSn on the redistribution of surface atoms, which is in good agreement with recent reports [141]. It is important to highlight the absence of macroscopic Sn droplets on the sample's surface after LTA [28]. This agrees well with the absence of a GeSn equilibrium phases that result from phase separation, as observed in the XRD-RSM maps (Fig. 4.1a). Instead, LTA processing yields small nanoislands with orders of magnitude lower diameter than the β-Sn droplets seen after RTA processing.

Next, a comprehensive TEM analysis of the 11.2 at.% GeSn sample after LTA at ED4 was realized. Results are shown and discussed in the following paragraphs. First, the effect of the LTA treatment ED4 on the microstructure of the entire GeSn stack was evaluated (not shown). The underlying layers, *i.e.* Ge-VS and GeSn #1-3 layers, are unaffected by the treatment. However, two regions with different morphologies are visible in the 360 nm-thick GeSn TL. While in the first ~160 nm a high crystallinity is preserved, a ~200 nm-thick highly defective region is visible in the uppermost portion of the stacking and results from the LTA process. Higher resolution images of this region are shown in Fig. 4.4. We note that these results support the XRD data in Fig. 4.1c, since the LTA-damaged region is contained in the TL, while the underlying layers stayed in their pristine condition after ED4.

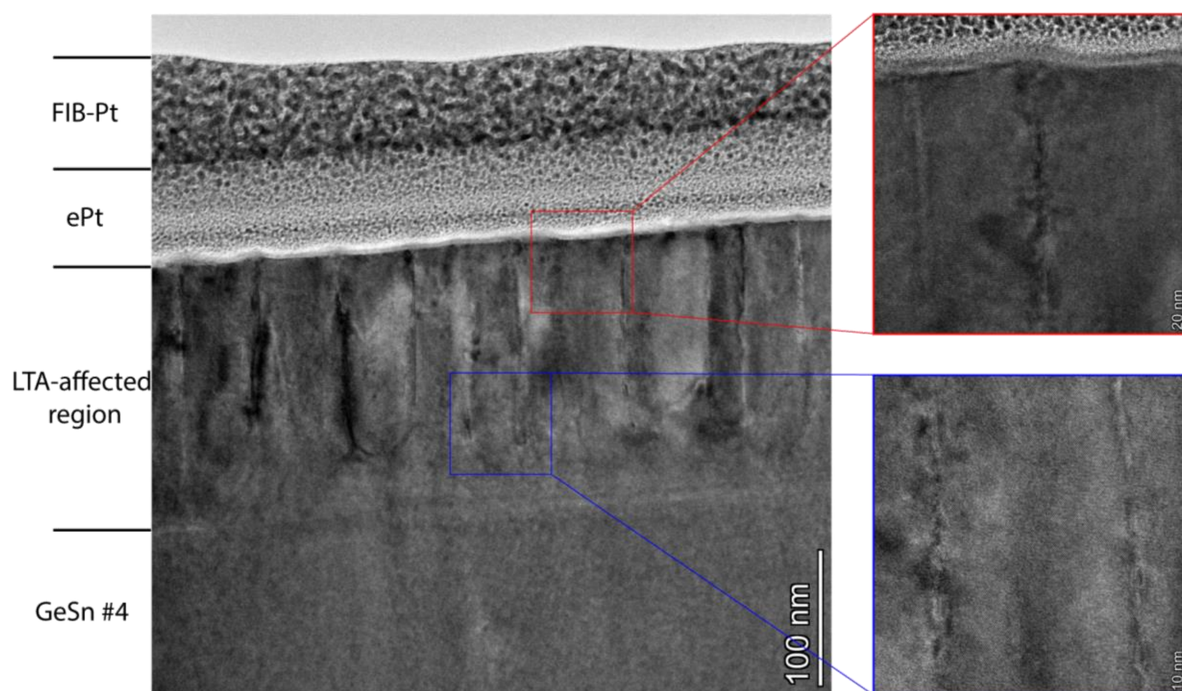

Figure 4.4 Higher-resolution Cross-sectional TEM images of the LTA-affected region, Insets are higher resolution images of the top and bottom parts of this region

The LTA-affected region in Fig. 4.4 can be restricted in thickness to the bright thin line, which is apparent in the main image at 200nm in depth, and the reason for that is discussed later on. More

importantly, this region is mainly characterized by the presence of linear features that resemble threading-like dislocations, and the inset figures (HR-STEM images) indicate the maintained degree of crystallinity in regions between these features. Moreover, these features appear at a depth of 150 nm, and they over-extend to the top layer where dome-shaped nanoislands are visible. These nanoislands are also apparent in the AFM images, as shown earlier.

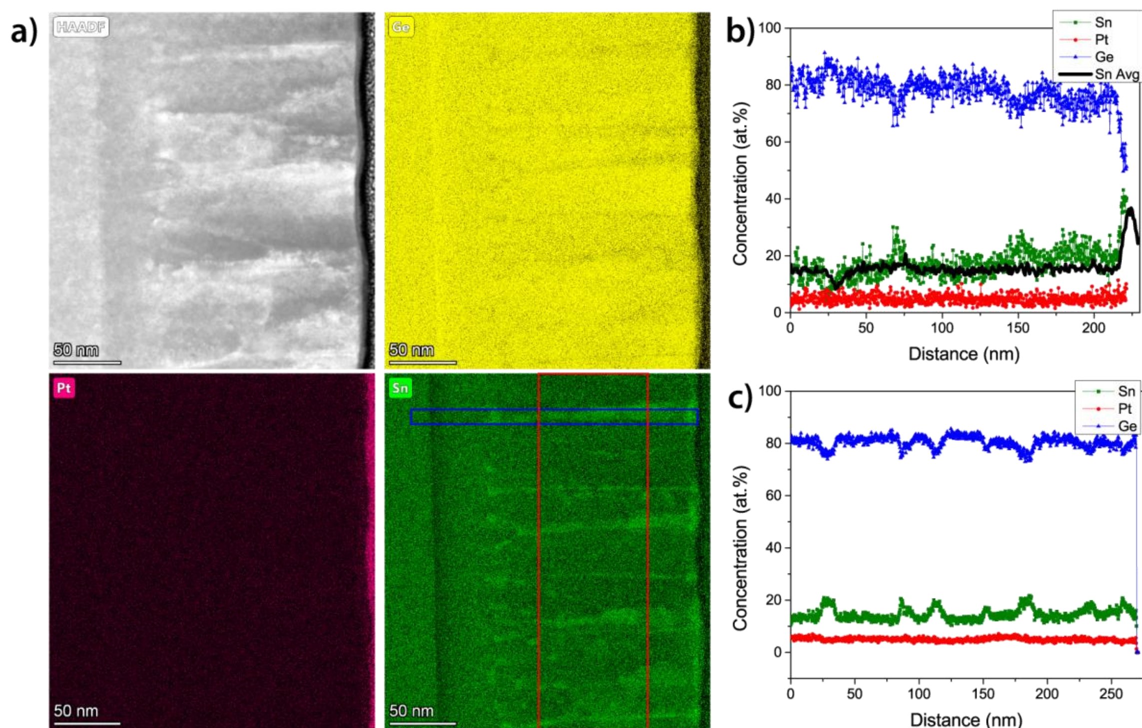

Figure 4.5 a) HAADF image and EDX maps of Ge, Sn, and Pt, of the LTA-affected region, b) lateral EDX compositional profiles (along the length of the blue line in the EDX maps), the solid black line is a profile average along the entire length of the LTA-affected region, c) longitudinal EDX compositional profiles (along the length of the red line in the EDX maps).

To investigate the Sn diffusion in $Ge_{0.888}Sn_{0.112}$ layer during LTA at ED4, we acquired STEM images and EDX maps displayed in Fig. 4.5a. As discussed in Section 3.3.4, the HAADF technique provides compositional contrast images, where brighter regions are richer in elements with higher atomic number Z. Thus, local enrichment of Sn is visible along the linear features, with an average Sn-content of 20-22 at.% that is much higher than in the nearby crystalline regions with 13-14 at.%

(Figs. 4.5b-c). Note that a Sn-content of 11.2 at.% was estimated for the TL in the as-grown sample, hence lower than what was observed in the crystalline regions after LTA. In addition, the RSM map of this sample indicates that part of the TL reduces in Sn-content down to ~9 at.% after ED4. Consequently, the real Sn-content values are shifted down with a 4-5 at.% range from those obtained through EDX profiling, and this more likely results from the presence of a Pt signal. However, the variation in the Sn EDX profile is still valid. The Sn-content further increases to ~30 at.% when the enriched lines reach the surface. Interestingly, at large depths in the TL, the local Sn-rich lines vanish, and depletion of Sn is observed down to ~10 at.%, followed by a steep increase back to the 14 at.%, as observed in the EDX profile. This behavior is also apparent across the entire lateral dimension of the Sn EDX map, where a (darker) Sn-poor line is visible at a depth of 200 nm. The line can be considered the largest depth affected by the laser during LTA, because deeper Sn atoms would have diffused to this region if they had enough thermal energy, since solute atoms (Sn) are attracted towards regions with higher temperatures considering the thermal gradient [142]. In addition, in the left inset of Fig 4.7, the Sn-depleted line perfectly follows the LTA-affected region's thickness variation at the Ni contact edge, which serves as additional proof for this behavior.

Moreover, to explain the possible underlying mechanisms for Sn diffusion during LTA, it is first important to highlight the effect of varying the laser parameters on the annealing process. As the laser ED increases, the slope of the created thermal gradient *vs.* depth is maintained, however, its y-offset increases, and the surface's temperature can exceed the melting point of the processed material [143]. For bulk Ge, LTA at a value identical to ED4 yielded a large thermal gradient of ~300 °C/µm, and resulted in melting ~50 nm of the top layer [143]. However, the thermophysical properties of GeSn have not yet been investigated, which makes it harder to predict the material's response, [144] and the melt-depth of GeSn can vary from that of pure Ge for increasing Sn content [145, 146]. Thus, interpretations that include melting and solidification are not thoroughly considered here. More importantly, we note that during LTA, the temperature *vs.* elapsed-time curves consist of a very steep temperature ramp-up, which is directly controlled by the laser pulse duration and is usually restricted in the ns scale. On the other hand, the quench rate is governed solely by the annealed layer's thermophysical properties and takes 100 s of ns longer to stabilize

at the substrate's temperature. Thus, both time regimes can influence Sn redistribution in GeSn during LTA.

In the following paragraphs, we list and explain the possible mechanisms responsible for forming the structures shown in Fig. 4.5. First, we start with those that do not necessarily involve melting and recrystallization of $Ge_{0.888}Sn_{0.112}$ during LTA at ED4. As established earlier, Sn atoms diffuse towards regions with higher temperatures along the thermal gradient, *i.e.* towards the surface [142]. Furthermore, based on the mathematical models detailed in, [142] increasing the ED increases the gradient's average temperature, resulting in a higher redistribution of Sn atoms. This effect was also witnessed in LTA-treated GeSn at very high Eds that caused the total melting of the treated layer, where a thin 4 at.% GeSn sample was processed to achieve a graded GeSn layer with Sn-content up to 14 at.% near the surface [147]. As for the second mechanism, the LTA-affected region expands in volume during the treatment, and the quenching process can introduce new defects in the region, especially since this process is repeated 20 times. For instance, new dislocations that were not present in the as-grown layer can form as a result of the lattice expansion and shrinkage during these treatments. These dislocations can assist in Sn diffusion, given that the diffusion coefficient in their core is orders of magnitude higher than that for bulk diffusion, and can reach up to a factor of 10^4 [28].

Following these mechanisms, the Sn-rich lines in Fig. 4.5 likely originate from the small Sn-rich GeSn spherical features that appear 40-50 nm above the Sn-depleted region (Sn EDX map in Fig. 4.5a). Moreover, this depth range persists in the LTA-affected region of Ni/GeSn structures, despite its 35% higher thickness than in pristine GeSn, as will be discussed later on. Thus, these spherical features' origin at this depth range likely results from the processing conditions, which favor their nucleation at this depth range, and not initial defects present in GeSn. Their origin could be the result of combining the high local strain induced by the Sn-depleted region and threading-like dislocations formed during the LTA process. Another explanation that does not necessarily involve melting is the energy favourability for initial GeSn phase separation at this depth, such as by the spinodal decomposition of GeSn during the cooling process [148].

When the Sn-rich spherical features form, they can serve as nucleation sites for Sn to diffusion along the dislocations' cores. However, most of these lines increase in their thickness (Sn EDX map at Fig. 4.5a) and their composition (Sn profile in Fig. 4.5b) towards the surface. Although

these features are different from those attributed to Sn-pipe diffusion lines observed in the as-grown samples, [28] the combined effect of Sn diffusion along the thermal gradient and inside the dislocations' cores could be the reason for this variation. In addition, since shallower regions cool less rapidly during the LTA process, a high Sn concentration is expected in the Sn-rich lines near the surface. The latter can also be considered as the origin for the presence of dome-shaped surface features with a Sn-content of ~30 at.%, especially since these features overextend directly from the Sn rich pillars. Furthermore, the Sn-content, as-revealed in the average Sn profile (black line in Fig. 4.5b), is 1-2 at.% higher below the Sn-rich lines at a depth of 150-200 nm, and is flat until the signal spike at the surface. Hence, Sn accumulation at the surface results from Sn diffusion at a depth range of 0-150 nm.

The following possible mechanisms include the melting and rapid solidification of the LTA-affected region. During solidification, the underlying solid GeSn acts as a seed for the bottom-up liquid phase epitaxial regrowth of molten GeSn [146, 147]. The recrystallization velocity of GeSn is characterized directly by the solid/liquid interface velocity (v), which is proportional to the temperature gradient. For melts achieved with a Nd:YAG laser, the interface velocity is around 6–10 m/s. These high values are caused by the steep thermal gradient in LTA [145, 149]. Here, v exceeds the diffusive speed of Sn in Ge (v_D), which can reach up to v_D ~ 5 m/s [150] close to that of Sn in Si [151]. Such conditions allow both Sn and Ge atoms in the liquid to be incorporated in the solid with no energetic favorability, and the supersaturated liquid crystallizes while having a Sn composition that can deviate from the local equilibrium value (1.8 at%) [152]. Moreover, this 10x higher Sn content than the equilibrium value is likely to cause cellular breakdown in the solidification front during laser annealing, which could also explain the formation of these Sn-rich features during LTA [153, 154]. This mechanism is caused by the perturbation of the melt front, and lateral movement of Sn atoms, which create Sn-rich regions that are subsequently locked in composition during solidification. The resulting mosaic pattern's periodicity (Figs. 4.3d-e) can be correlated to the diffusion parameters of Sn in Ge during LTA [154].

In our case, it could be possible that Sn atoms diffuse from a depth range of 200-150 nm as a result of the thermal gradient effect, which creates Sn-depleted lines at 200nm and local Sn enrichment at depths above (200-150 nm). The later can further destabilize the solidification front at 150nm in depth, thereby allowing for the creation and propagation of Sn-rich regions towards the surface.

Moreover, the melting point of Sn is 232 °C, substantially lower than that of Ge 938 °C [155, 156]. Hence, the melting temperature of supersaturated GeSn is expected to be lower for regions with higher Sn concentrations. Consequently, the Sn-rich lines' melting temperature is expected to be lower than that of the neighboring regions. Thus, Sn atoms in these regions have a longer time to diffuse towards the surface and form Sn-rich dome-shaped features. This mechanism would explain the entirety of the features observed in the LTA-affected regions, and the shape of the average Sn profile (black line in Fig. 4.5b) as well. Finally, we note that these features were also observed in Sn-implanted Ge that was subsequently annealed above ED4. The result of LTA processing the layer is a fully-relaxed 6at.% Sn GeSn layer [157]. However, the features were not apparent in any of the studies conducted on pseudomorphic GeSn that was LTA-treated at similar conditions [141, 145, 146]. This is particularly interesting as it suggests that the solidification front's destabilization, and the lateral movement of Sn during solidification, are affected by the strain of the LTA-treated layers.

4.4 Laser annealing of Ni contacts on GeSn

To determine the effect of the LTA parameters on the electrical performance of Ni-based contacts on GeSn, we extracted ρc values from electrical measurements of the fabricated TLM devices. In addition, a comprehensive TEM analysis was carried out for Ni-based contacts on $Ge_{0.888}Sn_{0.112}$ that was LTA-treated at ED4. In the following, we start with results on the electrical measurements. First, it is crucial to note that the samples are undoped. However, background p-type doping levels of 1-5x10^{16} cm^{-3} for Ge-VS to 1-5x10^{17} cm^{-3} for GeSn were measured. The source of this unintentional p-type background doping is the vacancy defects present in the lattice, as discussed in Chapter 3.3 [158, 159]. For the electrical measurements, the specific contact resistance ρ_c was extracted from the reference and LTA-treated TLM-patterned contacts. The reported values are an average of at least three device sets for each rectangle dimension.

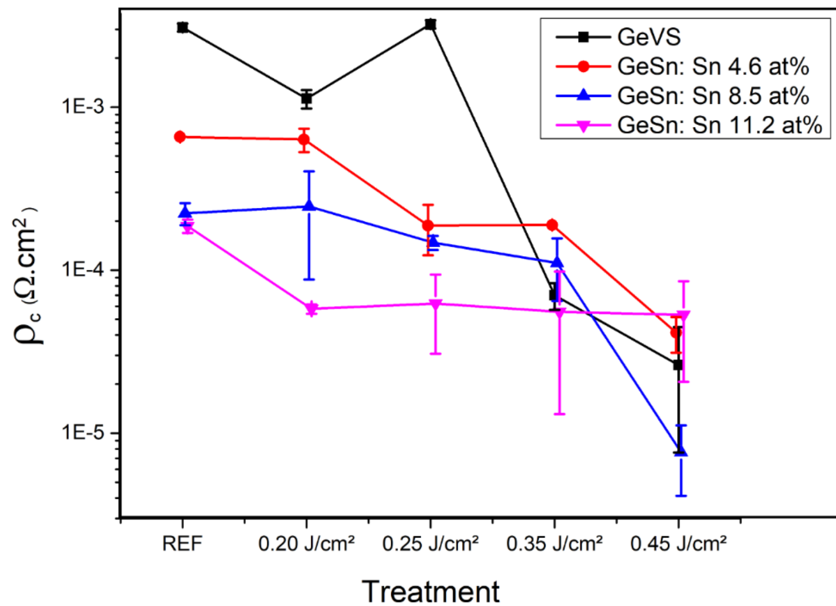

Figure 4.6 Evolution of the specific contact resistance ρ_c as a function of the laser ED

The specific contact resistance as a function of the ED1 to ED4 LTA treatments is plotted in Fig. 4.6. A decrease in contact resistance with increasing LTA is observed in all samples, however different regimes are visible. The Ge-VS shows the largest reduction in ρ_c. While the contact resistance remains constant in the 1-3x10^{-3} Ω cm^2 range in the as-grown and ED 1-2 samples, a steep decrease to 7±1x10^{-5} Ω cm^2 (ED 3) and 3±2x10^{-5} Ω cm^2(ED 4) is observed at higher LTA exposures. The sudden drop in resistivity is most likely related to the formation of NiGe or $NiGe_2$, which were reported in Ge when RTA-processed at 400 °C [73] or with LTA at an ED>0.3 J/cm² [138, 143]. A similar monotonic decrease in ρ_c is visible for both $Ge_{0.954}Sn_{0.046}$ and $Ge_{0.915}Sn_{0.085}$ samples, with values ranging from 7±0.04x10^{-4} Ω cm^2 (as-grown $Ge_{0.954}Sn_{0.046}$) to 4±1x10^{-5} Ω cm^2 (ED 4) and 2±0.3x10^{-4} Ω cm^2 (as-grown $Ge_{0.915}Sn_{0.085}$) to 8±4x10^{-6} Ω cm^2 (ED 4), respectively. As for the $Ge_{0.888}Sn_{0.112}$ sample, ρ_c initially decreases from the as-grown value of 2±0.2x10^{-4} Ω cm^2, to 6±0.4x10^{-5} Ω cm^2 for the ED1-treated sample. Whereas increasing the intensity in the ED2 to ED4 range yields similar values in the 5±5x10^{-5} Ω cm^2 range.

Additionally, it must be noted that in the presence of a thermal gradient, vacancies can only move along the thermal gradient towards regions with lower temperatures, *i.e.* away from the Ni/GeVS

or Ni/GeSn interfaces. Thus, the surface can only have an equal or lower background doping than the bulk after LTA [142]. As a result, the improvement of the electrical properties can only be attributed to the creation of a Ni germanide or stanogermanide. Regardless of the exact stoichiometry of the present Ni-based phases, they mainly form because of the fast diffusion of Ni on Ge/GeSn [143]. This mechanism can be impeded if a high Sn concentration is present on the surface [160]. Hence, this could be the reason why ρ_c stays constant for treatments with increasing EDs in the 11.2 at% Sn sample.

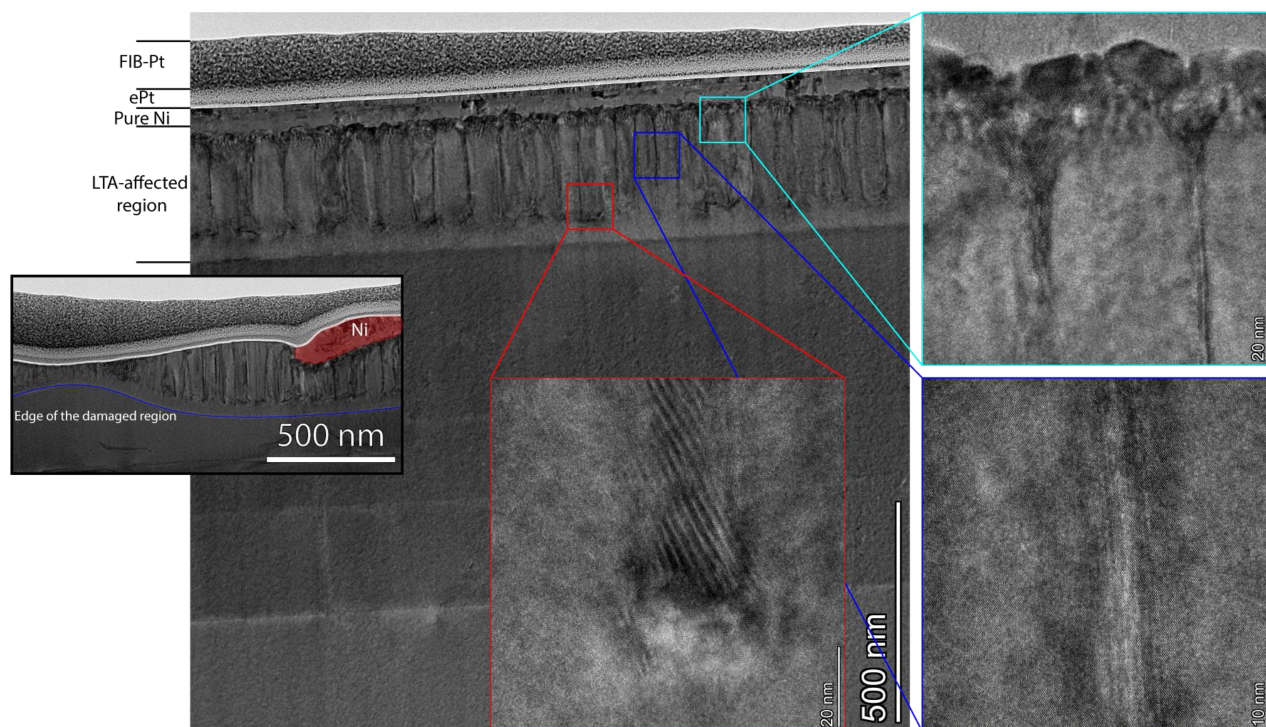

Figure 4.7 Cross-sectional TEM image of the contact Ni/GeSn with 11.2 at.% Sn, after LTA treatment at ED4. The inset on the left-side is a cross-sectional image of the contact edge. Other insets correspond to the HR-STEM images of the regions in small squares.

To further investigate these contacts' structural properties, Ni/$Ge_{0.888}Sn_{0.112}$ contact formation using LTA at ED4 was extensively studied with TEM analyses. Images of the area under the contact are shown in Fig. 4.7. First, we note that the LTA-affected region under the contact is 35% higher in thickness than that in pristine GeSn (Fig. 4.4). Moreover, the LTA-affected region's thickness

varies significantly near the contact edge in the left inset of Fig. 4.7. The latter highlights the importance of optimizing the Ni layer thickness to avoid additional reflection, which can unnecessarily further damage the material [143]. Moreover, HRSTEM images of structures around the Sn-rich lines are shown on the right side of Fig. 4.7. These images highlight the lines' different features compared to those obtained on LTA-annealed pristine GeSn, which likely resulted from the Ni's presence in these lines as well.

Moreover, HAADF imaging and EDX maps of the Ni, Sn, and Ge were acquired. Results are shown in Fig 4.8. First, the results presented in Fig. 4.8a-b serve as proof for the formation of a Ni-based alloy with GeSn, since a 60 nm Ni-rich GeSn region on the top of the surface is clearly observed in the EDX profile. Surprisingly, Ni was also found inside some Sn-rich lines, and even Sn-rich spherical features 250 nm below the surface (Ni EDX map in Fig. 4.8a). For the former-mentioned 60 nm thick Ni-rich GeSn, the HAADF image reveals that it consists of two regions, which need to be examined separately. We start with the continuous layer, marked by the green rectangle in the Ni EDX map in Fig 4.8a. Its corresponding EDX profile is shown in Fig 4.8c. The profiles show constant Ni, Ge, and Sn concentrations throughout the entire scanning distance. Moreover, the layer is crystalline and continuous based on the HR-STEM images (not shown here). Thus, it is most likely composed of a $Ni(Ge_{0.88}Sn_{0.12})_2$ phase, which is consistent with what was observed for Ni on pure Ge annealed at ED4, as discussed in [143]. We note that the formation of this phase, during LTA processing of Ni-based Ge contacts, allowed for the reduction of ρ_c by a factor of 100x compared with NiGe formed using RTA [143].

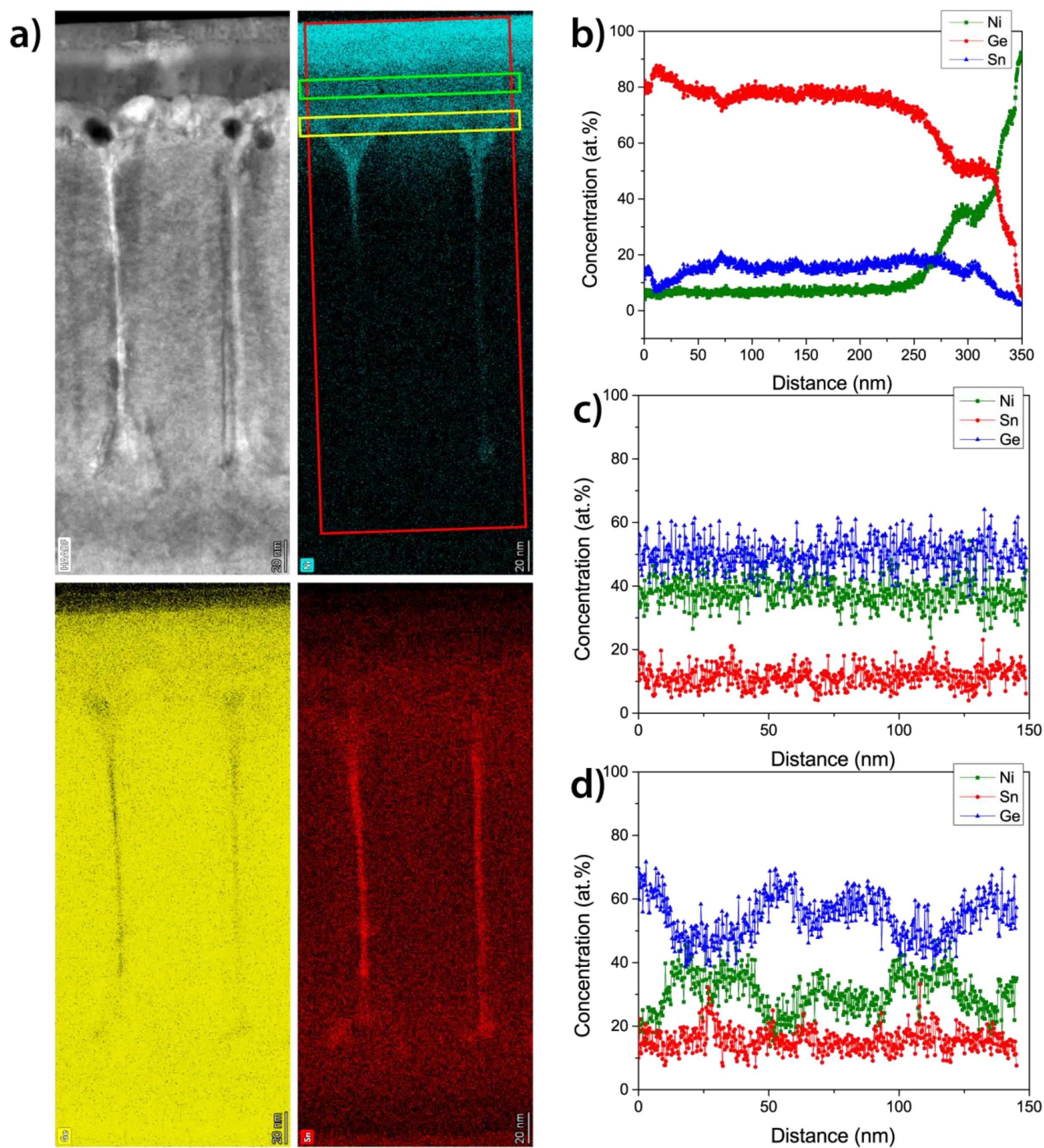

Figure 4.8 a) HAADF image and EDX maps of Ge, Sn, and Ni, of the LTA-affected region, b) EDX compositional depth profile, along the length of the red line in the EDX maps, c-d) longitudinal EDX compositional profiles, along the length of the green and yellow lines in the EDX maps, respectively.

Secondly, for the region marked by the yellow rectangle (Fig 4.8a), the formed structures are Ni- and Sn-rich, as seen in the EDX profiles in Fig. 4.8d). The funnel-like shape between the Ni layer and the Sn-rich lines is similar to that for hafnium pipe-diffusion in nitride superlattices reported in [161]. Moreover, Ni diffused along these lines and was also found in Sn-rich spherical features buried 250 nm deep. To explain this behavior, we begin by highlighting a few notes. First, it was found through a comprehensive analysis of the solid-state diffusion of Ni, and formation of Ni-based alloys with GeSn, that for GeSn samples with higher Sn concentrations, a higher temperature is required to form an alloy between Ni and GeSn [99]. Secondly, the solubility limit for Ni in liquid Ge is orders of magnitude higher than that for Ni in solid Ge [143, 162]. This allows for Ni to dissolve much more rapidly in the former. By considering both points, it is possible that Ni also diffuses in threading-like dislocations' cores at a higher rate than in the bulk of GeSn, similar to Sn-pipe diffusion, thereby leading to a faster Ni diffusion along these lines relative to the nearby structures. Another possibility is that the Sn-rich lines were in the liquid state during the fast diffusion of Ni towards the depth, which would support arguments on the cellular breakdown of GeSn. Finally, the cause of the poor electrical performance of LTA-processed Ni-based contacts on the $Ge_{0.88}Sn_{0.12}$ sample relative to samples with lower Sn-content, is the presence of these Sn-rich nanoislands at the interface between the $Ni(Ge_{0.88}Sn_{0.12})_2$ phase and the $Ge_{0.88}Sn_{0.12}$ layer below. These nanoislands were indeed higher in volume and density in the $Ge_{0.88}Sn_{0.12}$ sample, as discussed earlier in Section 4.3. Hence, they can be considered as highly-defective regions that block the electrical current passing from $Ni(Ge_{0.88}Sn_{0.12})_2$ effectively.

In conclusion, this chapter focused on understanding laser thermal annealing's effect on relaxed GeSn with Sn concentrations up to 11.2 at.% and Ni/GeSn contacts' resistance ρ_c. Here, we discussed the effect of varying the energy density and Sn composition on the morphological and compositional changes of GeSn upon annealing. Certain EDs were found to trigger Sn diffusion towards the surface. However, the specific contact resistance in nickel contacts was lowered by a factor of 100 as a result of forming a Ni-based GeSn alloy after LTA, while buried GeSn layers preserved their quality upon annealing at certain conditions. This serves as proof for the potential of implementing this technique in the functionalization of future GeSn-based devices' contacts. For this matter, the next chapter targets *in situ* doping of GeSn, which is another critical element in the fabrication of highly-performing ohmic contact.

CHAPTER 5 *IN SITU* N-TYPE AND P-TYPE DOPING OF PARTIALLY-RELAXED $GE_{0.91}SN_{0.09}$

5.1 Introduction

The development of n-type and p-type doped semiconductors is paramount for the design and fabrication of optoelectronic devices [4]. Doping levels in the 10^{18} cm^{-3} range are commonly used, for instance, in p-i-n GeSn multilayer heterostructures needed in the fabrication of photodetectors, [163-165] light-emitting diodes, [166-169] and lasers[170, 171]. In addition, higher doping levels (above 10^{19} cm^{-3}) are often required in devices such as in FinFETs and MOSFETs, [172, 173] and MIR plasmonic sensors [174, 175]. Moreover, these high doping levels are crucial for reducing the parasitic resistance of ohmic contacts in M-S junctions, as discussed in Section 2.2. The control of the doping level to reach active carrier concentrations in the 10^{19} cm^{-3} range and above is still an outstanding challenge for high Sn-content GeSn, [30] especially for n-type doping, given that undoped GeSn has an intrinsic p-type background doping in the 10^{17} cm^{-3} range [55, 110, 112, 115]. Furthermore, the investigation of *in situ* doping of partially-relaxed GeSn, at a high Sn-content of 9 at.%, has not been previously reported in the literature.

In this chapter, a systematic study is carried out to investigate p- and n-type doped, as-grown, and partially relaxed GeSn semiconductors. The chapter starts with the choice of the doping process, and the precursors used in RPCVD *in situ* doping. Next, we discuss the growth and characterization of relaxed p- and n-doped GeSn. Finally, we present the impact of doping on the electrical characteristics of GeSn M-S devices.

5.2 Choice of the doping process, dopant atoms, and their precursors

There are typically two distinct methods to dope semiconductors, *in situ* and *ex situ* processes [176]. Generally, achieving highly doped semiconductors is carried out through *ex situ* processes, which rely mainly on ion implantation and subsequent thermal activation [176]. However, one drawback of this process is that it usually degrades the crystalline quality of the implanted region [177]. Furthermore, the incorporated dopant atoms are not electrically active, requiring thermal

annealing to promote their diffusion into substitutional lattice sites [177]. For GeSn metastable semiconductors, thermal processing can severely degrade, if not compromise, their structural and optoelectronic properties. It has been shown that rapid thermal annealing at 350 °C of phosphorus- (P-) implanted $Ge_{0.93}Sn_{0.07}$ can lead to dopant activation without significant Sn segregation. However, the activation rate was below 0.1 % for all of the studied implant doses [178]. Thus, more advanced annealing processes, such as millisecond flash lamp annealing (FLA) or nanosecond laser annealing (NLA), must be employed for dopant activation in GeSn, as they may allow for high dopant activation while preserving the quality of the epilayers. For this purpose, active n-type doping levels in the 10^{19} cm^{-3} range were demonstrated in P-implanted $Ge_{0.95}Sn_{0.05}$ subsequentially treated with FLA. Although, small structural damage was induced during the activation, where Sn diffuses towards the crystalline/amorphous GeSn interface, which was created by ion implantation [176]. Furthermore, most of the thermal energy in these FLA and NLA processes is typically focused in the first 100 nm below the surface, and deeply buried layers would remain intact after processing, as discussed in Chapter 4. While being an advantage for treating surface layers, similar dopant activation in more complex structures such as p-i-n junctions cannot be achieved with FLA-NLA.

in situ doping of GeSn is obtained by incorporating dopant atoms directly in the active substitutional lattice sites during the epitaxial growth, by supplying either a group-III or group-V precursors for the p- or n-type doping, respectively. Using this method, higher control of the doping profile and its uniformity across the sample's depth can be achieved, and doped layers with a thickness of a few hundreds of nm can be grown, exceeding the total thickness that can be typically doped by ion implantation [179].

In this chapter, we studied *in situ* doping of GeSn grown by RPCVD. For the growth of p-type GeSn layers, boron (B) was selected as the impurity dopant because of its multiple advantages over other group-III elements [180-185]. First, B has been extensively used for Si and Ge doping, [180] in both *ex situ* and *in situ* doping processes, eventually reaching degenerate doping levels above 10^{20} cm^{-3} in Ge [181, 182]. Second, the diffusion coefficient of B in Ge is 1.5×10^{16} cm^2/s [183]. This value is substantially lower than that of Gallium, which is the other most prominent dopant element in Ge. This low diffusivity preserve the interface abruptness in a multilayer heterostructure during subsequent processing or growth steps [184]. For the B precursor dedicated to the growth

of p-type GeSn, di-borane (B_2H_6) was used. Note that B_2H_6 is a standard precursor commonly used in RPCVD reactors for CMOS commercial applications. Hence it aligns with our global objectives towards the monolithic integration of GeSn on Si platforms. Furthermore, the decomposition of B_2H_6 already takes place above 250 °C, [185] which is compatible with the low growth temperature of GeSn semiconductors.

As for n-type GeSn growth, arsenic (As) was selected as the impurity dopant rather than the commonly used P. The most important reason in this choice is the closer covalent radius of As to those of Ge and Sn as compared to P. Consequently, the reduced distortion in the GeSn lattice induced by As atoms is expected to lead towards higher active doping levels than that for P doping. This behavior was recently shown in pseudomorphic GeSn and SiGeSn, where 10x higher doping levels were achieved [186]. Arsine (AsH_3) was selected over the organometallic Tertiarybuthyl-arsine (TBA) as As precursor, because of its higher chemical purity, *i.e.* absence of carbon-related byproducts during the growth and compatibility with gas phase growth. In addition, preliminary SIMS profiling on one of our n-GeSn samples grown with TBA precursor revealed parasitic incorporation of carbon atoms, which are typical for MO precursors during low-temperature growth [185].

Lastly, for the expected doping levels in GeSn via *in situ* doping, and since non-equilibrium growth processes are necessarily implemented for GeSn growth, non-equilibrium doped growth is likely to result in active doping levels exceeding the theoretical equilibrium solubility of B and As in Ge of 5.5×10^{18} cm^{-3} and 8.0×10^{19} cm^{-3}, respectively [187].

5.3 p-type GeSn growth and characterization

5.3.1 Epitaxial growth

The p-type GeSn samples were grown according to the layout illustrated in Fig. 5.1a. The B_2H_6 precursor flow was controlled over one order of magnitude (0.5-4.9 sccm), while the GeH_4 flow was kept constant (90 sccm). Samples were labeled according to a B_2H_6 flow rate multiplier, ranging from the lowest flow labeled as (1x), to the highest flow labeled as (10x). Moreover, the stack consisted of three undoped relaxed GeSn layers. The top-layer (TL) in the reference undoped sample was grown for 2 hrs at 320 °C, with a thickness of ~300 nm [3]. For the doped samples, the

TL was first grown undoped for 1 hr under the same conditions, and then a fixed B_2H_6 flow was added to the growth recipe for an additional 1 hr.

5.3.2 Impact of B doping on the growth kinetics and morphological quality of GeSn

First, the crystalline quality of doped GeSn samples was investigated using TEM. TEM images of the 10x sample (Fig. 5.1b), show that the threading dislocations are mainly located in the first two GeSn buffer layers (#1-2), while high crystalline quality is confirmed for both the undoped TL, and the p-type doped GeSn layer. Thus, the doping precursor seems to have no noticeable effect on the crystal structure of GeSn. In addition, the TEM image indicates that the addition of B_2H_6 during the growth has no notable effect on the growth rate, since the total thicknesses of the two topmost layers are similar. This result stands in sharp contrast to recent observations in highly-strained GeSn layers, [30, 188] where a strong decrease in the growth rate was observed as B_2H_6 flow increases up to 30 sccm [30, 188].

To further investigate the crystalline quality, XRD (2θ-ω) (004) scans were acquired, and the obtained results are shown in Fig. 5.1c. In the undoped GeSn sample, three peaks are observed. The Ge-VS peak is above 66°. Peaks observed at lower angles correspond to the slightly compressive-strained GeSn layers with Sn compositions of 4.9 at.% (#1), 5.8 at.% (#2), and 7.9-8.7 at.% Sn (TL). More details on this will be further discussed below. By introducing B_2H_6, the underlying layers (#1-2) are unaffected, while the TL shifts towards higher angles. As previously established in Section 3.3.1, at a fixed strain value, a shift of the XRD peak to higher 2θ angles corresponds to a lower Sn composition, and at a fixed Sn-content, a shift to higher 2θ angles would indicate a higher degree of strain relaxation in the GeSn layer. Hence, the TL peak shift with increasing B_2H_6 flow suggests a reduction in its Sn-content (by at least 1 at.% Sn in the 10x sample), as a result of the incorporation of B atoms in the GeSn lattice. Finally, the $10 \times 10\ \mu m^2$ AFM maps (Fig. 1d-g) suggest a good epitaxial quality of the GeSn doped layers, since the <110>-oriented crosshatch pattern seems to be unaffected by the B_2H_6 flow rate, and the RMS roughness value is the same as in the undoped sample (in the 7-10 nm range).

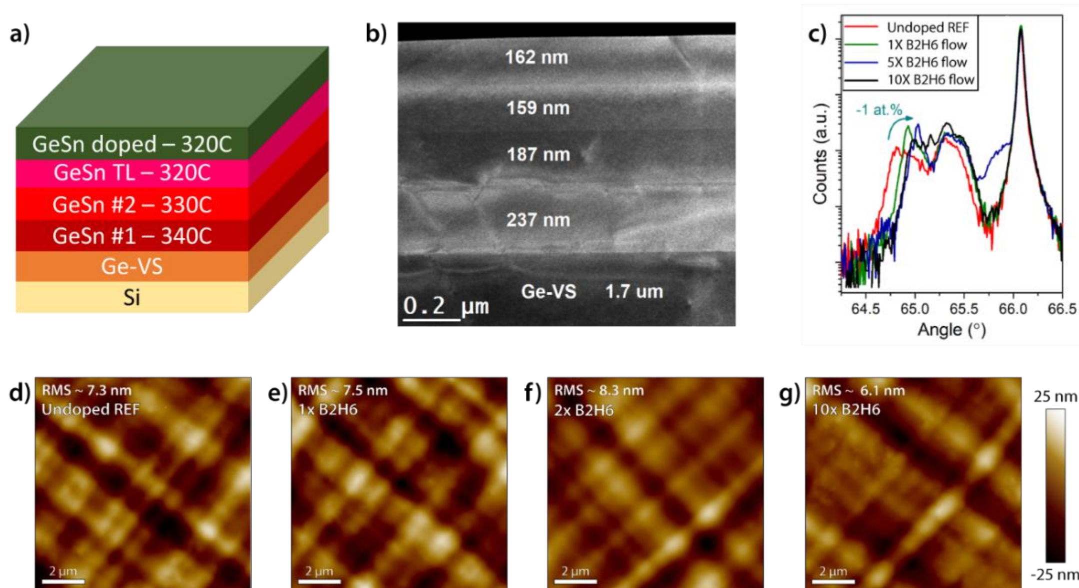

Figure 5.1 a) schematic illustration of the GeSn:B growth layout; b) Cross-sectional TEM image of the 10x B_2H_6 sample layer stack; c) GeSn:B samples set (2θ-ω) curves; d-g) 10 × 10 µm AFM maps with their corresponding B_2H_6 flow rates.

To decouple the effect of B *in situ* doping on the strain and composition of the p-GeSn layer, RSM measurements around the asymmetrical (224) XRD reflection were performed, and the obtained results are shown in Fig. 5.2. As depicted, the composition and strain of the first two layers #1 and #2 remain unchanged. However, the TL peak strongly shifts to higher q_z values (Section 3.3.1) with increasing B_2H_6 flow (arrow in Fig. 5.2), and the highest marked reduction in the Sn-content is from 8.7 at. % (undoped) to 6.2 at. % (10x). Note that this trend is in agreement with the (004) XRD scans displayed in Fig. 5.1c.

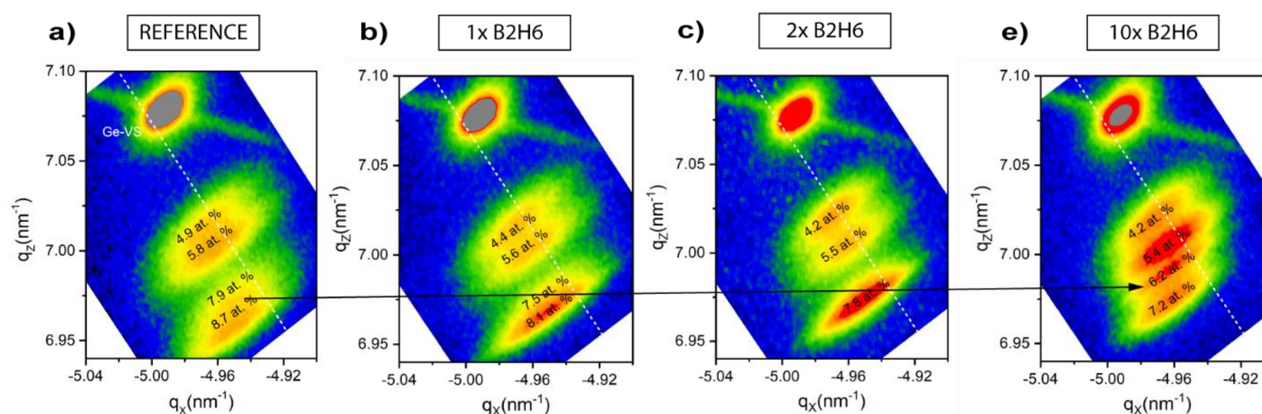

Figure 5.2 XRD-RSM (224) reflection maps for the GeSn:B samples set with their respective B_2H_6 flows, the arrow indicates the diffraction spot of the topmost layer.

A similar reduction in Sn-content with B_2H_6 flow was previously observed in pseudomorphic GeSn layers with Sn incorporation up to 10 at %, [30, 181, 188] and can be attributed to two underlying mechanisms. The first mechanism generally applies to samples grown at high growth rates above 10 nm/min. For these conditions, increasing the B_2H_6 flow resulted in a significantly higher growth rate, and consequently, a lower Sn incorporation [30]. However, given that our samples were grown at much lower growth rates around 2.5 nm/min, and considering that the TEM image in Fig. 5.1b shows no difference in the thicknesses of the doped and undoped layers. No significant change in the growth rate of our samples is observed, and this mechanism is not the major contributor to Sn reduction in our case. The second and more likely mechanism is the surface-site competition between B and Sn during the growth [181, 189]. The origin of this competition was studied extensively. In addition to *in situ* observations, it was revealed through *ex situ* B doping of GeSn via post-epitaxial B implantation followed by rapid thermal annealing, and first-principle calculations of the GeSn:B system, that B atoms are energetically favored to occupy Sn lattice sites rather than Ge sites in the GeSn:B system [190]. Hence, the Sn-content decrease with increasing B_2H_6 flow observed in our samples is caused by this surface-site competition between B and Sn during the growth. This trend was verified in our CV data discussed further below in the following section.

As for the strain, B atoms have a smaller covalent radius compared to Ge and Sn atoms. Henceforth, substitutional B atoms would in principle relax the compressive strain in GeSn. However, because of the very low density of B atoms in the lattice, about 1 B atom every 100 Sn atoms for the 10x B_2H_6 sample, a negligible deviation from the lattice parameter of undoped GeSn is expected. Instead, the Sn reduction with increasing B_2H_6 flow is the main reason for the doped p-GeSn layers to be more relaxed than the TL in the undoped reference.

5.3.3 Boron doping concentration and activation ratio

To gain more information on the compositional profile of B atoms in the GeSn lattice, dynamic SIMS measurements were performed. The depth profiles are displayed in Fig. 5.3. First, the Ge signal's sudden increase close to the samples' surface is as a result of the initial SIMS beam stabilization. It is more pronounced in the 10x sample with a total depth of 150 nm (Fig. 5.3d). More importantly, a small B signal in the upper 150-200 nm region of the stacking is visible in the 1 x sample (Fig. 5.3b), and its intensity further increases with increasing flow, both in 2x (Fig. 5.3c) and the 10x (Fig. 5.3d) samples. In addition, the B-content is uniform throughout the entire 160-180 nm thickness of the layer, which is one of the important characteristics to be verified for *in situ* doping.

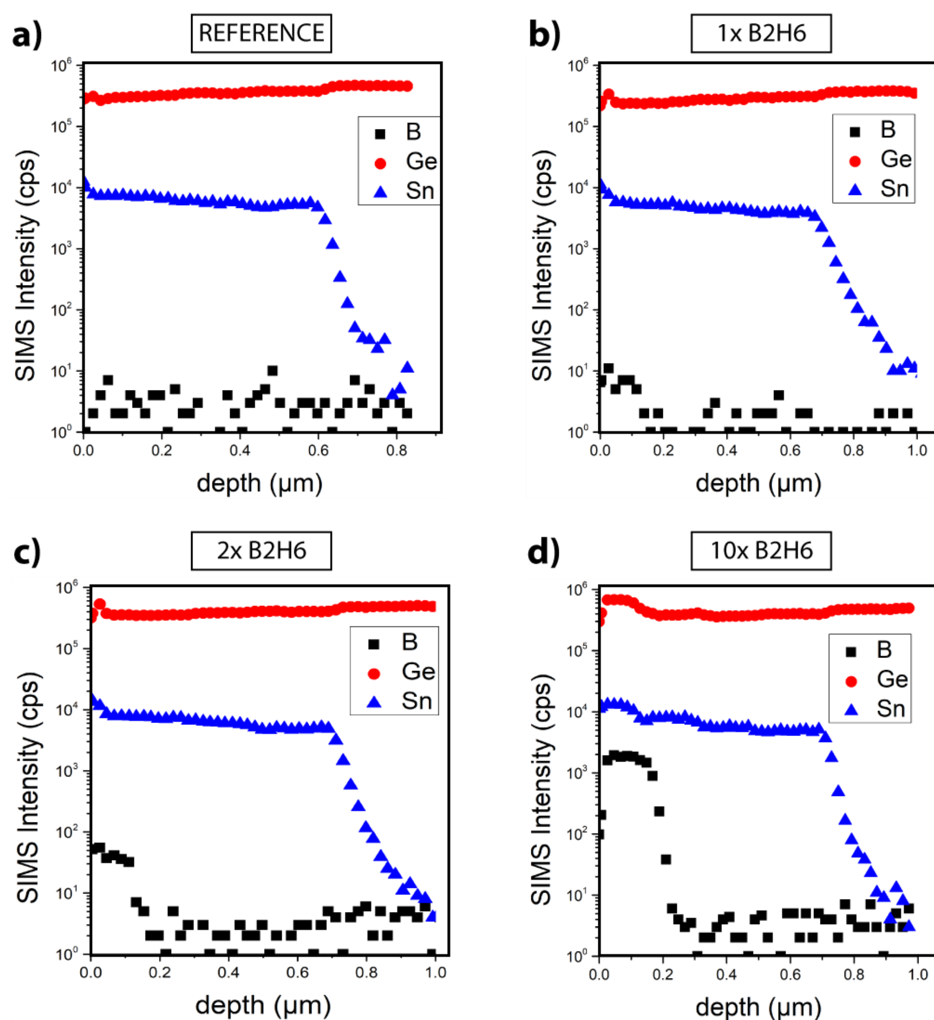

Figure 5.3 SIMS composition *vs.* depth profiles for the GeSn:B samples set with their respective B_2H_6 flow rates.

To determine the active doping level in GeSn, conventional and back-to-back MOS capacitors were fabricated using the doped GeSn samples, and following the process described in Section 3.3.2. The normalized capacitance *vs*. bias voltage is plotted for the four GeSn samples in Fig. 4a. Doping levels of 4.7×10^{17}, 2.3×10^{18}, 6.6×10^{18}, and 1.1×10^{19} cm^{-3} were estimated in the undoped, 1, 2, and 10x B_2H_6 flow samples, respectively. For the reference GeSn sample, the source of the unintentional p-type background doping has been attributed to the presence of point defects in the GeSn lattice [158, 159]. For this sample, the capacitance slightly increases in the weak inversion

region before it finally stabilizes. This is typical in C-V curves for narrow bandgap semiconductors measured at high frequencies. This effect was previously reported in Ge and pseudomorphic GeSn, and it is often referred to as "weak inversion hump" [110, 115, 191]. The main mechanism behind this effect is the strong minority inversion response witnessed in narrow bandgap semiconductors, which allows for a higher interaction of midgap traps with the CBE and VBE [191]. It is important to note that this effect does not influence the calculated doping level, since the latter is extracted from the slope in the transition region, which is not affected by this phenomenon [191]. In addition, it can be seen that the difference in the capacitance values between the accumulation and inversion regions decreases significantly as the doping level increases. Thus, an underestimation of the doping level is more probable for samples with higher doping levels. This highlights the importance of using higher-*k* dielectric oxides, or lower equivalent oxide thicknesses of the SiO_2, to increase device precision for high doping levels (Section 3.3.2). However, the attained doping level of 10^{19} cm^{-3} is reasonable enough to achieve a low contact resistance for p-GeSn, especially given the low hole SBH due to the FLP near the VBE in M/p-GeSn devices.

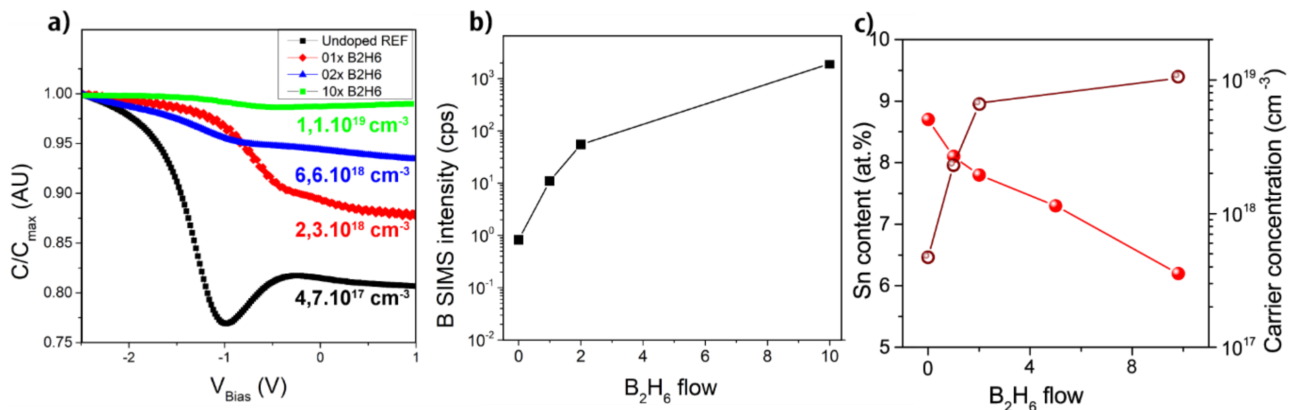

Figure 5.4 a) Capacitance-Voltage plots of the GeSn:B MOS Capacitors; b) SIMS Extracted boron intensity as a function of B_2H_6 flows; c) Sn-content and boron active carrier concentration as a function of B_2H_6 flows.

Next, the average B signal intensity was extracted from the SIMS profiles and plotted as a function of the B_2H_6 flow in Fig. 5.4b. In addition, the B SIMS signal was converted to carrier concentration by normalizing the Ge signal to the Ge bulk density of 4.42 x 10^{22} cm^{-3}. For this process, similar

ionic yield rates were assumed for Ge, Sn, and B atoms. This assumption was subsequently confirmed using atom probe tomography's results (not shown). Finally, the activation rate was then calculated as the B concentration ratio extracted from CV divided by the normalized B intensity from SIMS profiling. The calculated activation rate was higher than 80 % for both the 1x and 2x samples, and ~ 40 % for the 10x sample. We note that the last value is most likely underestimated by the presence of an unusual signal spike in the SIMS profiling, and the use of the low-*k* dielectric SiO_2 as a gate oxide.

For a comprehensive image, the reduction in Sn-content induced by the B active incorporation in relaxed GeSn samples is further displayed in Fig. 5.4c. In this regard, the results are in good agreement with the values of Sn reduction established for B-doped pseudomorphic GeSn [189, 192]. Thus, strain relaxation is likely not an important factor for the B incorporation in substitutional sites for the GeSn system. In addition, the active B concentration *vs.* B_2H_6 flow suggests that further increasing the flow may not result in a significant increase in the B active doping level, compared with lower B_2H_6 flows.

5.3.4 Impact of the growth temperature on B incorporation of GeSn:B

To explore B incorporation in GeSn at lower temperatures, *i.e.,* the main parameter used for higher Sn incorporation, [3] an additional sample was grown, in which the TL doped layer was grown at 305 °C rather than 320 °C used for the samples described above. For the characterization results, the TL in the undoped sample reaches a Sn-content of ~8 at. %, while the Sn-content decreases below 7 at. % with a B_2H_6 flow of 6x (Fig. 5.5a). Moreover, the 10 × 10 µm AFM maps of the reference (Fig. 5.5b) and doped (Fig. 5.5c) samples, show similar morphology and RMS roughness compared with the former samples. However, the CV data (Fig. 5.5b) yielded a doping level of $2.2x10^{19}$ cm^{-3}, which is higher than the expected doping level for samples grown at 320 °C with the same B_2H_6 flow, following the curves in Fig. 5.4c. As a consequence, despite the similar reduction in Sn-content with B incorporation at growth temperatures of 305 °C and 320 °C, a higher active doping was obtained for the former. Hence, decreasing the temperature might help in the incorporation of B atoms in partially relaxed GeSn. However, lowering the growth temperature in the B-doping process of pseudomorphic GeSn led to a lower B incorporation in these layers [30].

Consequently, it could be possible that reaching highly-doped, high Sn-content, and relaxed GeSn is more achievable compared with pseudomorphic GeSn discussed in [188].

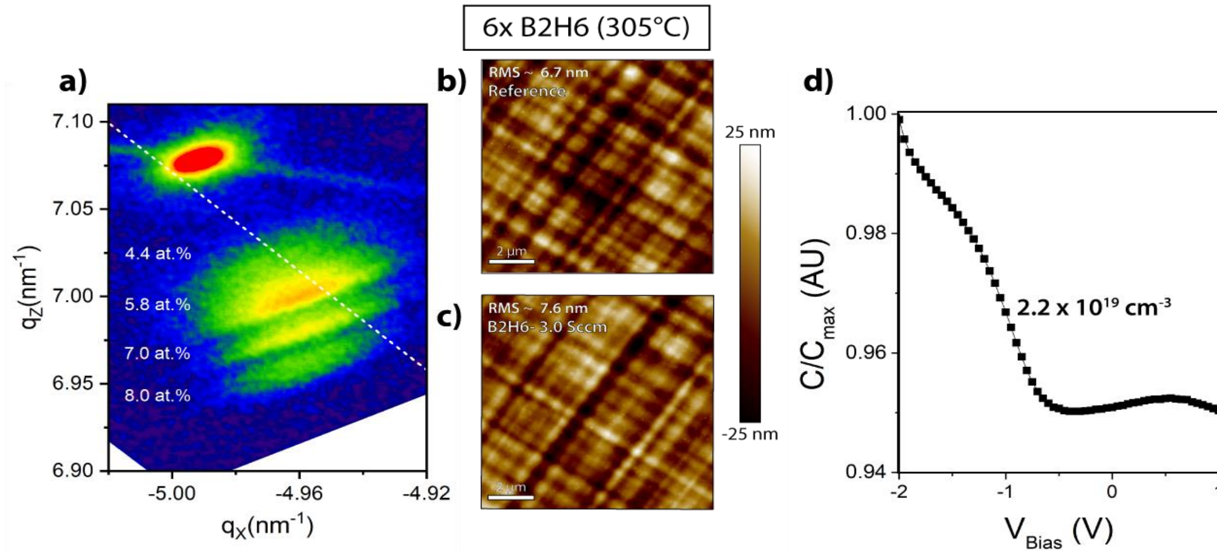

Figure 5.5 GeSn:B sample set with the topmost layer grown at 305 °c: a) XRD-RSM (224) map of the 6x B_2H_6 flow sample, b) and c) 10 × 10 µm AFM maps for the undoped reference and doped sample respectively, d) Capacitance-Voltage plots of the 6x GeSn:B MOS Capacitors.

5.4 N-type doping of relaxed GeSn

5.4.1 Epitaxial growth

The stackings used in the growth of n-GeSn are illustrated in Fig. 5.6. The AsH_3 flow was varied over two orders of magnitude (0.08-2 sccm) at a TL growth temperature of 320 °C (Fig. 6a), 315 °C (Fig. 6b), and 305 °C (Fig. 6c). For the n-GeSn growth using the layout in Fig. 5.6a. The undoped sample shown in (Fig. 5.2a) again serves as the undoped reference for this set. The XRD-RSM (224) maps for samples in this set are shown in Figs. 5.7a, 5.7b, and 5.7c for the undoped, AsH_3 at 4x, and 25x flows, respectively. By introducing AsH_3 during growth, the graded composition to 8.7 at. % vanishes, and only the GeSn layer with 7.9 at % Sn peak is visible, which suggests that the n-GeSn growth rate is strongly suppressed. Moreover, in the TEM image of the 25x sample (Fig. 7d), only the first three GeSn layers are visible, implying a complete suppression

of the n-GeSn growth. Furthermore, no noticeable morphological differences can be seen in the AFM maps (Figs. 5.7e-g) between the undoped sample and those grown with AsH_3, which confirms the growth suppression rather than a 3D islands-like growth.

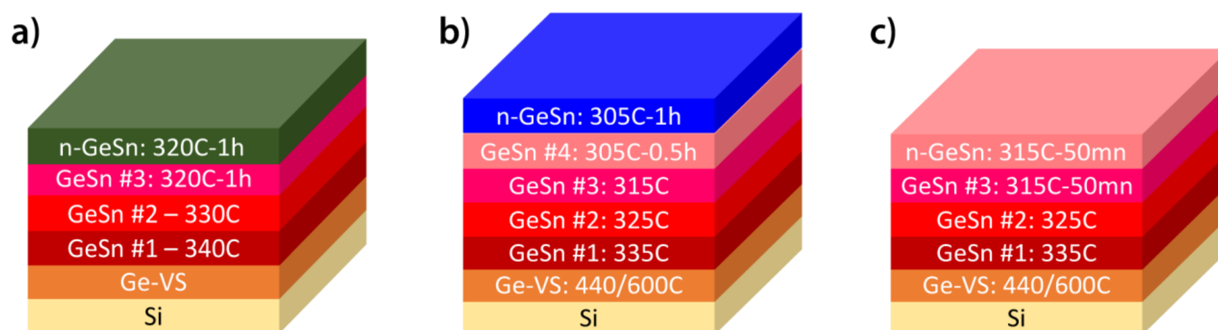

Figure 5.6 schematic illustration of the GeSn:As growth layout: a) for the first set, b) and c) for the second set of samples.

5.4.2 Impact of As doping on the morphological quality of GeSn

One possible explanation of the growth suppression can be obtained by comparing our GeSn doping process with the growth of As-doped Si layers [193]. During the growth of the latter at high AsH_3 flows, adsorbed As atoms form symmetrical As-As dimers on the Si surface, where two As atoms are bonded with a Si surface atom and completely saturate the Si surface bonds, which blocks the adsorption sites from other hydrides. This mechanism quenches the growth of doped Si:As layers. A similar saturation mechanism was attributed to Ge and Sn surface atoms in pseudomorphic GeSn [186]. Thus, at the 4x and 25x AsH_3 flows used in this set, a similar process is likely leading to the observed growth suppression.

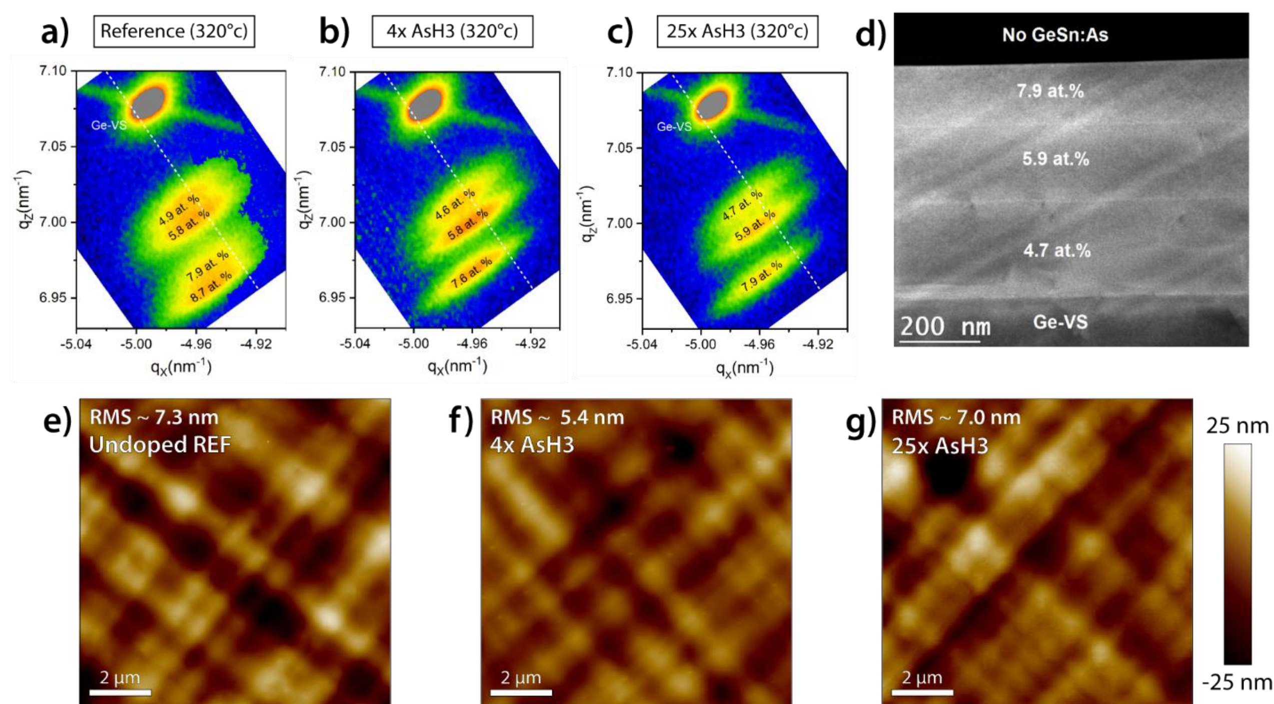

Figure 5.7 GeSn:As samples: a-c) XRD-RSM (224) maps with their corresponding AsH_3 flows, d) Cross-sectional TEM image of the 25x AsH_3 sample, e-g) $10 \times 10\ \mu m^2$ AFM maps with their corresponding AsH_3 flows.

Next, a second set of samples was grown, where the AsH_3 flow was reduced by 250 times to reach a value of 0.1x AsH_3. The layouts used in this growth are found in Fig. 5.6b at 305°C and Fig. 5.6d at 315 °C. The obtained results are shown in Fig. 5.8 for the set with TLs grown at 305 °C only, to limit the displayed data. Starting with the $10 \times 10\ \mu m^2$ AFM map on doped GeSn:As shown in Fig. 5.8a, the <110>-oriented crosshatch pattern persists, and the RMS roughness values stay in the 7-10 nm range similar to the undoped reference, indicating a good epitaxial quality of the GeSn:As samples. In addition, the map reveals small droplet-like shapes homogeneously visible throughout the map. The latter were not identified to be Sn-rich or As-rich, although they indicate an influence of As incorporation on the morphological or compositional properties of GeSn, which are discussed in the following paragraphs.

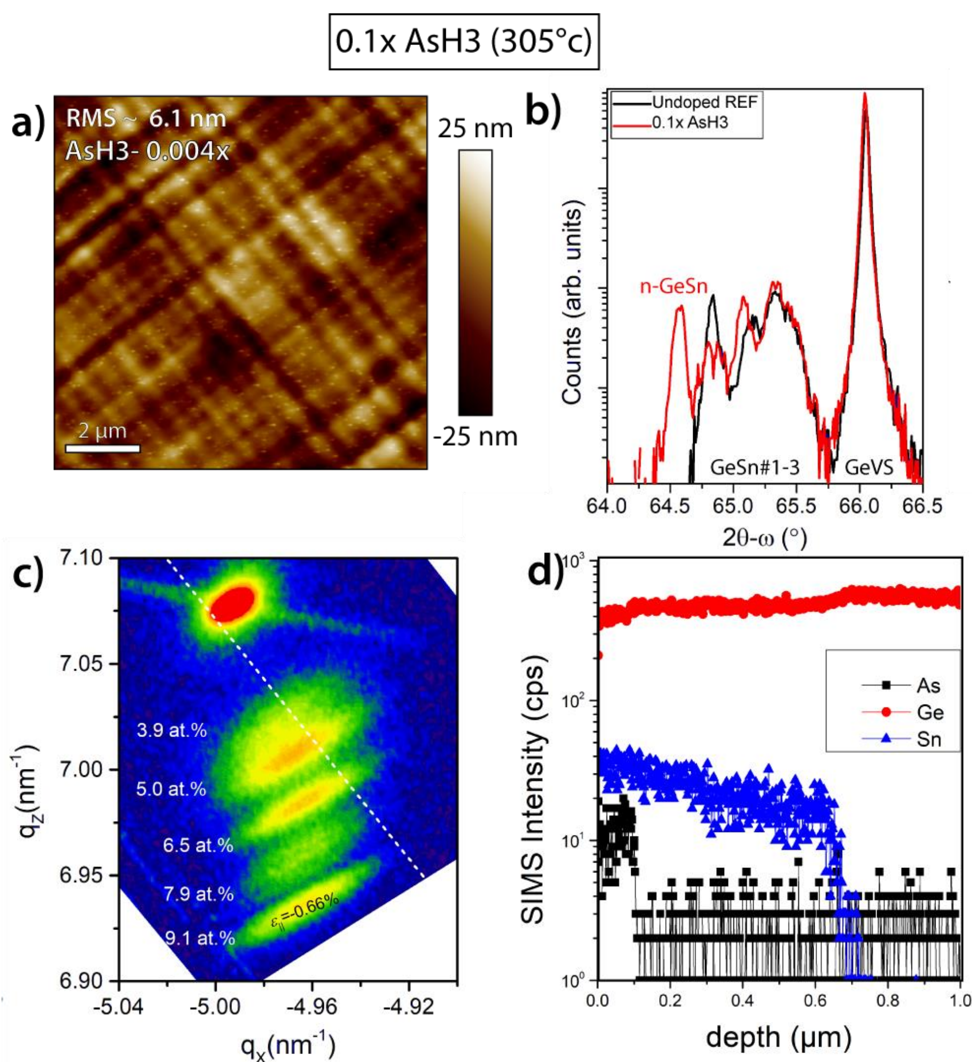

Figure 5.8 0.1x AsH_3 doped GeSn:As samples: a) $10 \times 10\ \mu m^2$ AFM map on the doped sample, b) (2θ-ω) curves of the samples; c) XRD-RSM (224) maps of the doped GeSn:As samples. d) SIMS composition *vs*. depth profiles

Following that, XRD (2θ-ω) scans are shown in Fig. 5.8b. The presence of a n-GeSn layer is clear from the additional peak at lower angles (64.6 °). In addition, the shift in 2θ from 64.8 ° for the undoped reference to 64.6 ° for the n-GeSn, suggests an increase in Sn-content in the latter. Moreover, the RSM map in Fig. 5.8c on the 0.1x sample further confirms the increase of 1.1 at.% Sn in the n-GeSn layer, and shows that the layer is pseudomorphically-grown on the undoped 7.9 at.% buffer layer, with a higher compressive strain value relative to the TL in the undoped

reference. The increase in Sn content upon As incorporation is surprising and stands in sharp contrast to earlier observations on pseudomorphic GeSn:As [186]. To further investigate this behavior, the SIMS depth profile was acquired for the 0.1x sample (Fig. 5.8d). A clear As signal is detected in the upmost 100 nm region of the stack, and a relatively higher Sn signal is noted for the first layer, compared with the layer below it that is grown at the same conditions. This further suggests the enhanced Sn incorporation with the AsH_3 supply.

So far, little is known about the exact origin of this mechanism. However, a recent paper [194] highlighted the Vacancy-Arsenic complexes' (V-As) role as a possible explanation of higher Sn incorporation in the GeSn:As system. During the growth, mobile V-As complexes with single, double, and triple As atoms, can form in high concentrations. Consequently, the presence of vacancies during the growth of GeSn assists in the direct As incorporation into active lattice sites. In addition, the presence of these complexes in high concentrations can help in creating V-As-Sn complexes, which may lead to an increase in the Sn level.

Moreover, from a chemistry point of view, it has been shown that the growth of metastable GeSn at low temperatures takes place according to highly complex reaction pathways between the $SnCl_4$ and GeH_4. These allow for the adsorption and surface reaction of Ge and Sn complexes, leading to the incorporation of Ge and Sn atoms into lattice sites [195]. It is possible that the addition of AsH_3 can act as a surfactant, and thus lower the surface energy during the growth of relaxed GeSn more effectively than in compressively-strained GeSn. The latter could enhance the decomposition rate of $SnCl_4$ on the surface, thereby increasing the Sn-content incorporated into the material. Moreover, the surfactant effect was already noted in the growth of Sb-doped GeSn [196, 197].

5.4.3 Arsenic doping concentration and activation ratio

The normalized capacitance *vs.* voltage bias for the n-GeSn layers, grown with 4x and 25x AsH_3 flows are plotted in Figs. 5.9a, and those grown with 0.1xAsH_3 flow are plotted in Fig. 5.9b. First, we note the inversion of the accumulation and depletion regions compared with p-type samples (Fig. 5.4a), which confirms the n-type behavior. The latter is a direct implication of the total compensation of the background p-type concentration seen in undoped Ge and GeSn, [198] as a result of the high incorporation of active As in the GeSn:As layers.

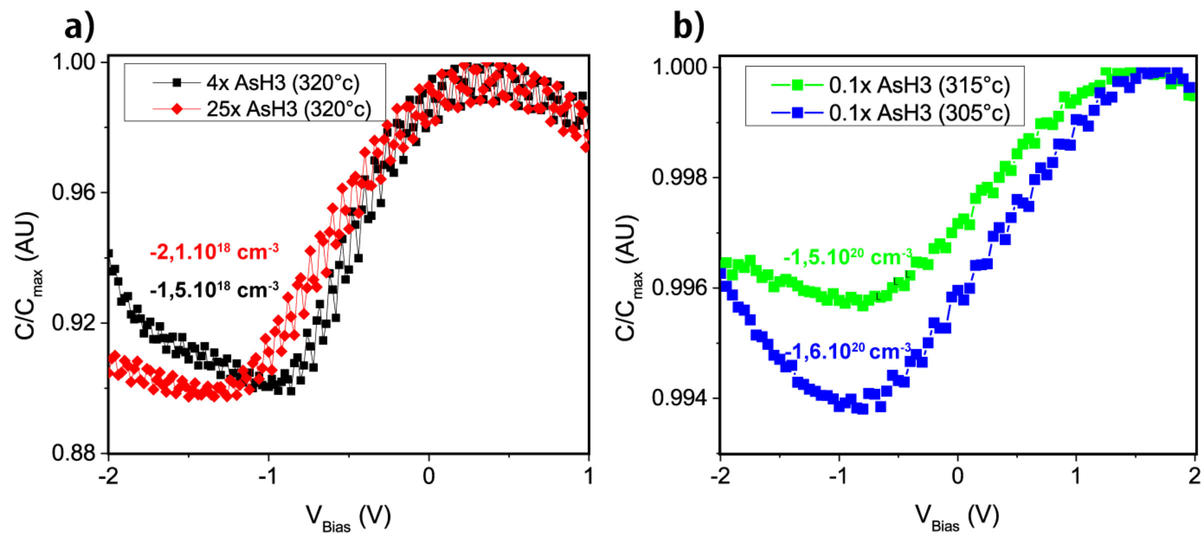

Figure 5.9 Capacitance-Voltage plots of GeSn:As MOSCap devices: a) for the first set, b) for the second set of samples. The negative sign signifies n-type doping

For the 4x and 25x samples, an n-type doping level in the order of 10^{18} cm^{-3} was estimated. This indicates that an ultra-thin doped region must be present at the samples' surface, despite not being clearly visible in TEM images. Moreover, this layer's very small thickness might be a reason for the high fluctuations in the CV data. As for the 0.1x samples, an n-type doping level in the 10^{20} cm^{-3} range is obtained. It is worth mentioning that detecting such a high doping level using SiO_2, as a low dielectric oxide with a relatively high thickness of 23 nm, is quite uncommon. For voltages above $|V_{max}|$= 1V, charge trapping in the low-*k* dielectric starts, which is caused by electrons tunneling through the oxide. This leads to the variation of capacitance in these regions instead of the theorized stabilization [111]. Thus, these MOS devices cannot be used for multiple times to extract values with the same accuracy as in the first measurement.

Furthermore, the averaged As signal of the doped region in the SIMS profiles (Fig. 5.8d) was converted to carrier concentration, using the same process as in the p-GeSn section. The calculated activation rate is around 10 %. Although, a low activation ratio at this doping level is a possibility, for example, as a result of the segregation of dopant atoms. This possibility would in fact explain the droplets-like shapes in the AFM map (Fig. 5.8a). However, the activation rate is highly underestimated for two main reasons. The first is the high possible underestimation of the active

doping level in the CV data, as established earlier. The second reason is that As^- secondary ions are 98% close in their molecular weight with GeH^- ions. Hence, they contribute to the same peak in the spectrum that is fitted to extract their intensity. Although the GeH^- signal is minimized by optimizing the primary beam parameters, the residual signal can still interfere with the results, which in turn influences calculations on the active rate. However, to the extent of the aforementioned applications, this doping level is highly sufficient, and can be directly used to specifically target an ultra-low contact resistance in n-type M-S junctions. Finally, it is worthy to note that both of the 0.1x samples had a very high doping level despite the difference in their growth temperature. This indicates the higher likelihood of achieving high doping levels in relaxed GeSn:As compared with GeSn:B at the slow growth rate conditions employed in this study.

5.5 Impact of boron and arsenic incorporation on the electrical properties of GeSn M-S devices

In the following, we study the impact of the doping level on the electrical properties of metal contacts on p-type and n-type GeSn. For this reason, TLM devices were fabricated by patterning via conventional photolithography, and e-beam deposition of a Ti/Au stack, with 10/60 nm in thicknesses, respectively. Metal evaporation was realized at 10^{-7} Torr base pressure, and the fabrication was finalized by metal lift-off. Ti was selected as a metal contact to investigate fermi-level pinning, since a Schottky behavior is expected for GeSn:As at moderate doping levels (10^{18} cm^{-3}), despite the work function of Ti that has a value of ϕ_{Ti} = 4.35 eV, hence theoretically close to CBE in GeSn 10 at% Sn (Fig. 2.1) [27]. For each sample, more than 5 device sets were measured, and the results are shown in Fig. 5.10.

Starting with Ti/Au on p-GeSn, results are plotted in Figs. 5.10a and 5.10b. The IV plots for a single set of TLM devices fabricated on the 10x B_2H_6 flow sample (Fig. 5.10a) reveals a perfectly linear ohmic behavior for all spacings d_s. This behavior is expected for p-type GeSn at this high doping level, caused by the strong FL pinning near the VBE. In addition, the extracted total resistance was used to estimate the specific contact resistance ρ_c. The contacts revealed a sheet resistance of 42.0 $\Omega.sq^{-1}$ and a ρ_c=3.06 $\times10^{-5}$ $\Omega.cm^{-2}$ for the 10x sample, as well as 780.0 $\Omega.sq^{-1}$ and a ρ_c= 1.46 $\times10^{-4}$ $\Omega.cm^{-2}$ for the 1x sample. These results are sufficient for some optoelectronic

devices [5]. However, it is important to note that ρ_c for the 10x sample is largely overestimated by at least an order of magnitude, as a result of the non-negligible parasitic resistances, as discussed in Section 3.3. Optimization of the contact using Ni stanogermanides instead of Ti is important to further lower ρ_c in future optoelectronic devices, as established in Section 2.3

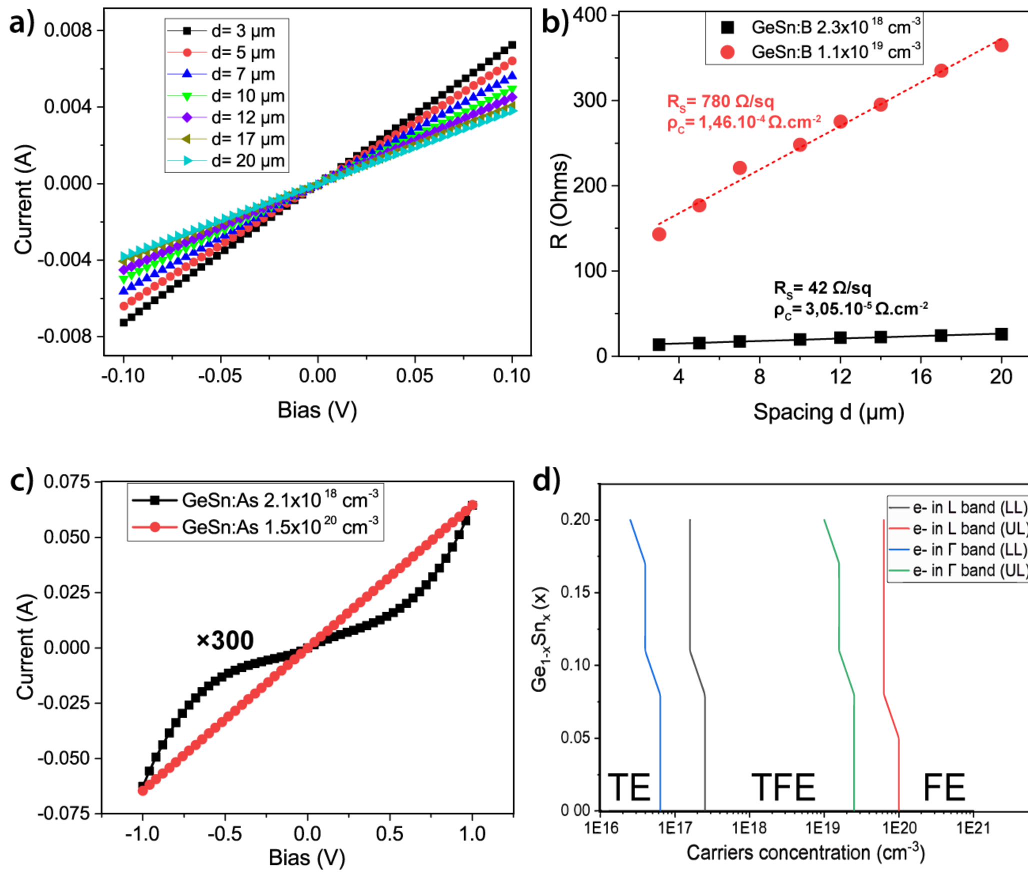

Figure 5.10. a) IV plots extracted from TLM devices on the 10x B_2H_6 samples; b) R_T *vs*. d_s for Ti/Au on the GeSn:B samples; c) IV plot extracted from the TLM device with ds=3 μm, of the GeSn:As samples; d) Thermionic field emission lower limits (LL) and upper limit (UL) for n-type carriers in $Ge_{1-x}Sn_x$: $0 < x < 0.2$.

On the other hand, to better understand the IV behavior of Ti/Au on n-GeSn, the corresponding current transport mechanisms were calculated as a function of the doping level and Sn-content, and results are plotted in Figs. 5.10d. The Upper Limit (UL) and Lower Limit (LL) of the thermionic

field emission transport mechanism signify the boundaries of each dominant transport mechanism. These were calculated using the tunneling probability, as described in ref [17]. The equation for the tunneling probability is given as:

$$E_{00} = \frac{qh}{4\pi}\sqrt{\frac{N_d}{K_s \varepsilon_0 m_{tun}^*}}, \quad (5.1)$$

where N is the doping level, and m_{tun}^* is the effective tunneling mass. Values for the latter were extracted for the electrons in the Γ and L bands in $Ge_{1-x}Sn_x$: $0 < x < 0.2$ from ref [97]. Next, the limits were defined based on the (UL) and (LL) values for pure Ge, and are given as follows:

$E_{00} \ll kT$ *i.e.,* < 0.1 kT. Thermionic emission dominates the current transport.

$E_{00} \approx kT$. Thermionic-field emission dominates the current transport.

$E_{00} \gg kT$ *i.e.,* > 10 kT. Field emission dominates the current transport.

The IV plot of the 10^{20} cm^{-3} doped GeSn:As sample is shown in Figs. 5.10c (red line). Here, the mechanism responsible for current transport is field emission, where electrons in the metal tunnel directly to the L band, [96] since the high band bending induced by the degenerate doping level allows for the tunneling current to be dominant even at very low voltage biases. This is why a perfect ohmic (linear) behavior is demonstrated, despite the high electron SBH calculated around 0.35 eV for relaxed $Ge_{0.9}Sn_{0.1}$, given the presence of strong FLP [27]. The extracted sheet resistance is 26.5 $\Omega.sq^{-1}$, and the specific contact resistance ρ_c is 3.87×10^{-05} $\Omega.cm^{-2}$. Although, the real values are largely overestimated for the same reasons mentioned earlier.

As for the IV plot of the 10^{18} cm^{-3} doped GeSn:As sample, thermionic field emission is the dominant current transport mechanism for electrons in both of the Γ and L bands, as indicated in Fig. 5.10d. As a consequence, the TLM M-S contacts on both sides, *i.e.* M-S-M contacts, act as back-to-back Schottky contacts, which is described in detail in [55]. Thus, the current in both negative and positive bias values is capped by the reverse bias current from each Schottky M-S contact, which is the reason for the symmetry in the IV plot, and a near-ohmic behavior is demonstrated. To be more precise, for low bias values, the barrier's width w is only thin enough at

a high energy level above the FL, and the form of the IV curve is typical to a Schottky device. As the voltage bias increases, the current corresponding to electron tunneling starts to dominate, and the total current starts to increase exponentially. The latter results from the combined effect of a lower barrier width caused by the high band bending, and less importantly, the lower effective barrier height caused by image-force lowering [47]. We finally note that this result also supports the presence of an ultra-thin n-type layer, as suggested by the C-V plots for the 4x and 25x samples.

As a summary, this chapter concentrated on understanding the *in situ* doping process during the growth of relaxed GeSn. Here, we demonstrated high doping levels in these layers. For p-type GeSn growth using B_2H_6, the active concentration was controlled in the 10^{17}-10^{19} cm^{-3} range at Sn concentrations between 6 and 9 at.%. In contrast, for n-type GeSn growth using AsH_3, a very high active concentration of 10^{20} cm^{-3} was achieved at a Sn-content of 9 at.%. M-S devices fabricated using these samples demonstrated their enhanced performance, and showed the associated effect of FLP, which degraded n-GeSn devices' performance at doping levels below 10^{20} cm^{-3}. The next chapter provides an overall conclusion of the work realized in this thesis, and future perspectives to guide the ongoing research on highly-efficient ohmic contacts to high Sn-content GeSn for SWIR/MIR applications.

CHAPTER 6 CONCLUSION AND PERSPECTIVES

In this chapter, we summarize the important findings discussed in this work. We start with the technological relevance of GeSn alloys, and the context of developing metal-GeSn contacts for device functionalization. Following that, we provide conclusions on and major contributions of the two experimental chapters, and their potential in accelerating the development and implementation of GeSn-based devices. Finally, we conclude this chapter by listing all of the questions raised by this work, and future perspectives to guide the ongoing research on metal-GeSn ohmic contacts.

6.1 Main conclusions

GeSn-based semiconductor alloys grown on Si wafers offer a robust, affordable, and highly scalable platform for fabricating highly efficient IR active and passive devices, operating in the SWIR and MIR spectra. Their CMOS compatibility could enable their ultra-large scale integration with electronics in the same chips. This would enable the fabrication of next-gen technologies, such as affordable SWIR vision for self-driving cars, and PICs for faster communication speeds and lower power consumption in datacenters.

Semiconductor devices require highly efficient electrical connections to drive and collect the current in the M-S junction without thermal losses by Joule heating, *i.e.,* ohmic contacts with ultra-low contact resistance ρ_c. The fabrication of n-type Ge- and GeSn-based ohmic contacts is especially difficult due to the fermi-level pinning near the valence band edge. To circumvent this issue, the doping level in the semiconductor side needs to be very high, and the SBH needs to be minimized. We have also shown that M-S alloyed junctions will remain the optimal and most flexible solution to further mitigate the FLP problem, and thereby regain control over the SBH to effectively lower its values. Moreover, the aforementioned optimizations also extend to p-type Ge- and GeSn-based ohmic contacts. The work realized in this thesis targeted all of these aspects. We also took into consideration the decreased thermal stability of GeSn at higher Sn contents in our processes' development to avoid compromising the electrical properties of the contacts with the optical performance of devices during processing.

For the first experimental part, we focused on investigating the potential of implementing laser thermal annealing as a low thermal budget processing solution for the functionalization of Ni-based ohmic contacts on GeSn, without damaging the GeSn heterostructure underneath. For this matter,

we systematically studied the effect of laser thermal annealing on the properties of CVD-grown GeSn samples with Sn-content up to 11.2 at.%, and on the performance of Ni-based contacts on these specimens. The laser energy density was varied to span multiple interaction modes with GeSn. We also discussed the effect of varying the energy density and Sn composition on the morphological and compositional changes of GeSn upon annealing. We found that for laser annealed uncontacted GeSn layers, certain energy densities trigger Sn diffusion towards the surface, to form Sn-rich GeSn nanoislands, and this behavior is more noted for samples with higher Sn-contents. However, Sn diffusion was restricted to only the first layer in the heterostructure, while the underlying layers remained in their as-grown condition, despite processing the samples at a very high total time of 120 ns and pulses number of 20. For the $Ge_{0.888}Sn_{0.112}$ sample, TEM data revealed the origin of Sn-rich dome shaped regions at the surface as the Sn-rich lines that form at 150 nm in depth. The origin of this behavior was discussed, and further comprehensive studies need to be conducted for a conclusive judgement on the underlying mechanism. However, these understandings can significantly help in optimizing the annealing conditions to lower the density of these laser-induced defects, and thereby lowering the overall laser-induced damage. As for laser annealed Ni-based contacts on GeSn, the contact resistance ρ_c was notably improved after LTA. This was attributed to forming a stanogermanide layer, which was also apparent in the TEM data on Ni/$Ge_{0.888}Sn_{0.112}$ after ED4. However, for these contacts, and despite achieving a metastable $Ni(Ge_{0.888}Sn_{0.112})_2$ layer at ED4, the specific contact resistance of the latter was not improved. This was attributed to the formation of a damaged layer at the interface that blocked the current flow. Overall, this phase's formation for high Sn-content GeSn is promising, and further studies targeting the optimization of processing conditions can significantly improve the contact properties on this materials system using this phase.

In the second part, we concentrated on understanding the doping process of relaxed and high Sn-content GeSn. Thus, we systematically investigated *in situ* doping during the growth of partially relaxed GeSn at 9 at.% Sn. We used arsenic and boron as the dopant elements, for n-type and p-type doping, respectively. The active carrier concentrations achieved are in the 10^{20} cm^{-3} and 10^{17}-10^{19} cm^{-3} ranges, for GeSn:As and GeSn:B layers, respectively. The calculated activation rate is also high in most of the studied samples. We also note that incorporating As and B in GeSn at these doping levels did not reduce the crystalline quality of the doped layers, nor induce the formation of additional threading dislocations. Thus, the surface topography of these layers remained similar

to undoped references. On the other hand, the Sn content was indeed affected by B and As incorporation. Higher As levels led to an increase in the Sn content in As-doped GeSn. Conversely, higher B concentrations led to a decrease in the Sn content. Thus, for future optoelectronic devices operating in the MIR range, *i.e.* using GeSn with high Sn concentrations, the development of processes that target highly doped and relaxed GeSn:As are intrinsically more manageable than GeSn:B as a result of the abovementioned interactions.

6.2 Perspectives for future work

In this thesis, we have developed *in situ* growth methods for highly doped GeSn layers, and low thermal budget processing for the fabrication of Ni-based alloys with GeSn. Both are needed in highly performing ohmic contacts on high Sn-content GeSn for future electronic and optoelectronic GeSn-based devices.

For the *in situ* doping process, we have demonstrated high active doping levels of 1.5×10^{20} cm^{-3} and 1.1×10^{19} cm^{-3} ranges, for n-type and p-type GeSn, respectively. For n-type doping in GeSn, this active doping level is high enough to reach field emission for current transport in M-GeSn junctions, and thereby circumvent issues related to FLP. Hence, these layers can be used directly as substrates for further M-GeSn processing to achieve ultra-low contact resistance in these junctions. For p-type doping, the growth can be further optimized to achieve higher active doping levels in the 10^{20} cm^{-3} range, and thereby reach FE for current transport in these devices. Our results show the higher likelihood of achieving these values on strain-relaxed GeSn relative to pseudomorphic GeSn. However, one alternative to this method is to intentionally lower the Sn-content of the layer intended for the ohmic contact, which allows for higher accommodation of B atoms in substitutional sites, and thereby achieve doping levels in the 10^{20} cm^{-3} range. In our case, we can use our RPCVD-grown Ge:B hyper-doped layers, which were developed during the optimization of doped GeSn growth. Finally, although the FLP acts as an advantage for ohmic contacts on p-type GeSn, further thermal processing of the junctions is needed for ultra-low contact resistance in both GeSn:B and GeSn:As layers. Thus, an LTA study on pristine as-grown doped GeSn can reveal if this annealing method is compatible with these samples, or that the dopant profiles cannot be preserved during annealing. On another note, we have shown that the active incorporation of As and B in GeSn influences the Sn-content in doped layers. Thus, for layouts such as p-i-n junctions, we point out that targeting flat Sn profiles throughout the doped and

undoped regions can be well-controlled by tuning the growth temperature and $SnCl_4$ flow rate to balance the Sn profile.

Regarding LTA processing of M-GeSn junctions for ohmic contacts, we have shown that it is possible to form a high-quality nickel alloy with GeSn, *i.e.,* $Ni(Ge_{0.888}Sn_{0.112})_2$, after LTA annealing the Ni/$Ge_{0.888}Sn_{0.112}$ at ED4, despite that it does not directly contact the $Ge_{0.888}Sn_{0.112}$ layer. We also mentioned that alloying Ni with GeSn requires a threshold ED below-which the alloy cannot be formed. For conventional annealing techniques on GeSn samples with higher Sn-content, these alloys require a higher processing temperature to form [99]. Hence, a similar increase in the threshold ED is expected. As the ED range for process optimization of this system becomes narrower for higher Sn-contents, the optimization process will be mainly restricted to the pulse duration and number. As we established earlier, in our LTA study, the total pulse duration was intentionally high to ensure a proper substrate reaction that can be studied and attributed to certain mechanisms. This also applies to the total pulses' number of 20. The latter is not advantageous compared with a single pulse since the quenching process takes 100s of ns, accumulating for higher pulses' numbers. Thus, there is a big room for LTA process optimization for the functionalization of M-GeSn junctions. However, it is still unclear if this optimization will reduce the formation of Ni-rich funnel-like shapes, and thereby lower the contact resistance. Thus, it is highly important to continue the systematic study of LTA on pure GeSn to find the origin of the Sn-rich lines, thereby designing LTA processes that lower their concentration or interference during Ni-GeSn alloy formation. For that matter, if cellular breakdown is indeed demonstrated to be the dominant mechanism for the formation of Sn-rich features in the LTA-affected region, careful considerations on the LTA parameters have to be taken to suppress this breakdown. We note that FLA treatments can also be suitable in this case, as they were shown to suppress cellular breakdown of Si supersaturated with Ti, [153, 199] and were recently employed to fabricate 4.5 at.% Sn GeSn layers [200]. Finally, after this optimization, one important objective would be studying the LTA effect on Ni alloys' formation with n- and p-type doped GeSn. Effects such as dopant segregation during LTA processing can further enhance the contacts' electrical properties, [54, 55] and this aspect is particularly interesting to investigate for contact engineering. These contacts have great importance in optimizing SWIR/MIR GeSn-based OE devices' performance, such as by increasing the external quantum efficiency of LEDs and lowering Joule heating effects of electrically pumped lasers.

REFERENCES

1. Geiger, R., T. Zabel, and H. Sigg, *Group IV Direct Band Gap Photonics: Methods, Challenges, and Opportunities.* Frontiers in Materials, 2015. **2**(52).
2. Attiaoui, A. and O. Moutanabbir, *Indirect-to-direct band gap transition in relaxed and strained Ge1−x−ySixSnyternary alloys.* Journal of Applied Physics, 2014. **116**(6).
3. Assali, S., J. Nicolas, and O. Moutanabbir, *Enhanced Sn incorporation in GeSn epitaxial semiconductors via strain relaxation.* Journal of Applied Physics, 2019. **125**(2).
4. Zaima, S., et al., *Growth and applications of GeSn-related group-IV semiconductor materials.* Science and Technology of Advanced Materials, 2015. **16**(4): p. 043502.
5. Atalla, M.R.M., et al., *All-Group IV membrane room-temperature mid-infrared photodetector.* physics.app-ph, 2020.
6. Tran, H., et al., *Si-Based GeSn Photodetectors toward Mid-Infrared Imaging Applications.* ACS Photonics, 2019. **6**(11): p. 2807-2815.
7. Zhou, Y., et al., *Optically Pumped GeSn Lasers Operating at 270 K with Broad Waveguide Structures on Si.* ACS Photonics, 2019. **6**(6): p. 1434-1441.
8. Chrétien, J., et al., *GeSn Lasers Covering a Wide Wavelength Range Thanks to Uniaxial Tensile Strain.* ACS Photonics, 2019. **6**(10): p. 2462-2469.
9. Zhou, Y., et al., *Electrically injected GeSn lasers on Si operating up to 100 K.* Optica, 2020. **7**(8).
10. Soref, R., D. Buca, and S.-Q. Yu, *Group IV Photonics: Driving Integrated Optoelectronics.* Optics and Photonics News, 2016. **27**(1): p. 32-39.
11. Soref, R., *Mid-infrared photonics in silicon and germanium.* Nature Photonics, 2010. **4**(8): p. 495-497.
12. Saito, S., et al., *Towards monolithic integration of germanium light sources on silicon chips.* Semiconductor Science and Technology, 2016. **31**(4): p. 043002.
13. Radamson, H.H. and E. Simeon, *5 - Channel materials*, in *CMOS Past, Present and Future*, H.H. Radamson, et al., Editors. 2018, Woodhead Publishing. p. 105-124.
14. *INTERNATIONAL ROADMAP FOR DEVICES AND SYSTEMS.* IEEE, 2017.
15. Radamson, H.H., et al., *2 - Scaling and evolution of device architecture*, in *CMOS Past, Present and Future*, H.H. Radamson, et al., Editors. 2018, Woodhead Publishing. p. 19-40.
16. Rhoderick, E.H., *Metal-semiconductor contacts.* IEE Proceedings I - Solid-State and Electron Devices, 1982. **129**(1): p. 1.
17. Schroder, D.K., *Semiconductor Material and Device Characterization*. 2005.
18. Nishimura, T., K. Kita, and A. Toriumi, *Evidence for strong Fermi-level pinning due to metal-induced gap states at metal/germanium interface.* Applied Physics Letters, 2007. **91**(12).

19. Galluccio, E., et al., *Formation and characterization of Ni, Pt, and Ti stanogermanide contacts on Ge0.92Sn0.08.* Thin Solid Films, 2019. **690**: p. 137568.

20. Goodman, C.H.L., *Direct-gap group IV semiconductors based on tin.* IEE Proceedings I - Solid-State and Electron Devices, 1982. **129**(5): p. 189-192.

21. Doherty, J., et al., *Progress on Germanium–Tin Nanoscale Alloys.* Chemistry of Materials, 2020.

22. Olesinski, R.W. and G.J. Abbaschian, *The Ge−Sn (Germanium−Tin) system.* Bulletin of Alloy Phase Diagrams, 1984. **5**(3): p. 265-271.

23. Oguz, S., et al., *Synthesis of metastable, semiconducting Ge-Sn alloys by pulsed UV laser crystallization.* Applied Physics Letters, 1983. **43**(9): p. 848-850.

24. Bauer, M.R., et al., *Tunable band structure in diamond–cubic tin–germanium alloys grown on silicon substrates.* Solid State Communications, 2003. **127**(5): p. 355-359.

25. Gupta, S., et al., *Achieving direct band gap in germanium through integration of Sn alloying and external strain.* Journal of Applied Physics, 2013. **113**(7): p. 073707.

26. Richard D'Costa, V., et al., *Above-bandgap optical properties of biaxially strained GeSn alloys grown by molecular beam epitaxy.* Applied Physics Letters, 2014. **104**(2): p. 022111.

27. Polak, M.P., P. Scharoch, and R. Kudrawiec, *The electronic band structure of Ge1−xSnxin the full composition range: indirect, direct, and inverted gaps regimes, band offsets, and the Burstein–Moss effect.* Journal of Physics D: Applied Physics, 2017. **50**(19).

28. Nicolas, J., et al., *Dislocation Pipe Diffusion and Solute Segregation during the Growth of Metastable GeSn.* Crystal Growth & Design, 2020. **20**(5): p. 3493-3498.

29. Pukite, P.R., A. Harwit, and S.S. Iyer, *Molecular beam epitaxy of metastable, diamond structure SnxGe1−x alloys.* Applied Physics Letters, 1989. **54**(21): p. 2142-2144.

30. Margetis, J., et al., *Fundamentals of Ge 1−x Sn x and Si y Ge 1−x-y Sn x RPCVD epitaxy.* Materials Science in Semiconductor Processing, 2017. **70**: p. 38-43.

31. Dou, W., et al., *Investigation of GeSn Strain Relaxation and Spontaneous Composition Gradient for Low-Defect and High-Sn Alloy Growth.* Sci Rep, 2018. **8**(1): p. 5640.

32. Assali, S., et al., *Atomically uniform Sn-rich GeSn semiconductors with 3.0–3.5 μm room-temperature optical emission.* Applied Physics Letters, 2018. **112**(25).

33. Ye, H. and J. Yu, *Germanium epitaxy on silicon.* Sci Technol Adv Mater, 2014. **15**(2): p. 024601.

34. Hartmann, J.M., et al., *Impact of the H2 anneal on the structural and optical properties of thin and thick Ge layers on Si; Low temperature surface passivation of Ge by Si.* Journal of Crystal Growth, 2010. **312**(4): p. 532-541.

35. Littlejohns, C.G., et al., *Ge-on-Si Plasma-Enhanced Chemical Vapor Deposition for Low-Cost Photodetectors.* IEEE Photonics Journal, 2015. **7**(4): p. 1-8.

36. Aubin, J., et al., *Impact of thickness on the structural properties of high tin content GeSn layers.* Journal of Crystal Growth, 2017. **473**: p. 20-27.

37. Aubin, J., et al., *Growth and structural properties of step-graded, high Sn content GeSn layers on Ge.* Semiconductor Science and Technology, 2017. **32**(9): p. 094006.

38. von den Driesch, N., et al., *Thermally activated diffusion and lattice relaxation in (Si)GeSn materials.* Physical Review Materials, 2020. **4**(3): p. 033604.

39. Zaumseil, P., et al., *The thermal stability of epitaxial GeSn layers.* APL Materials, 2018. **6**(7).

40. Groiss, H., et al., *Free-running Sn precipitates: an efficient phase separation mechanism for metastable Ge1−xSnx epilayers.* Scientific Reports, 2017. **7**(1): p. 16114.

41. Gaudet, S., et al., *Thin film reaction of transition metals with germanium.* Journal of Vacuum Science & Technology A: Vacuum, Surfaces, and Films, 2006. **24**(3): p. 474-485.

42. Lee, Y.-J., et al., *Dopant Activation in Single-Crystalline Germanium by Low-Temperature Microwave Annealing.* IEEE Electron Device Letters, 2011. **32**(2): p. 194-196.

43. Niinistö, J., et al., *Controlled growth of HfO2 thin films by atomic layer deposition from cyclopentadienyl-type precursor and water.* Journal of Materials Chemistry, 2005. **15**(23).

44. *The theory of crystal rectifiers.* Proceedings of the Royal Society of London. Series A. Mathematical and Physical Sciences, 1997. **171**(944): p. 27-38.

45. Schottky, W., *Zur Halbleitertheorie der Sperrschicht- und Spitzengleichrichter.* Zeitschrift fr Physik, 1939. **113**(5-6): p. 367-414.

46. Sze, S.M. and K.K. Ng, *Physics of Semiconductor Devices*. 2006.

47. Hutin, L., et al., *Schottky Barrier Height Extraction in Ohmic Regime: Contacts on Fully-Processed 200mm GeOI Substrates*, in *ECS Transactions*. 2008, ECS.

48. Wang, S.H., et al., *Design of a shallow thermally stable ohmic contact to p-type InGaSb.* Journal of Vacuum Science & Technology B: Microelectronics and Nanometer Structures, 2003. **21**(2).

49. Firrincieli, A., et al., *Study of the impact of doping concentration and Schottky barrier height on ohmic contacts to n-type germanium.* Microelectronic Engineering, 2013. **106**: p. 129-131.

50. Jeon, J., et al., *Formation of ultra-low resistance contact with nickel stanogermanide/heavily doped n +-Ge1−x Sn x structure.* Semiconductor Science and Technology, 2018. **33**(12).

51. Landauer, R., *Spatial Variation of Currents and Fields Due to Localized Scatterers in Metallic Conduction.* IBM Journal of Research and Development, 1957. **1**(3): p. 223-231.

52. Wu, Y., et al., *Sub- 10−9Ω·cm2 Specific Contact Resistivity (Down to 4.4×10−10Ω·cm2) for Metal Contact on Ga and Sn Surface-Segregated GeSn Film.* IEEE Transactions on Electron Devices, 2018. **65**(12): p. 5275-5281.

53. Wu, Y., et al. *Metal/P-type GeSn Contacts with Specific Contact Resistivity down to 4.4×10−10 Ω-cm2*. in *2018 IEEE Symposium on VLSI Technology*. 2018.

54. Ikeda, K., et al., *Modulation of NiGe/Ge Schottky barrier height by sulfur segregation during Ni germanidation.* Applied Physics Letters, 2006. **88**(15).

55. Schulte-Braucks, C., et al., *Schottky barrier tuning via dopant segregation in NiGeSn-GeSn contacts.* Journal of Applied Physics, 2017. **121**(20).

56. Miyoshi, H., et al. *In-situ contact formation for ultra-low contact resistance NiGe using carrier activation enhancement (CAE) techniques for Ge CMOS*. in *2014 Symposium on VLSI Technology (VLSI-Technology): Digest of Technical Papers*. 2014.

57. Bardeen, J., *Surface States and Rectification at a Metal Semi-Conductor Contact.* Physical Review, 1947. **71**(10): p. 717-727.

58. Mead, C.A. and W.G. Spitzer, *Fermi Level Position at Metal-Semiconductor Interfaces.* Physical Review, 1964. **134**(3A): p. A713-A716.

59. *The physics and chemistry of the Schottky barrier height.* Applied Physics Reviews, 2014. **1**(1).

60. Dimoulas, A., et al., *Fermi-level pinning and charge neutrality level in germanium.* Applied Physics Letters, 2006. **89**(25).

61. Tung, R.T., *Formation of an electric dipole at metal-semiconductor interfaces.* Physical Review B, 2001. **64**(20).

62. Mönch, W., *Barrier heights of real Schottky contacts explained by metal-induced gap states and lateral inhomogeneities.* Journal of Vacuum Science & Technology B: Microelectronics and Nanometer Structures, 1999. **17**(4).

63. Nishimura, T., et al., *Almost pinning-free bismuth/Ge and /Si interfaces.* AIP Advances, 2019. **9**(9).

64. Luo, X., et al., *Understanding of Fermi level pinning at metal/germanium interface based on semiconductor structure.* Applied Physics Express, 2020. **13**(3): p. 031003.

65. Nishimura, T., T. Yajima, and A. Toriumi, *Reexamination of Fermi level pinning for controlling Schottky barrier height at metal/Ge interface.* Applied Physics Express, 2016. **9**(8).

66. Kuzmin, M., et al., *Origin of Fermi-level pinning and its control on the n-type Ge(100) surface.* Physical Review B, 2016. **94**(3): p. 035421.

67. Li, H., Y. Guo, and J. Robertson, *Face Dependence of Schottky Barriers Heights of Silicides and Germanides on Si and Ge.* Sci Rep, 2017. **7**(1): p. 16669.

68. Jheng, L.S., et al., *Comparative investigation of Schottky barrier height of Ni/n-type Ge and Ni/n-type GeSn.* AIP Advances, 2017. **7**(9).

69. Yung-Hsien, W., et al. *Formation of solid phase epitaxial GeSn and its application to high-performance N-MOSFETs and low-resistivity contact*. in *2016 13th IEEE International Conference on Solid-State and Integrated Circuit Technology (ICSICT)*. 2016.

70. Zhang, S.-L. and M. Östling, *Metal Silicides in CMOS Technology: Past, Present, and Future Trends.* Critical Reviews in Solid State and Materials Sciences, 2003. **28**(1): p. 1-129.

71. Lin, L., Y. Guo, and J. Robertson, *Metal silicide Schottky barriers on Si and Ge show weaker Fermi level pinning.* Applied Physics Letters, 2012. **101**(5).

72. Michaelson, H.B., *The work function of the elements and its periodicity.* Journal of Applied Physics, 1977. **48**(11): p. 4729-4733.

73. Spann, J.Y., et al., *Characterization of nickel Germanide thin films for use as contacts to p-channel Germanium MOSFETs.* IEEE Electron Device Letters, 2005. **26**(3): p. 151-153.

74. Zhang, Q., et al., *Formation and Thermal Stability of Nickel Germanide on Germanium Substrate.* Japanese Journal of Applied Physics, 2005. **44**(No. 45): p. L1389-L1391.

75. Gaudet, S., et al., *Reaction of thin Ni films with Ge: Phase formation and texture.* Journal of Applied Physics, 2006. **100**(3): p. 034306.

76. Li, H., et al., *Electrical characteristics of Ni Ohmic contact on n-type GeSn.* Applied Physics Letters, 2014. **104**(24).

77. Demeulemeester, J., et al., *Sn diffusion during Ni germanide growth on Ge1–xSnx.* Applied Physics Letters, 2011. **99**(21): p. 211905.

78. Wang, C., et al., *Improved performance of Ge n + /p diode by combining laser annealing and epitaxial Si passivation.* Chinese Physics B, 2018. **27**(1): p. 018502.

79. Suzuki, A., et al., *Alleviation of Fermi level pinning at metal/n-Ge interface with lattice-matched Si x Ge1− x − y Sn y ternary alloy interlayer on Ge.* Japanese Journal of Applied Physics, 2018. **57**(6).

80. Suzuki, A., et al., *Growth of ultrahigh-Sn-content Ge1−xSnxepitaxial layer and its impact on controlling Schottky barrier height of metal/Ge contact.* Japanese Journal of Applied Physics, 2016. **55**(4S).

81. Suzuki, A., et al., *Reduction of Schottky barrier height for n-type Ge contact by using Sn electrode.* Japanese Journal of Applied Physics, 2014. **53**(4S).

82. Kumari, P. and V.R. Rao, *Fermi-Level Depinning in Germanium Using Black Phosphorus as an Interfacial Layer.* IEEE Electron Device Letters, 2019. **40**(10): p. 1678-1681.

83. Baek, S.-h.C., et al., *Alleviation of fermi-level pinning effect at metal/germanium interface by the insertion of graphene layers.* Applied Physics Letters, 2014. **105**(7).

84. Chen, K., et al., *Formation of Ohmic Contact With Low Contact Resistance on n-GeSn by Fermi Level Depinning Using Plasma Treatment.* IEEE Electron Device Letters, 2016. **37**(7): p. 827-830.

85. Janardhanam, V., et al., *Fermi-level depinning in germanium Schottky junction using nitrogen plasma treatment.* Electronics Letters, 2018. **54**(14): p. 897-899.

86. Roy, A.M., J.Y.J. Lin, and K.C. Saraswat, *Specific Contact Resistivity of Tunnel Barrier Contacts Used for Fermi Level Depinning.* IEEE Electron Device Letters, 2010. **31**(10): p. 1077-1079.

87. Kim, J., et al., *Universal Metal–Interlayer–Semiconductor Contact Modeling Considering Interface-State Effect on Contact Resistivity Degradation.* IEEE Transactions on Electron Devices, 2018. **65**(11): p. 4982-4987.

88. Lieten, R.R., et al., *Mechanisms of Schottky Barrier Control on n-Type Germanium Using Ge3N4 Interlayers.* Journal of The Electrochemical Society, 2011. **158**(4): p. H358.

89. Kim, G.-S., et al., *Schottky barrier height modulation of metal–interlayer–semiconductor structure depending on contact surface orientation for multi-gate transistors.* Applied Physics Letters, 2019. **114**(1).

90. Lin, J.Y.J., et al., *Increase in current density for metal contacts to n-germanium by inserting TiO2 interfacial layer to reduce Schottky barrier height.* Applied Physics Letters, 2011. **98**(9).

91. Kim, G.-S., et al., *Fermi-Level Unpinning Technique with Excellent Thermal Stability for n-Type Germanium.* ACS Applied Materials & Interfaces, 2017. **9**(41): p. 35988-35997.

92. Manik, P.P. and S. Lodha, *Contacts on n-type germanium using variably doped zinc oxide and highly doped indium tin oxide interfacial layers.* Applied Physics Express, 2015. **8**(5): p. 051302.

93. Kim, G.S., et al., *Formation of Low-Resistivity Metal/Germanium Contact with Ultra-Thin Interlayer and Plasma Oxidation for n-Channel Germanium FET.* ECS Transactions, 2016. **72**(4): p. 127-129.

94. Kim, J., et al., *Analytical Study of Interfacial Layer Doping Effect on Contact Resistivity in Metal-Interfacial Layer-Ge Structure.* IEEE Electron Device Letters, 2014. **35**(7): p. 705-707.

95. Yu, H., et al. *MIS or MS? Source/drain contact scheme evaluation for 7nm Si CMOS technology and beyond*. in *2016 16th International Workshop on Junction Technology (IWJT)*. 2016.

96. Wu, Y., D. Lei, and X. Gong, *Theoretical investigation of metal/n-Ge1−xSnx (0 ≤ x < 0.11) contacts using transfer matrix method.* Journal of Applied Physics, 2019. **125**(10): p. 105102.

97. Yang, Y., et al., *Germanium-tin n-channel tunneling field-effect transistor: Device physics and simulation study.* Journal of Applied Physics, 2013. **113**(19).

98. Schaekers, M., et al., *Contact resistivities of metal-insulator-semiconductor contacts and metal-semiconductor contacts.* Applied Physics Letters, 2016. **108**(17).

99. Quintero, A., et al., *Impact of Sn content in Ge1−xSnx layers on Ni-stanogermanides solid-state reaction and properties*, in *2018 IEEE International Interconnect Technology Conference (IITC)*. 2018. p. 103-105.

100. Nishimura, T., et al., *Formation of Ni(Ge1−xSnx) layers with solid-phase reaction in Ni/Ge1−xSnx/Ge systems.* Solid-State Electronics, 2011. **60**(1): p. 46-52.

101. Henini, M., *Handbook of Semiconductor Manufacturing Technology: Y. Nishi, R. Doering (Eds.); Marcel Dekker, New York, ISBN 0-8247-8783-8.* Microelectronics Journal, 2001. **32**(2): p. 180.

102. Margetis, J., et al., *Strain engineering in epitaxial Ge1−xSnx: a path towards low-defect and high Sn-content layers.* Semiconductor Science and Technology, 2017. **32**(12): p. 124006.

103. Madou, M.J., *Fundamentals of Microfabrication and Nanotechnology, Three-Volume Set*. 2018.

104. Sun, S., et al., *Surface termination and roughness of Ge(100) cleaned by HF and HCl solutions.* Applied Physics Letters, 2006. **88**(2).

105. Mahjoub, M.A., et al., *Impact of Wet Treatments on the Electrical Performance of Ge0.9Sn0.1-Based p-MOS Capacitors.* ACS Applied Electronic Materials, 2019. **1**(2): p. 260-268.

106. Segmüller, A., I.C. Noyan, and V.S. Speriosu, *X-ray diffraction studies of thin films and multilayer structures.* Progress in Crystal Growth and Characterization, 1989. **18**: p. 21-66.

107. Fewster, P.F., *X-Ray Scattering from Semiconductors*. 2003.

108. Xu, C., et al., *Deviations from Vegard's law in semiconductor thin films measured with X-ray diffraction and Rutherford backscattering: The Ge1-ySny and Ge1-xSix cases.* Journal of Applied Physics, 2017. **122**(12).

109. G, S.B. and S. Banerjee, *Solid State Electronic Devices*. 6th ed. 2006.

110. Wirths, S., et al., *High-k gate stacks on low bandgap tensile strained Ge and GeSn alloys for field-effect transistors.* ACS Appl Mater Interfaces, 2015. **7**(1): p. 62-7.

111. Frank, D.J., et al., *Device scaling limits of Si MOSFETs and their application dependencies.* Proceedings of the IEEE, 2001. **89**(3): p. 259-288.

112. Schulte-Braucks, C., et al., *Correlation of Bandgap Reduction with Inversion Response in (Si)GeSn/High-k/Metal Stacks.* ACS Appl Mater Interfaces, 2017. **9**(10): p. 9102-9109.

113. Nicollian, E.H. and J.R. Brews, *MOS (Metal Oxide Semiconductor) Physics and Technology*. 2002: Wiley.

114. Kasap, S. and P. Capper, *Springer Handbook of Electronic and Photonic Materials; Single-Crystal Silicon: Electrical and Optical Properties*. 2017.

115. Schulte-Braucks, C., et al., *Low Temperature Deposition of High-k/Metal Gate Stacks on High-Sn Content (Si)GeSn-Alloys.* ACS Appl Mater Interfaces, 2016. **8**(20): p. 13133-9.

116. Reeves, G.K. and H.B. Harrison, *Obtaining the specific contact resistance from transmission line model measurements.* IEEE Electron Device Letters, 1982. **3**(5): p. 111-113.

117. Reeves, G.K., *Specific contact resistance using a circular transmission line model.* Solid-State Electronics, 1980. **23**(5): p. 487-490.

118. Marlow, G.S. and M.B. Das, *The effects of contact size and non-zero metal resistance on the determination of specific contact resistance.* Solid-State Electronics, 1982. **25**(2): p. 91-94.

119. Hao, Y., et al., *A Simplified Method for (Circular) Transmission Line Model Simulation and Ultralow Contact Resistivity Extraction.* IEEE Electron Device Letters, 2014. **35**(9): p. 957-959.

120. Wu, Y., et al., *Elimination of the Parasitic Metal Resistance in Transmission Line Model for Extraction of Ultralow Specific Contact Resistivity.* IEEE Transactions on Electron Devices, 2019. **66**(7): p. 3086-3092.

121. Yu, H., et al., *Process options to enable (sub-)1e-9 Ohm.cm2 contact resistivity on Si devices*, in *2016 IEEE International Interconnect Technology Conference / Advanced Metallization Conference (IITC/AMC)*. 2016. p. 66-68.

122. Stavitski, N., et al., *Systematic TLM Measurements of NiSi and PtSi Specific Contact Resistance to n- and p-Type Si in a Broad Doping Range.* IEEE Electron Device Letters, 2008. **29**(4): p. 378-381.

123. Park, J.Y., J. Cho, and S.C. Jun, *Review of contact-resistance analysis in nano-material.* Journal of Mechanical Science and Technology, 2018. **32**(2): p. 539-547.

124. Wu, Y., et al., *A Novel Fast-Turn-Around Ladder TLM Methodology with Parasitic Metal Resistance Elimination, and 2×10−10 Ω-cm2Resolution: Theoretical Design and Experimental Demonstration*, in *2019 Symposium on VLSI Technology*. 2019. p. T150-T151.

125. Wu, Y., et al., *An Improved Methodology for Accurate Extraction of Ultra-Low Specific Contact Resistivity of Alloyed Contacts Using Nanoscale Transmission Line Method.* IEEE Electron Device Letters, 2018. **39**(6): p. 803-806.

126. Williams, D.B. and C.B. Carter, *Transmission Electron Microscopy*. 2009.

127. *Secondary Ion Mass Spectrometry—a Practical Handbook for Depth Profiling and Bulk Impurity Analysis* New York: Wiley.

128. Py, M., *Study of interfaces and nanometric structures by ToF-SIMS : upon a spatially resolved quantitative analysis*, in *Micro and nanotechnologies/Microelectronics*. 2011: Université de Grenoble. p. 277.

129. Wirtz, T., et al., *High-resolution high-sensitivity elemental imaging by secondary ion mass spectrometry: from traditional 2D and 3D imaging to correlative microscopy.* Nanotechnology, 2015. **26**(43): p. 434001.

130. Zhong, J. and J. Yan, *Seeing is believing: atomic force microscopy imaging for nanomaterial research.* RSC Advances, 2016. **6**(2): p. 1103-1121.

131. Crossley, A., et al., *A study comparing measurements of roughness of silicon and SiO2 surfaces and interfaces using scanning probe microscopy and neutron reflectivity.* Journal of Non-Crystalline Solids, 1995. **187**: p. 221-226.

132. Fournier-Lupien, J.-H., *Les alliages germanium-étain et silicium-germanium-étain: croissance, propriétés structurales et stabilité thermique*, in *Department of physics*. 2015, École Polytechnique de Montréal.

133. Huet, K., et al., *Laser Thermal Annealing: A low thermal budget solution for advanced structures and new materials*, in *2014 International Workshop on Junction Technology (IWJT)*. 2014, IEEE: Shanghai. p. 1-6.

134. Lombardo, S.F., et al., *Laser annealing in Si and Ge: Anomalous physical aspects and modeling approaches.* Materials Science in Semiconductor Processing, 2017. **62**: p. 80-91.

135. Kim, D.H., et al., *Electrical properties and structure of laser-spike-annealed hafnium oxide.* Thin Solid Films, 2010. **518**(10): p. 2812-2815.

136. Frigerio, J., et al., *Optical properties of highly n-doped germanium obtained byin situdoping and laser annealing.* Journal of Physics D: Applied Physics, 2017. **50**(46).

137. Shayesteh, M., et al., *Optimized Laser Thermal Annealing on Germanium for High Dopant Activation and Low Leakage Current.* IEEE Transactions on Electron Devices, 2014. **61**(12): p. 4047-4055.

138. Shi Ya Lim, P., et al., *Fermi-level depinning at the metal-germanium interface by the formation of epitaxial nickel digermanide NiGe2 using pulsed laser anneal.* Applied Physics Letters, 2012. **101**(17).

139. Lim, P.S.Y., et al., *Formation of epitaxial metastable NiGe2 thin film on Ge(100) by pulsed excimer laser anneal.* Applied Physics Letters, 2010. **97**(18).

140. Firrincieli, A., et al., *Study of ohmic contacts to n-type Ge: Snowplow and laser activation.* Applied Physics Letters, 2011. **99**(24).

141. Wang, L., et al., *Post-growth annealing of germanium-tin alloys using pulsed excimer laser.* Journal of Applied Physics, 2015. **118**(2).

142. Medvid, A., *Redistribution of Point Defects in the Crystalline Lattice of a Semiconductor in an Inhomogeneous Temperature Field.* Defect and Diffusion Forum, 2002. **210-212**: p. 89-102.

143. Shayesteh, M., et al., *Atomically Flat Low-Resistive Germanide Contacts Formed by Laser Thermal Anneal.* IEEE Transactions on Electron Devices, 2013. **60**(7): p. 2178-2185.

144. Kim, T., et al., *Heat flow model for pulsed laser melting and rapid solidification of ion implanted GaAs.* Journal of Applied Physics, 2010. **108**(1).

145. Tran, T.T., et al., *Synthesis of Ge1−xSnx alloys by ion implantation and pulsed laser melting: Towards a group IV direct bandgap material.* Journal of Applied Physics, 2016. **119**(18).

146. Gao, K., et al., *Ge1−xSnx alloys synthesized by ion implantation and pulsed laser melting.* Applied Physics Letters, 2014. **105**(4).

147. Onufrijevs, P., et al., *Direct-indirect GeSn band structure formation by laser Radiation: The enhancement of Sn solubility in Ge.* Optics & Laser Technology, 2020. **128**.

148. Freitas, F.L., et al., *Influence of the composition fluctuations and decomposition on the tunable direct gap and oscillator strength of Ge1-xSnx alloys.* Applied Physics Letters, 2016. **108**(9).

149. Warrender, J.M., *Laser hyperdoping silicon for enhanced infrared optoelectronic properties.* Applied Physics Reviews, 2016. **3**(3).

150. Azrak, E., et al., *Growth of In-Plane Ge1–xSnx Nanowires with 22 at. % Sn Using a Solid–Liquid–Solid Mechanism.* The Journal of Physical Chemistry C, 2018. **122**(45): p. 26236-26242.

151. Reitano, R., P.M. Smith, and M.J. Aziz, *Solute trapping of group III, IV, and V elements in silicon by an aperiodic stepwise growth mechanism.* Journal of Applied Physics, 1994. **76**(3): p. 1518-1529.

152. Aziz, M.J. and T. Kaplan, *Continuous growth model for interface motion during alloy solidification.* Acta Metallurgica, 1988. **36**(8): p. 2335-2347.

153. Rebohle, L., S. Prucnal, and W. Skorupa, *A review of thermal processing in the subsecond range: semiconductors and beyond.* Semiconductor Science and Technology, 2016. **31**(10): p. 103001.

154. Recht, D., et al., *Supersaturating silicon with transition metals by ion implantation and pulsed laser melting.* Journal of Applied Physics, 2013. **114**(12).

155. Bhatia, A., et al., *Synthesis of Ge1−xSnxAlloy Thin Films Using Ion Implantation and Pulsed Laser Melting (II-PLM).* Journal of Electronic Materials, 2012. **41**(5): p. 837-844.

156. Chekhovskoi, V.Y. and V.E. Peletskii, *Nonequilibrium metal melting during rapid heating.* Russian Metallurgy (Metally), 2008. **2008**(5): p. 377-385.

157. Tran, T.T., et al., *Ion beam synthesis and photoluminescence study of supersaturated fully-relaxed Ge-Sn alloys.* Materials Science and Engineering: B, 2020. **262**.

158. Takeuchi, W., et al., *Characterization of Shallow- and Deep-Level Defects in Undoped Ge1−xSnxEpitaxial Layers by Electrical Measurements.* ECS Journal of Solid State Science and Technology, 2015. **5**(4): p. P3082-P3086.

159. Slotte, J., et al., *(Invited) Positron Annihilation Spectroscopy on Open-Volume Defects in Group IV Semiconductors.* ECS Transactions, 2014. **64**(11): p. 241-253.

160. Noroozi, M., et al., *Effect of strain on Ni-(GeSn)x contact formation to GeSn nanowires.* MRS Proceedings, 2014. **1707**.

161. Garbrecht, M., et al., *Dislocation-pipe diffusion in nitride superlattices observed in direct atomic resolution.* Sci Rep, 2017. **7**: p. 46092.

162. Trumbore, F.A., *Solid Solubilities of Impurity Elements in Germanium and Silicon*.* Bell System Technical Journal, 1960. **39**(1): p. 205-233.

163. Zhao, Y., et al., *High performance silicon-based GeSn p–i–n photodetectors for short-wave infrared application.* Chinese Physics B, 2019. **28**(12).

164. Werner, J., et al., *Germanium-tin p-i-n photodetectors integrated on silicon grown by molecular beam epitaxy.* Applied Physics Letters, 2011. **98**(6).

165. Xu, S., et al., *GeSn lateral p-i-n photodetector on insulating substrate.* Opt Express, 2018. **26**(13): p. 17312-17321.

166. Bertrand, M., et al., *Mid-Infrared GeSn-Based LEDs with Sn Content up to 16%*, in *2019 IEEE 16th International Conference on Group IV Photonics (GFP)*. 2019. p. 1-2.

167. Senaratne, C.L., et al., *Advances in Light Emission from Group-IV Alloys via Lattice Engineering and n-Type Doping Based on Custom-Designed Chemistries.* Chemistry of Materials, 2014. **26**(20): p. 6033-6041.

168. Gupta, J.P., et al., *Infrared electroluminescence from GeSn heterojunction diodes grown by molecular beam epitaxy.* Applied Physics Letters, 2013. **102**(25).

169. Du, W., et al., *Room-temperature electroluminescence from Ge/Ge1-xSnx/Ge diodes on Si substrates.* Applied Physics Letters, 2014. **104**(24).

170. Wirths, S., et al., *Lasing in direct-bandgap GeSn alloy grown on Si.* Nature Photonics, 2015. **9**(2): p. 88-92.

171. Al-Kabi, S., et al., *An optically pumped 2.5 µm GeSn laser on Si operating at 110 K.* Applied Physics Letters, 2016. **109**(17).

172. Vincent, B., et al., *Characterization of GeSn materials for future Ge pMOSFETs source/drain stressors.* Microelectronic Engineering, 2011. **88**(4): p. 342-346.

173. Wang, H., et al., *Performance Enhancement in Uniaxially Strained Germanium–Tin FinTFET: Fin Direction Dependence.* IEEE Transactions on Electron Devices, 2017. **64**(7): p. 2804-2811.

174. Soref, R., J. Hendrickson, and J.W. Cleary, *Mid- to long-wavelength infrared plasmonic-photonics using heavily doped n-Ge/Ge and n-GeSn/GeSn heterostructures.* Opt Express, 2012. **20**(4): p. 3814-24.

175. Augel, L., et al., *Ellipsometric characterization of doped Ge_{0.95}Sn_{0.05} films in the infrared range for plasmonic applications.* Opt Lett, 2016. **41**(18): p. 4398-400.

176. Prucnal, S., et al., *Ex situ n+ doping of GeSn alloys via non-equilibrium processing.* Semiconductor Science and Technology, 2018. **33**(6).

177. Nastasi, M. and J.W. Mayer, *Ion Implantation and Synthesis of Materials*. 2006.

178. Liu, J.-Y., et al., *High Dopant Activation of Phosphorus in Strained and Relaxed GeSn by Rapid Thermal Annealing and Microwave Annealing*, in *2019 Electron Devices Technology and Manufacturing Conference (EDTM)*. 2019. p. 44-46.

179. Ahmed, W. and E. Ahmed, *Ion implantation and in situ doping of silicon.* Materials Chemistry and Physics, 1994. **37**(3): p. 289-294.

180. Xu, C., et al., *Fabrication of Ge:Ga Hyperdoped Materials and Devices Using CMOS-Compatible Ga and Ge Hydride Chemistries.* ACS Appl Mater Interfaces, 2018. **10**(43): p. 37198-37206.

181. Vohra, A., et al., *Low temperature epitaxial growth of Ge:B and Ge0.99Sn0.01:B source/drain for Ge pMOS devices: in-situ and conformal B-doping, selectivity towards oxide and nitride with no need for any post-epi activation treatment.* Japanese Journal of Applied Physics, 2019. **58**(SB).

182. Bogumilowicz, Y. and J.M. Hartmann, *Reduced-pressure chemical vapor deposition of boron-doped Si and Ge layers.* Thin Solid Films, 2014. **557**: p. 4-9.

183. Uppal, S., et al., *Diffusion of ion-implanted boron in germanium.* Journal of Applied Physics, 2001. **90**(8): p. 4293-4295.

184. Sgourou, E.N., et al., *Diffusion and Dopant Activation in Germanium: Insights from Recent Experimental and Theoretical Results.* Applied Sciences, 2019. **9**(12).

185. Stringfellow, G., *Organometallic Vapor-Phase Epitaxy*

2nd Edition. 1999: Academic Press. 572.

186. Bhargava, N., J. Margetis, and J. Tolle, *As doping of Si–Ge–Sn epitaxial semiconductor materials on a commercial CVD reactor.* Semiconductor Science and Technology, 2017. **32**(9).

187. Milazzo, R., et al., *N-type doping of Ge by As implantation and excimer laser annealing.* Journal of Applied Physics, 2014. **115**(5).

188. Margetis, J., et al. *Growth and Characterization of Epitaxial Ge1-XSnx Alloys and Heterostructures Using a Commercial CVD System*

in *ECS Meeting Abstracts*. 2014.

189. Vincent, B., et al., *Undoped and in-situ B doped GeSn epitaxial growth on Ge by atmospheric pressure-chemical vapor deposition.* Applied Physics Letters, 2011. **99**(15).

190. Tsai, C.-E., et al., *Boron-doping induced Sn loss in GeSn alloys grown by chemical vapor deposition.* Thin Solid Films, 2018. **660**: p. 263-266.

191. Martens, K., et al., *On the Correct Extraction of Interface Trap Density of MOS Devices With High-Mobility Semiconductor Substrates.* IEEE Transactions on Electron Devices, 2008. **55**(2): p. 547-556.

192. Kohen, D., et al., *Enhanced B doping in CVD-grown GeSn:B using B δ-doping layers.* Journal of Crystal Growth, 2018. **483**: p. 285-290.

193. Jang, S.-M., *Chemical Vapor Deposition of Epitaxial Silicon-Germanium from Silane and Germane.* Journal of The Electrochemical Society, 1995. **142**(10).

194. Khanam, A., et al., *A demonstration of donor passivation through direct formation of V-Asi complexes in As-doped Ge1−xSnx.* Journal of Applied Physics, 2020. **127**(19): p. 195703.

195. Margetis, J., et al., *Chemistry and kinetics governing hydride/chloride chemical vapor deposition of epitaxial Ge1−xSnx.* Journal of Vacuum Science & Technology A, 2019. **37**(2).

196. Srinivasan, V.S.S., et al., *Contact resistivities of antimony-doped n-type Ge1−xSnx.* Semiconductor Science and Technology, 2016. **31**(8): p. 08LT01.

197. *Sb Doped GeSn Growth by MOCVD with Newly Employed Source Gases.* ECS Meeting Abstracts, 2016.

198. Jung, W.-S., et al., *Fluorine passivation of vacancy defects in bulk germanium for Ge metal-oxide-semiconductor field-effect transistor application.* Applied Physics Letters, 2012. **101**(7).

199. Liu, F., et al., *Suppressing the cellular breakdown in silicon supersaturated with titanium.* Journal of Physics D: Applied Physics, 2016. **49**(24): p. 245104.

200. Prucnal, S., et al., *Band gap renormalization in n-type GeSn alloys made by ion implantation and flash lamp annealing.* Journal of Applied Physics, 2019. **125**(20): p. 203105.